UNIVERSITY OF SOUTHAMPTON

Faculty of Engineering and Physical Sciences
School of Physics and Astronomy

Tailored Reservoir of Exciton-Polariton Condensates

by

Yuan Wang

ORCiD: 0000-0002-0688-3276

A thesis for the degree of
Doctor of Philosophy

July 2023

University of Southampton

Abstract

Faculty of Engineering and Physical Sciences
School of Physics and Astronomy

Doctor of Philosophy

Tailored Reservoir of Exciton-Polariton Condensates

by Yuan Wang

The AlGaAs-like quantum wells sandwiched by high-quality microcavities can produce Wannier–Mott excitons and long-lifetime microcavity photons, forming the lightweight exciton-polaritons (polaritons) in the strong coupling regime. Polariton condensates can occur at cryogenic temperatures through optically excited high-energy excitons. Then the excitons follow a quick optical-phonon-induced relaxation into the reservoir, high-momentum of the lower polariton branch (LP). Through multiple scattering with acoustic phonons and parametric scattering in the vicinity of the LP bottleneck, the photonic components of the polaritons are increasing, and the polaritons on the reservoir eventually fall into the bottom or higher position of the LP, leading to the polariton condensates. The strong polariton-polariton interaction due to the excitonic components of the polaritons makes the polariton condensates a promising testbench for various nonlinear effects in the realm of quantum fluid of light.

Through numerically solving the generalized Gross-Pitaevskii model coupled with the reservoir rate equation, this thesis studies methods to enhance and focus ballistic polariton condensates with tailored reservoir driven by localized nonresonant asymmetric-shaped excitation. This thesis demonstrates that the lens-shaped pump above the threshold can drive the focus of condensate away from the pumping region; by employing a second excitation next to the lens, the planar condensate flow is generated and can reflect and scatter with the lens-shaped blueshift, resulting in the focused condensate beating with hundreds of gigahertz. Furthermore, the source-lens system can be reprogrammed to achieve different beating locations and frequencies, paving the way for the realization of the all-optical transistor. This thesis also shows that in the polariton lattices, the stronger interaction between the nearest neighbors is achieved in the polygonal- rather than Gaussian-shaped pump due to the focused condensates flowing towards the nearest neighbors; and, in comparison to a Gaussian-shaped pump, the polygonal-shaped pump can increase the spatial coherence for a given power density or lower the energy needed for condensation. This finding can greatly improve spatial coherence in the needs of large-scale polariton condensates networks.

Contents

Declaration of Authorship

I, Yuan Wang, declare that this thesis and the work presented in it is my own and has been generated by me as the result of my own original research.

I confirm that:

1. This work was done wholly or mainly while in candidature for a research degree at this University;
2. Where any part of this thesis has previously been submitted for a degree or any other qualification at this University or any other institution, this has been clearly stated;
3. Where I have consulted the published work of others, this is always clearly attributed;
4. Where I have quoted from the work of others, the source is always given. With the exception of such quotations, this thesis is entirely my own work;
5. I have acknowledged all main sources of help;
6. Where the thesis is based on work done by myself jointly with others, I have made clear exactly what was done by others and what I have contributed myself;
7. Parts of this work have been published as:
   Y. Wang, et al., Phys. Rev. B **104**, 235306, (2021),
   Y. Wang, et al., Phys. Rev. B **106**, 245304, (2022).

Signed:..... Date:.....

Acknowledgements

I am deeply grateful to Prof. Pavlos Lagoudakis and Prof. Simone De Liberato for their unwavering kindness, support, and guidance throughout the whole of my PhD courses. Their ambition and vision in both physics and life have profoundly shaped not only my research abilities but also my attitude towards future challenges.

I also wish to express my deepest gratitude to Dr. Helgi Sigurðsson, a passionate physicist, who served as my unofficial co-supervisor. His advice on leveraging the power of the graphics processing unit in numerical studies has been tremendously beneficial.

I would like to thank Prof. Hendrik Ulbricht for the guidance in organizing the QLM Summer School 2019, Nicky Brooks and Jacob Viner for their assistance, and the speakers and QLM communities for all kinds of help and suggestions. I would also like to thank Prof. Vasileios Apostolopoulos and Prof. David Smith for their help, suggestions, and encouragement throughout my studies.

Special thanks go to my examiners, Prof. Alexey Kavokin and Prof. Nikolay Gippius. Their thorough evaluation and insightful comments greatly improved the quality of my work, and I am indebted to them for their time and expertise.

I am grateful to Dr. Krzysztof Sawicki for engaging in enlightening discussions and addressing my inquiries related to experimental details relevant to my studies throughout the thesis preparation process. I am also grateful to Dr. Julian Töpfer for his kindness and insightful discussion of our project. My gratitude extends to colleagues Dr. Christopher R Gubbin, Dr. Dmitriy Dovzhenko, Denis Aristov, and Stella Harrison for their inspirational conversations and maintaining a supportive work environment. Further thanks go to Dr. Mael Brossard and Dr. Ekaterina Grayfer for their assistance with paper submissions. My friends Dewei Chen, Yuguang Chen, Viviana Merlino, Yipeng Shen, Wei Xiao, Zihao Guan, Yeling Zhou, and Zixin Zhang also deserve my gratitude for their care and support throughout my PhD journey.

I want to give special thanks to my friend Dr. Erika Cortese and Bruno Liistro for pulling me out of my puzzle from time to time and inviting me to embrace the meaning of life from a different perspective.

I also want to thank everyone who helped me directly or indirectly but not listed above.

And last but not least, I want to thank my parents, Junling Li and Weidong Wang. Without their greatest support and encouragement throughout my studies and life, this thesis would never be possible.

Publications

Publications treated in this thesis:

Y. Wang, H. Sigurdsson, J. D. Töpfer, and P. G. Lagoudakis, *Reservoir optics with exciton-polariton condensates*, Physical Review B **104**, 235306 (2021)

Y. Wang, P. G. Lagoudakis, and H. Sigurdsson, *Enhanced coupling between ballistic exciton-polariton condensates through tailored pumping*, Physical Review B **106**, 245304 (2022)

Other publication:

Y. Wang and S. De Liberato, *Theoretical proposals to measure resonator-induced modifications of the electronic ground state in doped quantum wells*, Physical Review A **104**, 023109 (2021)

K. Sawicki, D. Dovzhenko, Y. Wang, H. Sigurðsson and P. G. Lagoudakis, *Power-driven Zeeman suppression and inversion in exciton-polariton condensates*, Manuscript in Preparation (2023)

Chapter 1

Introduction

Cavity quantum electrodynamics explains the interaction between the microcavity photons and the collective excitation confined in semiconductor quantum wells (QWs). Consider a two-level system where an electron is present inside a cavity that has both ground and excited states. Through spontaneous emission, the electron in the excited state can drop to the ground state, emitting photons with energy equal to the electronic transition energy. The remaining photons inside the cavity can either be reabsorbed by the electron or decay away from the cavity. A high-quality cavity can diminish photon losses and enhance the interaction between the photons and the excitation because of long-lifetime photons. A clear statement was found in 1946 by Purcell that through tailoring the density of states of the photons, in other words, by engineering the cavity itself, the spontaneous emission rate of the system can be enhanced or suppressed [1]. That is to say, the cavity plays a vital role in light-matter interaction.

When the decay rate of any system's component (e.g., the cavity photons and excitation) exceeds light-matter coupling strength, the weak-coupling regime is dominant in the system's dynamics. In this regime, these emitted photons are damped away and cannot stimulate electronic excitation again. Suppose the electrons are initially at the ground state, and we measure the probability of finding electrons in an excited state against time after the external stimulation on the electrons; the probability decays faster when the density of states of photons is in resonance with the excitation frequency, or it decays slower when they are off the resonance. These phenomena have been demonstrated in experiments of quantum dot systems [2]. Now, it raises the question: what if the quality of the cavity is good enough that the photons can exist long enough to be reabsorbed by the electrons? To answer this question, the system needs to enter the strong-coupling (SC) regime, where the decay rate is lower than that of any system's component. Assuming that the aforementioned measurements are taken again under the SC regime, damped oscillation is expected in the probability curvature against time. Such an oscillation is also called Rabi oscillation, which was first observed in the experiment using Rydberg atoms [3].

In the presence of external stimulation, the cavity photons, together with the QW excitation, would participate in processing stimulation, emission, and reabsorption, under the SC regime. Due to the fast energy exchange between the photons and the excitation, the polaritons stemming from being part light and part matter are formed. There are various types of polaritons in nature, such as exciton-polaritons, intersubband-polaritons, surface-plasmon-polaritons, and many other couplings between quasiparticles and light (more than 70 types of polaritons are known and are listed in [4]). The number of components of the polaritons is not limited to two. A more complicated mixture or interaction with more than two different matter modes with various forms is possible and exists in nature. For example, one would expect intersubband-polaron polaritons because of the interaction among intersubband transitions, longitudinal-optical phonons, and photons. In this thesis, we restrict ourselves to exciton-polaritons in the SC regime.

Exciton-polaritons (from here on polaritons), in which the SC regime was observed in experiment until 1992 [5] and originating from SC between microcavity photons and confined QW excitons, are bosonic quasiparticles. Owing to the photonic component of the polariton, a small effective mass (around 10^{-5} of the electron mass) can be achieved. The critical temperature of Bose-Einstein condensates (BEC) for an ideal three-dimensional noninteracting Bose gas is inversely proportional to the bosonic effective mass for a given bosonic gas density. Hence, due to the small effective mass, polaritons can attain higher temperatures (around 10 K for inorganic material) for BEC than the atomic gas has (around 170 nK for rubidium-87 atoms [6] and 2 μK for sodium atoms [7]). The polariton condensates can be produced using nonresonant excitation once the pumping power density exceeds the critical (threshold) one. Together with a strong exciton-exciton interaction strength from the excitonic component of the polaritons, the phase transitions from nonresonant external lasers into a macroscopically occupied coherent state are realized [8] even at room temperature [9–11].

In polariton condensates, the repulsive polariton-polariton interaction that contributes the most to the excitonic part of the polaritons can produce a blue-shifting potential [12, 13]. This theoretically predicts the possibility of engineering the potential landscape through shaping the nonresonant excitation. From the experiments' perspective, the development and application of the spatial light modulator make it practicable to artificially design the pumping configurations, bringing the extra flexibility to manipulate macroscopic quantum states directly [12, 14]. In the field of optics, irreversible fabrication methods like etching, deposition, and lithography are commonly used to design samples for specific tasks. In contrast, the potential produced from polariton condensates can be not only tailored by applying external excitation with different pump profiles but also be able to be reprogrammed through the spatial light modulator for different needs, leading to the realization of the all-optical devices. Several important experiments have been made in all-optical manipulation of polariton

condensates using nonresonant excitation methods [12, 14] over the past decade. For example, the nonresonantly pulsed polariton wavepackets that could be reamplified when crossing the excitation area due to stimulated scattering of reservoir excitons into the wavepacket were demonstrated in 1D lithographically etched microcavities [15], and the amplification without beam deflection was realized in experiment [16]. Other applications, such as polariton trapping [17, 18], exceptional points [19], dissipative annealing of the XY model [20], vortex manipulation [21, 22], and lattices [23, 24] have been studied.

Another fascinating feature of polariton condensates is the synchronization and spontaneous coherence. Dating back to the double-slit experiment by Thomas Young in 1802, the coherence extracted from one or multiple quantities also plays a dominant role in many aspects. In a polariton system, good coherence can give access to intricate long-range and long-time condensate dynamics and also play a role in various optical applications such as biological imaging [25], information processing [26, 27], neuromorphic computing [28], and metrology [29]. The application of polariton networks usually requires the maintenance of spatial coherence in a large area; however, the limited power from external excitation cannot always meet the demand for large-scale polariton lattices.

In this thesis, the aim is to utilize the aforementioned features of polariton condensates to develop all-optical devices capable of controlling and focusing the polariton flow and enhancing coherence between internodes of polariton lattices. The challenge lies in obtaining the analytical solution of the complex nonlinear phenomena resulting from the interaction between polaritons and reservoir excitons. However, conventional CPU-based methods become the bottleneck when it comes to large spatial grids and long temporal scales. To overcome this problem, parallel computational algorithms are applied to find the solution to the Gross-Pitaevskii equation (GPE) by leveraging the power of the graphics processing unit. For the sake of clarity, the rest of the thesis is organized as follows:

In chapter 2, backgrounds related to microcavity photons, QW excitons, and polariton condensates are introduced. First, the general properties regarding microcavity photons and QW exciton are given by explaining how the microcavity's geometry alters the effective mass of microcavity photons and how confinement along the growth direction of the QWs changes the dynamics of the excitons. Later, the behavior of the coupling between photons and excitons under the SC regime and the condition of the bosonic approximation of the exciton-polaritons are shown. In the last part, the physical model, GPE coupled with the reservoir rate equation, of polariton condensates in the general nonlinear and linear case is shown and discussed; besides, the mutual first-order spatial coherence in arbitrary two regions of a condensate map is introduced in the chapter 5.

In chapter 3, a self-built CUDA-based computational tool is introduced using the split-step Fourier method (SSFM) to numerically solve the GPE. Specifically, the theoretical expression and accuracy of SSFM are presented; besides, a brief introduction to CUDA, from both software's and hardware's perspective, which is key to the manipulation of the self-defined function, is given. Finally, some algorithms that integrate SSFM into the CUDA are listed. Since a strong nonequilibrium input-output system is mostly considered in this thesis, obtaining the exact theoretical expression for most cases is impossible and the numerical solution introduced in this chapter covers most of the numerical results.

In chapter 4, starting from a simplified case, the numerical studies of the Schrödinger equation with the resonant planar wave, the lens-shaped complex-valued potential, and the photonic losses are shown. Then taking all the nonlinear terms from the GPE into consideration, an all-optical lens-shaped device is numerically studied to guide, focus and enhance the outflowing polariton condensates away from the nonresonant optically-excited pump region. Moreover, the combination of a planar condensate flow produced by a second excitation and a lens-shaped one is investigated. Besides, several pump configurations to produce the focused condensate outflows, the possibilities to engineer the output of the condensate fluid from all-optical source-lens devices, and possible applications are also proposed.

In chapter 5, the comparison of density maps among a polygonal- and Gaussian-shaped pump profile is made first. The isometric from the duality of patterns perspective is studied, and the rotation of the concentration from the corner of the condensate in real and momentum space is observed. The different orientations among each polygonal spot (example of triangular spots) in a single hexagonal structure are shown. Eventually, the enhancement of the coupling between the nearest neighbors in a polariton condensate lattices is studied.

In chapter 6, overall conclusions are made.

Chapter 2

Introduction to exciton-polariton condensates

2.1 Introduction

As preparation for the subsequent sections and chapters, the terminology, physical phenomena, quantum theory of the polariton system and polariton condensates, or any technical details that need extra clarification are discussed in this chapter. The light-matter system covering the microcavity photons, excitons, and strong coupling between them is introduced first in section 2.2; In section 2.3, the condition, mechanism, and methods to producing the polariton condensates are introduced; Section 2.4 is the conclusions of this chapter.

2.2 Introduction to light-matter system

This section aims to briefly and explicitly introduce each component of the polariton system. Also, the approximation used to derive the theoretical description is mentioned. In section 2.2.1, how the microcavity photons are created and how the physical property can be altered through the microcavity system are explained. For simplicity, the metallic cavity, as a kind of the Fabry–Pérot cavity, is taken for the demonstration; besides, the cavity, made of distributed Bragg reflectors (DBRs) and widely used in polaritons, is also mentioned. In section 2.2.2, the formation of excitons is theoretically studied in an artificial lattice system embedded with a periodic infinity potential, and the numerical analysis of the energy band of excitons in bulk lattices is obtained through the Bloch theorem; moreover, the behavior of excitons with confinement from the QW, the spin selection rule, and the bosonic limit of excitons are also explored. In section. 2.2.3, the polariton operator is derived following the Hopfield diagonalization,

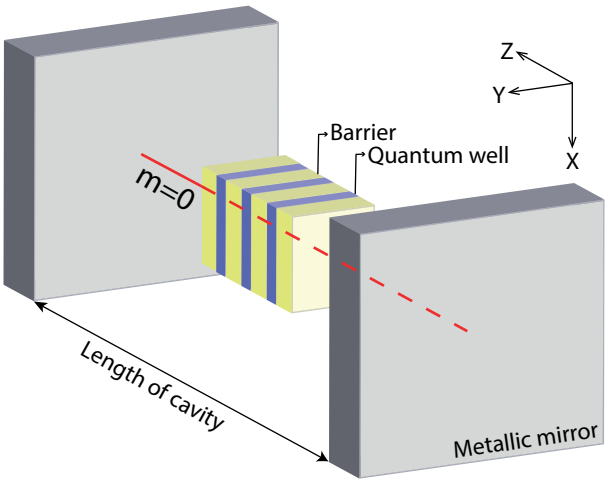

FIGURE 2.1: Sketch of the planar metallic cavity and stacks of quantum wells. As an example, the transverse magnetic mode ($TM_m, m \in \mathbb{N}_0$) that the direction of the electric field is perpendicular to the mirror ($m = 0$) and is highlighted in the red line.

and the spectrum of the polaritonic system with positive, zero, and negative detuning is investigated.

2.2.1 Microcavity photons

The planar metallic cavity is widely used to generate cavity photons in cavity quantum electrodynamics. For example, the Fabry–Pérot cavity consisting of two planer metallic mirrors with high reflectivity and multiple QWs is sketched in Fig. 2.1. Let us assume that the two large enough parallel mirrors are in the x-y plane and the growth of the semiconductor heterostructures is along the z -axis, then the z -axis becomes the key parameter altering the density of the photons coupled to the particles inside the QWs. For simplicity, only the transverse magnetic photonic modes are considered, and the photonic frequency as a function of mode and the length of the cavity is given by

$$\frac{\varepsilon_C}{c^2}\omega^2_{n,\boldsymbol{k}_\parallel} = \boldsymbol{k}^2_\parallel + \frac{\pi^2 n_C^2}{L_C^2}, \tag{2.1}$$

where $\boldsymbol{k}_\parallel = (k_x, k_y)$ is the in-plane wavevector, c the speed of light, n_C the photonic mode with $n_C \in [0, 1, 2, ...]$, and ε_C is the dielectric constant of the cavity material.

Ideally, the total number of frequencies can reach infinity without applying any boundary conditions; however, in reality, each cavity has a maximum frequency called the cutoff frequency. When the frequency of the cavity exceeds this frequency, the cavity becomes transparent. According to the description of the cut-off frequency, we obtain

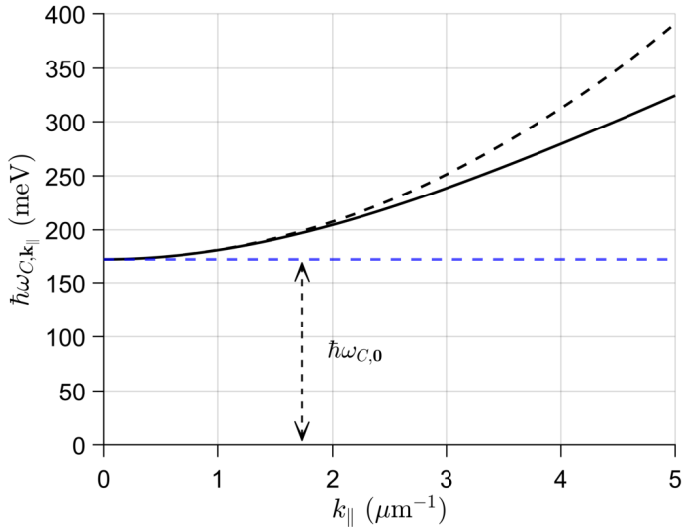

FIGURE 2.2: Dispersion relation of microcavity photons as a function of the in-plane wavevector. The black dashed line refers to the parabolic approximation of photonic frequency. The blue dashed line refers to the cutoff energy in parabolic approximation. Parameters: $\varepsilon_C = 12.9$, $L_C = 2.0\,\mu m$, and $n_C = 2$.

the relation

$$\sum_{n,\boldsymbol{k}_\parallel} |\omega_{n,\boldsymbol{k}_\parallel}| \leqslant \omega_M, \tag{2.2}$$

where ω_M denotes the upper cut-off frequency of the metallic cavity. Furthermore, the frequency of the cavity as the function of the $\boldsymbol{k}_\parallel$ with a parabola-like form can be derived from Eq. (2.1) under Taylor expansion with relation $|\boldsymbol{k}_\parallel| \ll k_z$

$$\omega_{C,\boldsymbol{k}_\parallel} \approx \omega_{C,\mathbf{0}} + \frac{\hbar}{2m_C}\boldsymbol{k}_\parallel^2, \tag{2.3}$$

with

$$\omega_{C,\mathbf{0}} = \frac{c}{\sqrt{\varepsilon_C}}k_z, \qquad m_C = \hbar\omega_{C,\mathbf{0}}\frac{\varepsilon_C}{c^2}, \qquad k_z = \frac{\pi n_C}{L_C} \tag{2.4}$$

where $\omega_{C,\mathbf{0}}$ is the minimum frequency taken at $\boldsymbol{k}_\parallel = \mathbf{0}$, m_C the effective mass of the cavity, and k_z is the out-of-plane wavevector. Figure 2.2 shows the comparison between the dispersion relation with [see Eq. (2.3)] and without [see Eq. (2.1)] parabolic approximation. We can see that the parabolic model is accurate when the in-plane wavevector is in the vicinity of zero. It is worth mentioning that Eq. (2.1) also reveals the nature of the dispersion relation of the part-light part-matter quasiparticles. The photonic components of the quasiparticles have inherently obtained the nature of microcavity photons resulting in a similar dispersion relation of the quasiparticles, though the matter part in QW also contributes to the coupled system.

When exciton-polaritons are concerned, the microcavity mirrors used to reflect the photons are called distributed Bragg reflectors (DBRs). DBRs consist of multiple pairs of dual layers; each pair is made of alternating materials with low and high refractive indices. Unlike the semiconductor structure shown in Fig. 2.1 that the length of the microcavity can be smoothly tuned, and the length of DBRs usually cannot be altered once a stack of DBRs sandwiching the QWs are fabricated. Such DBRs and QWs sandwiched in between are illustrated in Fig. 2.3. The essence of using alternating materials

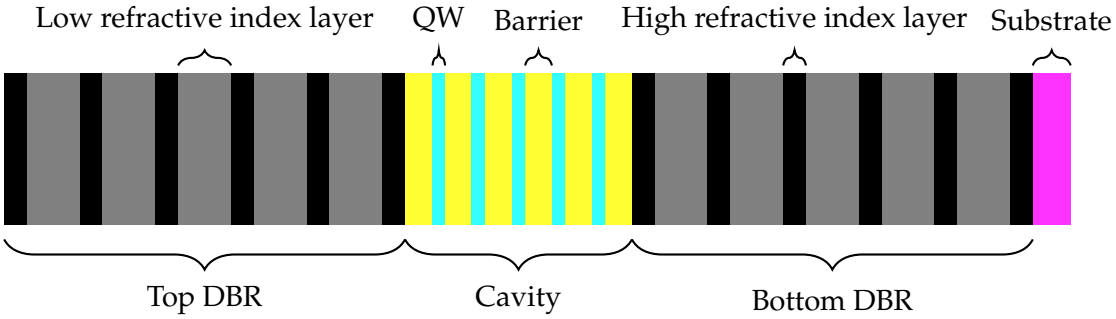

FIGURE 2.3: Sketch of the DBR microcavity and quantum wells. Each DBR consists of 5 pairs of low (gray area) and high (black area) refractive index materials. 5 quantum wells (blue area) and the attached barriers (yellow area) are shown as an example. The magenta layer is the substrate at the end of the bottom. (Figure is adapted from Ref. [30])

is to produce a stopband in the cavity region shown in Fig. 2.3. When the cavity wavelength is in the vicinity of four times the optical thickness of each layer of DBR, the DBRs behave with high reflectivity. In this case, constructive interference occurs from the refractive wave resulting in a planar microcavity between two DBRs. In the cavity region (see Fig. 2.3), the cavity wavelength matches twice the total optical thickness of the QWs and barrier layers. It should be noted that the QW length in Fig. 2.3 seems comparable to the length of the barrier or cavity, but it is not true in the real DBR microcavity. The length of the QW (around 6 nm) is much thinner compared to the length of the cavity region (around 1700 nm) [31]. In this thesis, we do not get involved with the property of the DBRs, and although the mechanics of producing the cavity mode is different from that of the Fabry-Pérot cavity to that of the DBR planar cavity, what affects the characteristic of microcavity photons most is still the losses of the microcavity. As shown in Fig. 2.4, the microcavity is designed with a cavity resonance at 850 nm, and the reflectivity is close to unity when the wavelength is around 850 nm $\pm$ 50 nm.

2.2.2 Excitons and quasiparticles

Electrons below the Fermi level of the valence band (VB) are naturally fermions. However, through stimulation that has higher energy than the energy gap between the VB and the conduction band (CB) of light, the electrons can transfer to the CB while leaving holes with positive charges from the VB, resulting in boson-like quasiparticles.

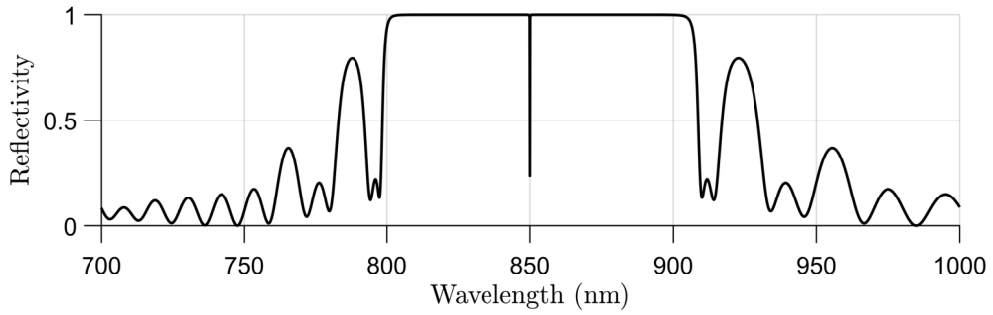

FIGURE 2.4: Reflectivity of the DBR microcavity versus wavelength. Top (Bottom) DBR consists of 23 (26) pairs of GaAs and AlAs with GaAs cavity.

Such quasiparticles are called excitons, consisting of electron-hole pairs, because of the Coulomb interaction. In nature, there are two main types of excitons: Frenkel excitons and Wannier–Mott excitons. The former, commonly found in organic crystals, tends to have a stronger electron-hole Coulomb interaction forming a delocalized exciton state, while the latter, usually observed in inorganic materials, has a weaker Coulomb interaction due to a high screening effect with a localized state. In this thesis, only Wannier–Mott excitons are considered.

An exciton formation invokes a many-body problem that involves the attractive interaction from the electron-hole pairs and the repulsive interaction between the electrons in CB and the residual electrons in VB, and it turns out that the competition diminishes the attractive coupling between electrons and holes. However, assuming that the number of electrons in CB is much smaller than the number of residual electrons in VB, this complex system can be further converted to a hydrogen-like problem if we consider the residual electrons and holes in VB as a proton with a positive charge.

2.2.2.1 Energy band of zinc-blende crystal bulk lattice

To understand the band structure of the semiconductor material, $\boldsymbol{k}\cdot\boldsymbol{p}$ perturbation theory is a useful tool to simplify the numerical model. To emulate the real crystal structure in a bulk semiconductor system, we propose an infinity periodic potential $V_C(\boldsymbol{r})$ satisfying $V_C(\boldsymbol{r}) = V_C(\boldsymbol{r}+\boldsymbol{R})$. Thus, neglecting the external electromagnetic field, the wavefunction $\Psi(\boldsymbol{r})$ corresponding to the time-independent Hamiltonian of an electron inside potential $V_C(\boldsymbol{r})$ considering the spin-orbit interaction (SOI) is

$$\left\{\frac{\widehat{p}^2}{2m_0} + V_C(\boldsymbol{r}) + \frac{\hbar}{4m_0^2c^2}\widehat{p}\cdot\boldsymbol{\sigma}\times[\nabla_{\boldsymbol{r}}V_C(\boldsymbol{r})]\right\}\Psi(\boldsymbol{r}) = E\Psi(\boldsymbol{r}), \tag{2.5}$$

where $\boldsymbol{r} = (x, y, z)$ is the position of exciton, c is the speed of light, m_0 the free electron mass, $\boldsymbol{\sigma} = (\sigma_x, \sigma_y, \sigma_z)$ the Pauli matrices and $\widehat{p} = -i\hbar\nabla_{\boldsymbol{r}}$ is the momentum operator.

The general solution of Eq. (2.5) is given by Bloch theorem[1]

$$\psi_{n,\boldsymbol{k}}(\boldsymbol{r}) = u_{n,\boldsymbol{k}}(\boldsymbol{r})e^{i\boldsymbol{k}\cdot\boldsymbol{r}}, \tag{2.6}$$

where n is the band index, $\boldsymbol{k} = (k_x, k_y, k_z)$ the wavevector, and $u_{n,\boldsymbol{k}}(\boldsymbol{r})$, a periodic function which has the same periodicity as the $V_C(\boldsymbol{r})$, is the Bloch amplitude. Substituting the Eq. (2.6) into the Eq. (2.5), we arrive at

$$\left\{ \underbrace{\frac{\widehat{p}^2}{2m_0} + V_C(\boldsymbol{r})}_{\widehat{H}_0} + \underbrace{\overbrace{\frac{\hbar}{4m_0^2c^2}\widehat{p}\cdot\boldsymbol{\sigma}\times[\nabla V_C(\boldsymbol{r})]}^{\Delta\widehat{H}_0} + \overbrace{\frac{\hbar}{m_0}\boldsymbol{k}\cdot\widehat{\mathcal{P}}}^{\Delta\widehat{H}_k}}_{\Delta\widehat{H}} \right\} u_{n,\boldsymbol{k}} = \left(\underbrace{E_{n,\boldsymbol{k}} - \frac{\hbar^2\boldsymbol{k}^2}{2m_0}}_{\mathcal{E}_{n,\boldsymbol{k}}} \right) u_{n,\boldsymbol{k}}, \tag{2.7}$$

in which $\mathcal{E}_{n,\boldsymbol{k}}$ is considered to be the eigenvalue of the system, $\widehat{H}_0$ and $\Delta\widehat{H}$ are denoted as a non-perturbed and perturbed system, respectively, and the operator $\widehat{\mathcal{P}}$ including the SOI is

$$\widehat{\mathcal{P}} = \widehat{p} + \frac{\hbar}{4m_0c^2}\boldsymbol{\sigma}\times[\nabla V_C(\boldsymbol{r})]\,. \tag{2.8}$$

Note that the perturbed term in Eq. (2.7) can be further divided into $\boldsymbol{k}$ independent part denoted as $\Delta\widehat{H}_0$ and the dependent one $\Delta\widehat{H}_{\boldsymbol{k}}$. The former contributes to the SOI at the band edge with $\boldsymbol{k} = \boldsymbol{0}$, which eventually leads to the spin-off band (see Fig. 2.5). Taking the perturbation theory around $\boldsymbol{k} \approx \boldsymbol{0}$, the eigenenergy of Eq. (2.7) up to second order is obtained

$$\underbrace{E_{n,\boldsymbol{k}} - \frac{\hbar^2\boldsymbol{k}^2}{2m_0}}_{\mathcal{E}_{n,\boldsymbol{k}}} \approx \underbrace{E_{n,\boldsymbol{0}}}_{\mathcal{E}_{n,\boldsymbol{0}}} + \langle u_{n,\boldsymbol{0}}|\Delta\widehat{H}|u_{n,\boldsymbol{0}}\rangle + \sum_{m\neq n}\frac{\langle u_{n,\boldsymbol{0}}|\Delta\widehat{H}|u_{m,\boldsymbol{0}}\rangle\langle u_{m,\boldsymbol{0}}|\Delta\widehat{H}|u_{n,\boldsymbol{0}}\rangle}{\langle u_{n,\boldsymbol{0}}|\widehat{H}_0|u_{n,\boldsymbol{0}}\rangle - \langle u_{m,\boldsymbol{0}}|\widehat{H}_0|u_{m,\boldsymbol{0}}\rangle}, \tag{2.9}$$

where the second term on the right-hand side (RHS) of Eq. (2.9) is canceled because $u_{n,\boldsymbol{0}}(\boldsymbol{r})$ and $\widehat{p}$ are an even and odd functions, respectively. Rearranging the Eq. (2.9), we have

$$E_{n,\boldsymbol{k}} \approx E_{n,\boldsymbol{0}} + \frac{\hbar^2\boldsymbol{k}^2}{2m_0} + \frac{\hbar}{m_0}\sum_{n\neq m}\frac{\boldsymbol{k}\cdot|\langle u_{n,\boldsymbol{0}}|\widehat{\mathcal{P}}|u_{m,\boldsymbol{0}}\rangle|^2}{E_{n,\boldsymbol{0}} - E_{m,\boldsymbol{0}}} + \sum_{n\neq m}\frac{|\langle u_{n,\boldsymbol{0}}|\Delta\widehat{H}_0|u_{m,\boldsymbol{0}}\rangle|^2}{E_{n,\boldsymbol{0}} - E_{m,\boldsymbol{0}}}. \tag{2.10}$$

The last term of RHS of (2.10) is nonnegligible at $\boldsymbol{k} = 0$ due to SOI. If we neglect the entire SOI, operator $\widehat{\mathcal{P}}$ in Eq. (2.10) is replaced with $\widehat{p}$, thus we arrive at

$$E_{n,\boldsymbol{k}} \approx E_{n,\boldsymbol{0}} + \frac{\hbar^2\boldsymbol{k}^2}{2m_0} + \frac{\hbar}{m_0}\sum_{n\neq m}\frac{\boldsymbol{k}\cdot|\langle u_{n,\boldsymbol{0}}|\widehat{p}|u_{m,\boldsymbol{0}}\rangle|^2}{E_{n,\boldsymbol{0}} - E_{m,\boldsymbol{0}}}. \tag{2.11}$$

[1]Bloch theorem can also be written as $\psi_{n,\boldsymbol{k}}(\boldsymbol{r}+\boldsymbol{R}) = \underbrace{u_{n,\boldsymbol{k}}(\boldsymbol{r}+\boldsymbol{R})}_{u_{n,\boldsymbol{k}}(\boldsymbol{r})}e^{i\boldsymbol{k}\cdot\boldsymbol{r}}e^{i\boldsymbol{k}\cdot\boldsymbol{R}} = \psi_{n,\boldsymbol{k}}(\boldsymbol{r})e^{i\boldsymbol{k}\cdot\boldsymbol{R}}$. This reveals that the probability of finding an electron in position $\boldsymbol{r}$ is the same as in $\boldsymbol{r}+\boldsymbol{R}$.

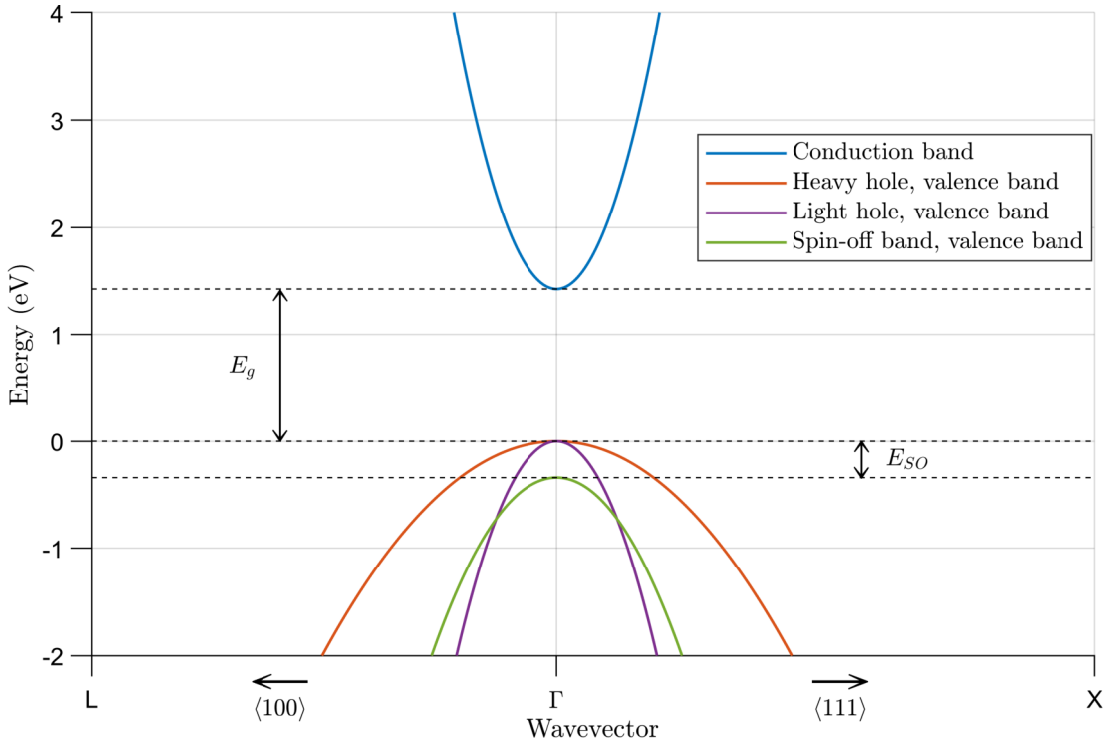

FIGURE 2.5: Calculated parabola-like band structure of GaAs around Γ point along direction ⟨100⟩ and ⟨111⟩. Parameters: Lattice constant of GaAs is 5.653 25 Å, E_g = 1.424 eV, E_{SO} = 0.34 eV, and mass of conduction band, heavy-hole band, light-hole band, and spin-off band, are, respectively, 0.067 m_0, 0.45 m_0, 0.082 m_0, and 0.154 m_0.

If we replace the m_0 with an effective mass m_n^* in the nth band, Eq. (2.11) can be written as

$$E_{n,\boldsymbol{k}} \approx E_{n,\boldsymbol{0}} + \frac{\hbar^2 \boldsymbol{k}^2}{2m_n^*} \tag{2.12}$$

with effective mass satisfying relation

$$\frac{1}{m_n^*} = \frac{1}{m_0} + \frac{2}{m_0^2} \sum_{n \neq m} \frac{|\langle u_{n,\boldsymbol{0}} | \hat{p} | u_{m,\boldsymbol{0}} \rangle|^2}{E_{n,\boldsymbol{0}} - E_{m,\boldsymbol{0}}}. \tag{2.13}$$

Thus, Eqs. (2.12) and (2.13) indicate that the energy band can also follow parabolic approximation with certain effective mass. And such effective mass is often considered a good approximation when $|\boldsymbol{k}|$ is in the vicinity of zero.

The band structure of GaAs, which is a type of zinc-blende crystal structure, is calculated using Eq. (2.12) with different effective mass and shown in Fig. 2.5. The CB shows an upward parabolic shape, while the VBs consisting of the heavy hole, light hole, and spin-off band show a downward shape. The effective mass of the VB is negative to keep the consistency with Eq. (2.12). It is noteworthy that the real band structure is much more complicated than that shown in Fig. 2.5, and for the sake of simplicity, we have

assumed that the band structure is isotropic along all directions and can be simplified into a parabolic form. That is to say, in this thesis, the effective mass is considered as a scalar quantity, although in real-world scenarios, the effective mass is more accurately represented as a tensor. The energy gap between the minimal value of the CB and the maximal value of the VB is denoted as E_g and the energy of splitting inside the VB due to SOI is E_{SO} as shown in Fig. 2.5. Although limited by the model, for bulk GaAs lattice, the degeneracy of the heavy hole and the light hole from the band edge, as well as the deviated spin-off band, is clearly shown in Fig. 2.5. However, for large wavevector, the accuracy of the parabolic approximation is lost.

2.2.2.2 Confinement from quantum well

For the bulk lattice, the degeneracy that appears in VB from the band edge shown in Fig. 2.5 is only valid for bulk material. If the material is structured in a QW with confinement from the growth axis of the semiconductor structure (see the horizontal axis of Fig. 2.3), the potential of the crystal $V_C(\boldsymbol{r})$ appearing in Section 2.2.2.1 should also include the confining energy along the growth axis. In other words, the exciton wavefunction can no longer be considered in 3D, but rather in quasi-2D. The degeneracy of VB shown in the bulk material is thus lifted due to the extra confinement on the growth axis, since the confining energy can result in an extra $\boldsymbol{k}$-independent splitting term in Eq. (2.12) giving rise to different energy from the band edge of two bands. The QW system here, ideally speaking a 2D system, can be understood like this: There is a quantum well with finite potential perpendicular to the xy-plane producing the bound energy along the z-axis; since the heavy hole with a smaller effective mass (negative effective mass in VB) has smaller bound energy than the light hole has, the degeneracy of the heavy hole and the light hole at the Γ point shown in Fig. 2.5 is lifted leaving a higher energy band from the heavy hole.

In Eq. (2.5), we have shown the Hamiltonian of an electron inside the perfect 3D periodic potential; however, instead of using bulk materials, as we have mentioned before, the extra confining potential along the z-axis should also be taken into account in the Hamiltonian. If we neglect the SOI and assume the density of the electron-hole pairs is low, the wavefunction of the exciton $\Psi_X(\boldsymbol{r})$ and its corresponding eigenvalue E_X of exciton confined by extra quantum well for electron $V_e(z_e)$ and hole $V_h(z_h)$ can be obtained from

$$\left[\frac{\widehat{p}_e^2}{2m_e^*} + \frac{\widehat{p}_h^2}{2m_h^*} - \frac{e^2}{4\pi\varepsilon_r\varepsilon_0|\boldsymbol{r}_e - \boldsymbol{r}_h|} + V_e(z_e) + V_h(z_h)\right]\Psi_X = E_X\Psi_X, \tag{2.14}$$

where m_e^* and m_h^* is the effective mass of electron and hole, respectively, ε_r is the dielectric constant of the material of the QW, $\boldsymbol{r}_e$ ($\boldsymbol{r}_h$) the position conjugate to the electron (hole), the first two terms and the third term on the left-hand side (LHS) of Eq. (2.14)

are, respectively, the momentum energy of the electron and hole, and the Coulomb interaction between them. It is worth mentioning that the exact exciton wavefunction from Eq. (2.14) is still in 3D, and we will consider a more ideal 2D case later under certain circumstances where the width of the QW is comparable to the Bohr radius of the exciton. For the electron-hole system, as a two-body system, Eq. (2.14) can be separated into the center-of-mass (CM) part and relative motion (RM) part

$$\left[\frac{\widehat{p}_{CM}^2}{2m_{CM}^*}+\frac{\widehat{p}_{RM}^2}{2m_{RM}^*}-\frac{e^2}{4\pi\varepsilon_r\varepsilon_0|\boldsymbol{r}_{RM}|}+V_e(z_e)+V_h(z_h)\right]\Psi_X=E_X\Psi_X, \tag{2.15}$$

where $\boldsymbol{r}_{RM}=\boldsymbol{r}_e-\boldsymbol{r}_h$ is the relative position between the electron and hole, $m_{CM}^*=m_e^*+m_h^*$ the center of mass of the exciton, $m_{RM}^*=m_e^*m_h^*/m_{CM}^*$ the reduced mass, $\widehat{p}_{CM}=-i\hbar\nabla_{CM}$ and $\widehat{p}_{RM}=-i\hbar\nabla_{RM}$ are the corresponding momentum operators in center-of-mass and relative coordinate, respectively. We define the wavefunction

$$\Psi_{X,n,\boldsymbol{k}_{CM}}=\underbrace{\frac{1}{\sqrt{V}}e^{i\boldsymbol{k}_{CM}\cdot\boldsymbol{r}_{CM}}}_{\text{free particle}}\psi_{n,\boldsymbol{k}_{CM}}^{RM}(\boldsymbol{r}_{RM})\phi_e(z_e)\phi_h(z_h), \tag{2.16}$$

where $V=\int d\boldsymbol{r}_{CM}$ is the integrating volume, and the wavefunction consists of four parts representing free particles from the center-of-mass solution, relative solution, and wavefunction of electron and hole along the growth axis. Then replacing the wavefunction from Eq. (2.15) with the Eq. (2.16), we have

$$\begin{aligned}\left[\frac{\widehat{p}_{RM}^2}{2m_{RM}^*}-\frac{e^2}{4\pi\varepsilon_r\varepsilon_0|\boldsymbol{r}_{RM}|}+V_e(z_e)+V_h(z_h)\right]&\psi_{n,\boldsymbol{k}_{CM}}^{RM}(\boldsymbol{r}_{RM})\phi_e(z_e)\phi_h(z_h)\\&=\left(E_{X,n,\boldsymbol{k}_{CM}}-\underbrace{\frac{\hbar^2}{2m_{CM}^*}\boldsymbol{k}_{CM}^2}_{\text{kinetic energy of exciton}}\right)\psi_{n,\boldsymbol{k}_{CM}}^{RM}(\boldsymbol{r}_{RM})\phi_e(z_e)\phi_h(z_h),\end{aligned} \tag{2.17}$$

where the kinetic energy in the CM coordinate is the kinetic energy of the exciton. In the following, we will show two siturations where exciton is in bulk lattices and in ideal 2D QW.

Bulk lattice

If we neglect the confinement along the z-axis, the confining potential in the Hamiltonian, as well as the confining wavefunction of electron and hole along the z-axis, disappear, namely

$$\left(\frac{\widehat{p}_{RM}^2}{2m_{RM}^*}-\frac{e^2}{4\pi\varepsilon_r\varepsilon_0|\boldsymbol{r}_{RM}|}\right)\psi_{n,\boldsymbol{k}_{CM}}^{BULK}(\boldsymbol{r}_{RM})=\left(E_{X,n,\boldsymbol{k}_{CM}}^{BULK}-\frac{\hbar^2}{2m_{CM}^*}\boldsymbol{k}_{CM}^2\right)\psi_{n,\boldsymbol{k}_{CM}}^{BULK}(\boldsymbol{r}_{RM}), \tag{2.18}$$

where $\psi^{BULK}_{n,\boldsymbol{k}_{CM}}(\boldsymbol{r}_{RM})$ is the exciton wavefunction for the bulk materials. In this case, the exciton is very similar to the hydrogen atom. Solving Eq. (2.18) will give us the ground state (1s state) wavefunction of the exciton (hereafter, notation 1s is used to refer to case when $n = 1$)

$$\psi^{BULK}_{1s}(r_{RM}) = \frac{1}{\sqrt{\pi} a^{BULK\,3/2}_{Bohr}} e^{-r_{RM}/a^{BULK}_{Bohr}} \tag{2.19}$$

with Bohr radius

$$a^{BULK}_{Bohr} = \frac{4\pi\hbar^2\varepsilon_r\varepsilon_0}{m^*_{RM}e^2}. \tag{2.20}$$

And, the exciton energy for 3D bulk material with different principle quantum number n is

$$E^{BULK}_{X,n,\boldsymbol{k}_{CM}} = \frac{\hbar^2}{2m_{CM}}\boldsymbol{k}^2_{CM} - E^{BULK}_{binding,n}, \tag{2.21}$$

where the first term on the right-hand side (RHS) of Eq. (2.21) is the kinetic energy of the exciton and the binding energy of exciton inside the bulk material $E^{BULK}_{binding,n}$ is given by

$$E^{BULK}_{binding,n} = \frac{E_{Rydberg}}{n^2} \tag{2.22}$$

with the Rydberg energy analogy to the hydrogen atom

$$E_{Rydberg} = \frac{m^*_{RM}e^4}{32\pi^2\hbar^2\varepsilon_r^2\varepsilon_0^2}. \tag{2.23}$$

The Rydberg energy $E_{Rydberg}$ differs from different materials; for example, the Rydberg energy of GaAs, the commonly used semiconductor material, is around 4.8 meV but for Cu_2O it can reach even around 98.0 meV. The exciton formed by the latter is called the Rydberg exciton due to its large binding energy, and the maximum principle quantum number observed by the experiment is up to $n = 25$ [32], which shows a contrast that in GaAs due to a smaller Rydberg energy, theoretically even for very low temperature (1.35 K) the maximum n that can be obtained is around 6 before it is ionized [33].

Quantum well

Taking into account the confinement from the growth direction, the QW can be considered a 2D system. Due to the confining energy from the growth axis, the energy for 2D

QW is given by adding an extra energy term from Eq. (2.21)

$$E^{QW}_{X,n,\boldsymbol{k}_{CM,\parallel}} = \frac{\hbar^2}{2m^*_{CM}}\boldsymbol{k}^2_{CM,\parallel} - E^{QW}_{binding,n} + E^{QW}_{confining}, \tag{2.24}$$

where we have replaced the wavevector with the one in 2D, and the last term on the RHS of Eq. (2.24) refers to the confining energy. The differences between heavy hole and light hole are mentioned in section 2.2.2.1 since they have different effective masses. Moreover, Using the cylindrical coordinate system for relative motion $\boldsymbol{r}_{RM} = (\boldsymbol{\rho}, z)$, the wavefunction for the relative motion is given by [30]

$$\left[-\frac{\hbar^2}{2m^*_{RM}}\frac{1}{\rho}\frac{\partial}{\partial\rho}\left(\rho\frac{\partial}{\partial\rho}\right) - \frac{e^2}{\varepsilon_r\varepsilon_0\rho}\right]\psi^{QW}_n(\rho) = E^{QW}_{binding,n}\psi^{QW}_n(\rho). \tag{2.25}$$

The solution of Eq. (2.25) gives ground state ($1s$ state) of the exciton in a 2D system:

$$\psi^{QW}_{1s}(\rho) = \sqrt{\frac{2}{\pi}}\frac{1}{a^{QW}_{Bohr}}e^{-\rho/a^{QW}_{Bohr}} \tag{2.26}$$

with the Bohr radius of the exciton in QW

$$a^{QW}_{Bohr} = \frac{1}{2}a^{BULK}_{Bohr}. \tag{2.27}$$

And the binding energy from Eq.(2.24) for different quantum principle number is given by

$$E^{QW}_{binding,n} = \frac{E_{Rydberg}}{(n-\frac{1}{2})^2}. \tag{2.28}$$

Thus, for the ground state, we have $E^{QW}_{binding,1s} = 4E^{BULK}_{binding,1s}$. Through QW, the exciton can not only be confined in 2D and treated as a 2D material but could also enhance the exciton coupling with light due to the smaller Bohr radius in QW.

2.2.2.3 Optical transition

To understand the optical selection rule of the GaAs lattice, it is crucial to know the type of orbital of the CB and VB. The electron configurations of Ga and As are $[\mathrm{Ar}]3\mathrm{d}^{10}4\mathrm{s}^2\mathrm{4p}^1$ and $[\mathrm{Ar}]3\mathrm{d}^{10}4\mathrm{s}^2\mathrm{4p}^3$, respectively. The outermost shells of Ga and As have, respectively, 3 and 5 valence electrons. For both Ga and As, the s and p orbitals can hybridize to form four sp^3 orbitals; then the empty $4p$ orbital of Ga can combine with the half-filled $4p$ orbital of As to form a covalent bond. Eventually, the GaAs crystal forms through the sharing of valence electrons between the Ga and As atoms in a tetrahedral arrangement. The GaAs semiconductor considered in this thesis is also called a sp^3 semiconductor.

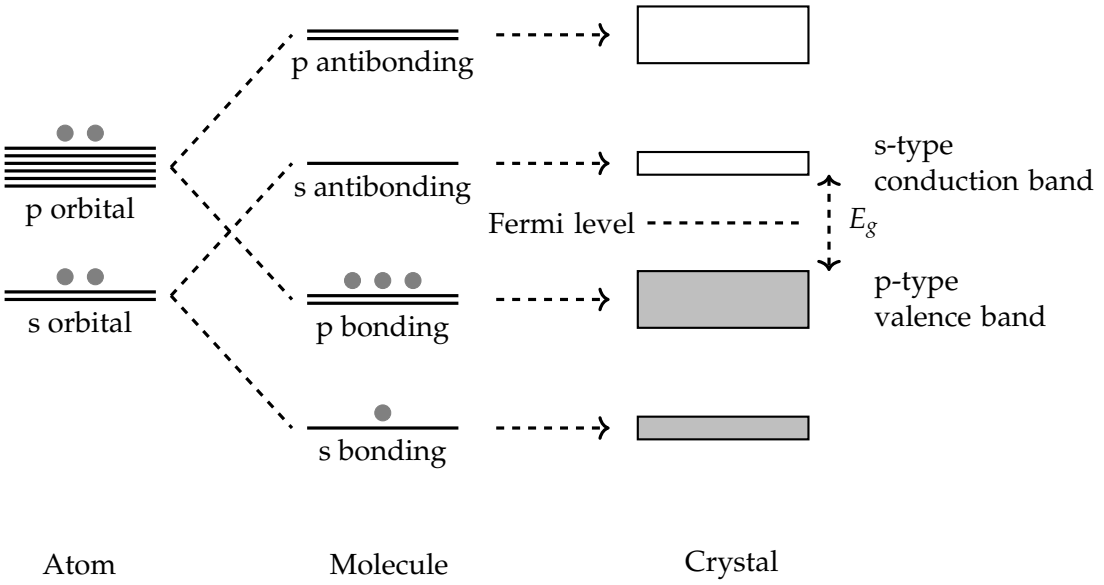

FIGURE 2.6: Illustration of the formation of the sp^3 semiconductor under the linear combination of atomic orbitals method. (Left column) Orbital s and p of the valence electrons of a single atom. (middle column) Pairing of Ga and As atoms. (right column) A large number of molecules form the crystal where the conduction band is s-type and the valence band is p-type. E_g is the band gap between the conduction band and the valence band. The gray dots symbolize different electron states. (Figure is adapted from Ref. [34])

According to the linear combination of atomic orbitals (LCAO) method, the molecule orbitals can be obtained by the supposition of different atomic orbitals. As illustrated in Fig. 2.6, the closed valence band and the conduction band closed to the Fermi level, originating from the molecules, inherit the orbital property from the p bonding (occupied state) and the s antibonding (empty state), respectively. Thus, the optical selection rule between the s-type and the p-type bands is taken into consideration for the GaAs lattice. The atomic band structure shown in Fig. 2.6 is a simplified atomic model that refers to the atom with four outer electrons because the average number of valence electrons of a single GaAs molecule is four.

The exciton is formed through photon stimulation with an energy larger than E_g [see Fig. 2.6 or Fig. 2.5], and certain transitions between VB and CB show the preference of photon with a certain polarization. The electrons in VB and CB can be described by the orbital angular momentum quantum number l and the spin quantum number m_s. Without SOI, the CB wavefunction is of type s, we have state $|l = 0, m_s = \frac{1}{2}\rangle$. Considering the SOI, the state can be further split into two bands with $|j = \frac{1}{2}, m_j = \pm\frac{1}{2}\rangle$ where $j = l + m_s$ defines the total angular momentum quantum number and $m_j = -j, -j + 1, \cdots, j - 1, j$ is its corresponding projection on the z-axis. The VB wavefunction is of type p with state $|l = 1, m_s = \frac{1}{2}\rangle$ in the absence of SOI and $|j = \frac{1}{2}, m_j = \pm\frac{1}{2}\rangle$ (light hole band) and $|j = \frac{3}{2}, m_j = \pm\frac{3}{2}\rangle$ (heavy hole band) in the presence of SOI. Figure 2.7 shows the splitting of the bands from the edge of the band in the QW, and due to the confining

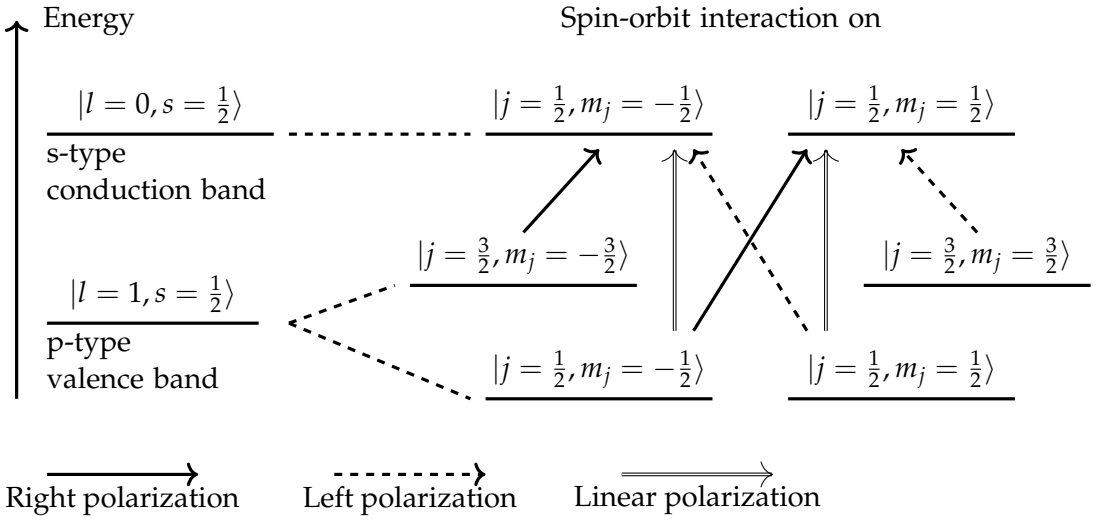

FIGURE 2.7: Optical selection rules for the zinc-blende quantum well. The energy band is shown at the band edge, and the splitting between the heavy hole and light hole is shown as a result of the confinement along the growth axis. (Figure is adapted from Ref. [30])

energy of the growth axis of the QW, the splitting between the heavy hole and the light hole is also illustrated.

If we denote m_j^{ph} the spin angular momentum quantum number of the photon, for the light with right circular polarization, we have $m_j^{ph} = +1$ and for left polarized light we have $m_j^{ph} = -1$. The optical selection rule can be explained in spin conservation: for stimulation from a right-polarized photon, the electron in the heavy hole with $m_j = -\frac{3}{2}$ can transit to the CB with $m_j = -\frac{1}{2}$ under the condition that the addition of m_j of both photon and the heavy hole is equal to the m_j of state from the conduction band. Figure 2.7 lists all possible transitions and notes that for linear polarized light, we have $m_j = 0$. Also, linear polarization is the superposition of right- and left-polarized light.

2.2.2.4 Bosonic approximation

Using the language of second quantization, the Hamiltonian of the electron-hole system can be simplified to a two-band system containing only the VB and CB. Thus, the total Hamiltonian is divided into the part containing only the self-energy from electrons

and holes, and the part considering the scattering among them

$$\begin{aligned}\widehat{H}_X &= \underbrace{\sum_{\boldsymbol{k}_\parallel}\hbar\omega_{CB}(\boldsymbol{k}_\parallel)\hat{c}^\dagger_{CB,\boldsymbol{k}_\parallel}\hat{c}_{CB,\boldsymbol{k}_\parallel}+\sum_{\boldsymbol{k}_\parallel}\hbar\omega_{VB}(\boldsymbol{k}_\parallel)\hat{c}^\dagger_{VB,\boldsymbol{k}_\parallel}\hat{c}_{VB,\boldsymbol{k}_\parallel}}_{\text{Self-energy of electrons and holes}} \\ &+\underbrace{\frac{1}{2}\sum_{\boldsymbol{q}\neq 0,\boldsymbol{k}'_\parallel,\boldsymbol{k}''_\parallel}V(\boldsymbol{q})\left(\hat{c}^\dagger_{CB,\boldsymbol{k}'_\parallel+\boldsymbol{q}}\hat{c}^\dagger_{CB,\boldsymbol{k}''_\parallel-\boldsymbol{q}}\hat{c}_{CB,\boldsymbol{k}''_\parallel}\hat{c}_{CB,\boldsymbol{k}'_\parallel}+\hat{c}^\dagger_{VB,\boldsymbol{k}'_\parallel+\boldsymbol{q}}\hat{c}^\dagger_{VB,\boldsymbol{k}''_\parallel-\boldsymbol{q}}\hat{c}_{VB,\boldsymbol{k}''_\parallel}\hat{c}_{VB,\boldsymbol{k}'_\parallel}\right)}_{\text{electron-electron and hole-hole interaction}} \\ &+\underbrace{\sum_{\boldsymbol{q}\neq 0,\boldsymbol{k}'_\parallel,\boldsymbol{k}''_\parallel}V(\boldsymbol{q})\hat{c}^\dagger_{CB,\boldsymbol{k}'_\parallel+\boldsymbol{q}}\hat{c}^\dagger_{VB,\boldsymbol{k}''_\parallel-\boldsymbol{q}}\hat{c}_{VB,\boldsymbol{k}''_\parallel}\hat{c}_{CB,\boldsymbol{k}'_\parallel}}_{\text{electron-hole interaction}},\end{aligned} \tag{2.29}$$

where $\omega_{CB}(\boldsymbol{k}_\parallel)$ ($\omega_{VB}(\boldsymbol{k}_\parallel)$) is the angular frequency of the electron from CB (VB) as the function of in-plane wavevector $\boldsymbol{k}_\parallel$, $V(\boldsymbol{q})$ stands for the Coulomb interaction in Fourier space, and $\hat{c}_{CB,\boldsymbol{k}_\parallel}$ ($\hat{c}_{VB,\boldsymbol{k}_\parallel}$) and $\hat{c}^\dagger_{CB,\boldsymbol{k}_\parallel}$ ($\hat{c}^\dagger_{VB,\boldsymbol{k}_\parallel}$) are annihilation operator and creation operator of an electron from CB (VB) with in-plane wavector $\boldsymbol{k}_\parallel$, respectively. Noting that the expression of Eq. (2.29) is retained because the ω_{CB} and ω_{VB} versus in-plane wavevector is still considered positive upward and negative downward form, as shown in Fig. 2.5. The Hamiltonian of Eq. (2.29) can be diagonalized into the form

$$\widehat{H}_X=\sum_{\boldsymbol{k}_\parallel}\hbar\omega_X(\boldsymbol{k}_\parallel)\hat{b}^\dagger_{\boldsymbol{k}_\parallel}\hat{b}_{\boldsymbol{k}_\parallel}, \tag{2.30}$$

where $\hat{b}^\dagger_{\boldsymbol{k}_\parallel}$ ($\hat{b}_{\boldsymbol{k}_\parallel}$) is the bosonic operator standing for the creation (annihilation) of an exciton at in-plane wavevector $\boldsymbol{k}_\parallel$ which can be considered as CM wavevector we defined in section 2.2.2.2. For brevity, assuming that only the direct transition from VB to CB is considered, the expression of the excitonic creation operator is described by

$$\hat{b}^\dagger_{n,\boldsymbol{k}_\parallel}=\sum_{\boldsymbol{q}}\phi_n(\boldsymbol{q})\hat{c}^\dagger_{CB,\boldsymbol{k}_\parallel/2+\boldsymbol{q}}\hat{c}_{VB,\boldsymbol{k}_\parallel/2-\boldsymbol{q}} \tag{2.31}$$

in which $\phi_n(\boldsymbol{k}_\parallel)$ is the Fourier transform of the exciton wavefunction of n-th state. Eq. (2.31) describes the transition from VB to CB that forms excitons by annihilating an electron from VB with the in-plane wavevector $\boldsymbol{k}_\parallel/2-\boldsymbol{q}$ and creating an electron from CB with the in-plane wavevector $\boldsymbol{k}_\parallel/2+\boldsymbol{q}$. To ensure the Boson-like operator

from Eq. (2.31) satisfy the bosonic commutation relation, we arrive at:

$$\begin{aligned}
[\hat{b}_{n,\boldsymbol{k}_\parallel}, \hat{b}^\dagger_{n',\boldsymbol{k}'_\parallel}] &= \sum_{\boldsymbol{q},\boldsymbol{q}'} \phi^*_n(\boldsymbol{q})\phi_{n'}(\boldsymbol{q}')\left[\hat{c}^\dagger_{VB,\boldsymbol{k}_\parallel/2-\boldsymbol{q}}\hat{c}_{CB,\boldsymbol{k}_\parallel/2+\boldsymbol{q}}, \hat{c}^\dagger_{CB,\boldsymbol{k}'_\parallel/2+\boldsymbol{q}'}\hat{c}_{VB,\boldsymbol{k}'_\parallel/2-\boldsymbol{q}'}\right] \\
&= \sum_{\boldsymbol{q}} |\phi_n(\boldsymbol{q})|^2\delta_{n,n'}\delta_{\boldsymbol{k}_\parallel,\boldsymbol{k}'_\parallel} - \sum_{\boldsymbol{q},\boldsymbol{q}'} \phi^*_n(\boldsymbol{q})\phi_{n'}(\boldsymbol{q}')\hat{c}_{VB,\boldsymbol{k}'_\parallel/2-\boldsymbol{q}'}\hat{c}^\dagger_{VB,\boldsymbol{k}_\parallel/2-\boldsymbol{q}}\delta_{\boldsymbol{k}_\parallel/2+\boldsymbol{q},\boldsymbol{k}'_\parallel/2+\boldsymbol{q}'} \\
&\quad - \sum_{\boldsymbol{q},\boldsymbol{q}'} \phi^*_n(\boldsymbol{q})\phi_{n'}(\boldsymbol{q}')\hat{c}^\dagger_{CB,\boldsymbol{k}'_\parallel/2+\boldsymbol{q}'}\hat{c}_{CB,\boldsymbol{k}_\parallel/2+\boldsymbol{q}}\delta_{\boldsymbol{k}_\parallel/2-\boldsymbol{q},\boldsymbol{k}'_\parallel/2-\boldsymbol{q}'} \\
&= \delta_{n,n'}\delta_{\boldsymbol{k}_\parallel,\boldsymbol{k}'_\parallel} - \sum_{\boldsymbol{q}} \phi^*_n(\boldsymbol{q})\phi_{n'}(\boldsymbol{k}_\parallel/2-\boldsymbol{k}'_\parallel/2+\boldsymbol{q})\hat{c}_{VB,\boldsymbol{k}'_\parallel-\boldsymbol{k}_\parallel/2-\boldsymbol{q}}\hat{c}^\dagger_{VB,\boldsymbol{k}_\parallel/2-\boldsymbol{q}} \\
&\quad - \sum_{\boldsymbol{q}} \phi^*_n(\boldsymbol{q})\phi_{n'}(\boldsymbol{k}'_\parallel/2-\boldsymbol{k}_\parallel/2+\boldsymbol{q})\hat{c}^\dagger_{CB,\boldsymbol{k}'_\parallel-\boldsymbol{k}_\parallel/2+\boldsymbol{q}}\hat{c}_{CB,\boldsymbol{k}_\parallel/2+\boldsymbol{q}}. \qquad (2.32)
\end{aligned}$$

Define $[A,B] = AB - BA$ and $\{A,B\} = AB + BA$, respectively, the commutator and anticommutator. To derive Eq. (2.32), the relations

$$\{\hat{c}_{k_1}, \hat{c}_{k_2}\} = 0, \quad \{\hat{c}^\dagger_{k_1}, \hat{c}^\dagger_{k_2}\} = 0, \quad \{\hat{c}_{k_1}, \hat{c}^\dagger_{k_2}\} = \delta_{k_1,k_2}, \qquad (2.33)$$

$$[\hat{c}_{k_1}, \hat{c}_{k_2}] = 0, \quad [\hat{c}^\dagger_{k_1}, \hat{c}^\dagger_{k_2}] = 0, \quad [\hat{c}_{k_1}, \hat{c}^\dagger_{k_2}] = \delta_{k_1,k_2} - 2\hat{c}^\dagger_{k_2}\hat{c}_{k_1}, \qquad (2.34)$$

$$[\hat{c}^\dagger_{k_1}\hat{c}_{k_2}, \hat{c}^\dagger_{k_3}\hat{c}_{k_4}] = \hat{c}^\dagger_{k_1}\hat{c}_{k_4}\delta_{k_2,k_3} - \hat{c}^\dagger_{k_3}\hat{c}_{k_2}\delta_{k_1,k_4}, \qquad (2.35)$$

are used. Applying the ground state $|G\rangle$, indicating all the electrons are below the Fermi level, to the communication relation of Eq. (2.32), and assuming all the transitions are in the vicinity of the band edge, namely, $|\boldsymbol{k}_\parallel| \approx 0$, we have

$$\langle G|[\hat{b}_{1s,\boldsymbol{0}}, \hat{b}^\dagger_{1s,\boldsymbol{0}}]|G\rangle = 1 - \sum_{\boldsymbol{q}} |\phi_{1s}(\boldsymbol{q})|^2 \approx 1 - \mathcal{O}[N_X {a^{QW}_{Bohr}}^2], \qquad (2.36)$$

in which N_X is the 2D excition density. Equation (2.36) shows that the bosonic approximation is still held in the low-density regime, where the number of excitons is low-density. Such an upper limit of sets of all the possible densities that the bosonic approximation still holds is also called the Mott density.

2.2.3 Strong coupling between Excitons and photons

The cavity quantum electrodynamics, dating back to the discovery of the Purcell effect in 1946 [1], has been playing a key role in light-matter interaction. Although the Purcell effect reveals the realization of enhancement of the spontaneous emission rate by tailoring the cavity environment, it is still limited in the weak coupling regime because the losses exceed the coupling strength. With the development of semiconductor device fabrication and cavity system, the coupling strength surpassing the damping was achieved for the first time bringing the SC regime into reality [3].

With photonic stimulation, electrons in the valence band below the Fermi level can transit to the conduction band, leaving a hole with a positive charge. Such an electron-hole pair that is a kind of quasiparticle is called an exciton. The Jaynes-Cummings model describing the exciton-light coupling is

$$\widehat{H} = \underbrace{\sum_{\boldsymbol{k}_\parallel} \hbar\omega_{C,\boldsymbol{k}_\parallel} \hat{a}^\dagger_{\boldsymbol{k}_\parallel} \hat{a}_{\boldsymbol{k}_\parallel} + \sum_{\boldsymbol{k}_\parallel} \hbar\omega_{X,\boldsymbol{k}_\parallel} \hat{b}^\dagger_{\boldsymbol{k}_\parallel} \hat{b}_{\boldsymbol{k}_\parallel}}_{\widehat{H}_0} + \underbrace{\sum_{\boldsymbol{k}_\parallel} \hbar\Omega_{R,\boldsymbol{k}_\parallel} (\hat{a}^\dagger_{\boldsymbol{k}_\parallel} \hat{b}_{\boldsymbol{k}_\parallel} + \hat{a}_{\boldsymbol{k}_\parallel} \hat{b}^\dagger_{\boldsymbol{k}_\parallel})}_{\widehat{H}_I}, \tag{2.37}$$

where $\hat{a}_{\boldsymbol{k}_\parallel}$ ($\hat{a}^\dagger_{\boldsymbol{k}_\parallel}$) the annihilation (creation) operator of the photon with in-plane wavevector $\boldsymbol{k}_\parallel$, $\omega_{C,\boldsymbol{k}_\parallel}$ and $\omega_{X,\boldsymbol{k}_\parallel}$ are the angular frequency of cavity and excitons, respectively, and $\Omega_{R,\boldsymbol{k}_\parallel}$, also refers to Rabi frequency, is the coupling strength between the exciton and photon. The total Hamiltonian is divided into two parts: the bare energy of excitons and photons $\widehat{H}_0$ and the Hamiltonian of the interaction $\widehat{H}_I$. Note that the decaying term has been neglected for simplicity, and in the SC regime, we have the relation $\Omega_{R,\boldsymbol{k}_\parallel} \gg \Omega_{loss}$ where Ω_{loss} represents all possible losses in the system. Furthermore, it is worth mentioning that when the Rabi frequency is comparable with the bare frequency of the components of the system (e.g., ω_C and ω_X), we say the system enters the ultrastrong coupling (USC) regime and the rotation wave approximation used in $\widehat{H}_I$ of Eq. (2.37) is thus broken. The advantage of achieving USC is having faster energy exchange between light and matter and further introducing novel physical phenomena, such as squeezed vacuum state, virtual photons, and virtual excitations [35, 36].

Equation (2.37) can be transferred into a diagonalized form

$$\widehat{H} = \sum_{\boldsymbol{k}_\parallel} \hbar\Omega_{L,\boldsymbol{k}_\parallel} \widehat{P}^\dagger_{L,\boldsymbol{k}_\parallel} \widehat{P}_{L,\boldsymbol{k}_\parallel} + \sum_{\boldsymbol{k}_\parallel} \hbar\Omega_{U,\boldsymbol{k}_\parallel} \widehat{P}^\dagger_{U,\boldsymbol{k}_\parallel} \widehat{P}_{U,\boldsymbol{k}_\parallel}, \tag{2.38}$$

where $\Omega_{L,\boldsymbol{k}_\parallel}$ ($\Omega_{U,\boldsymbol{k}_\parallel}$) is the lower (upper) polariton frequency, $\widehat{P}_{L,\boldsymbol{k}_\parallel}$ ($\widehat{P}^\dagger_{L,\boldsymbol{k}_\parallel}$) the annihilation (creation) operator of the lower polariton branch (LP), $\widehat{P}_{U,\boldsymbol{k}_\parallel}$ ($\widehat{P}^\dagger_{U,\boldsymbol{k}_\parallel}$) is the upper polariton branch (UP). And these polariton operators are defined by

$$\widehat{P}_{L,\boldsymbol{k}_\parallel} = \nu_{L,\boldsymbol{k}_\parallel} \hat{a}_{\boldsymbol{k}_\parallel} + \chi_{L,\boldsymbol{k}_\parallel} \hat{b}_{\boldsymbol{k}_\parallel}, \tag{2.39}$$

$$\widehat{P}_{U,\boldsymbol{k}_\parallel} = \nu_{U,\boldsymbol{k}_\parallel} \hat{a}_{\boldsymbol{k}_\parallel} + \chi_{U,\boldsymbol{k}_\parallel} \hat{b}_{\boldsymbol{k}_\parallel}, \tag{2.40}$$

in which ν and χ, reveling the ratio of the excitonic and photonic part in this polaritonic system, refer to Hopfield coefficients [37]. Since the bosonic commutation $[\widehat{P}_{L,\boldsymbol{k}_\parallel}, \widehat{P}^\dagger_{L,\boldsymbol{k}'_\parallel}] = \delta_{\boldsymbol{k}_\parallel,\boldsymbol{k}'_\parallel}$, $[\widehat{P}_{U,\boldsymbol{k}_\parallel}, \widehat{P}^\dagger_{U,\boldsymbol{k}'_\parallel}] = \delta_{\boldsymbol{k}_\parallel,\boldsymbol{k}'_\parallel}$, $[\widehat{P}_{L,\boldsymbol{k}}, \widehat{P}^\dagger_{U,\boldsymbol{k}}] = 0$, and $[\widehat{P}_{U,\boldsymbol{k}}, \widehat{P}^\dagger_{L,\boldsymbol{k}}] = 0$ are held, we arrive at

$$|\nu_{L,\boldsymbol{k}_\parallel}|^2 + |\chi_{L,\boldsymbol{k}_\parallel}|^2 = 1, \tag{2.41}$$

$$|\nu_{U,\boldsymbol{k}_\parallel}|^2 + |\chi_{U,\boldsymbol{k}_\parallel}|^2 = 1, \tag{2.42}$$

$$\nu_{L,\boldsymbol{k}} \nu^*_{U,\boldsymbol{k}} + \chi_{L,\boldsymbol{k}} \chi^*_{U,\boldsymbol{k}} = 0. \tag{2.43}$$

Given that the system is free of losses or gains, both ν and χ are inherently real values, thereby the complex conjugate symbol can be omitted. From Eqs. (2.41), (2.42), and (2.43), the polariton operators defined from Eqs. (2.39) and (2.40) can be further simplified to

$$\widehat{P}_{L,\boldsymbol{k}_\parallel} = \nu_{L,\boldsymbol{k}_\parallel}\hat{a}_{\boldsymbol{k}_\parallel} + \chi_{L,\boldsymbol{k}_\parallel}\hat{b}_{\boldsymbol{k}_\parallel}, \tag{2.44}$$

$$\widehat{P}_{U,\boldsymbol{k}_\parallel} = \chi_{L,\boldsymbol{k}_\parallel}\hat{a}_{\boldsymbol{k}_\parallel} - \nu_{L,\boldsymbol{k}_\parallel}\hat{b}_{\boldsymbol{k}_\parallel}. \tag{2.45}$$

Substituting Eqs. (2.44) and (2.45) into Eq. (2.38), and making the comparison with the Eq. (2.37), we have

$$\omega_{C,\boldsymbol{k}_\parallel} = \Omega_{L,\boldsymbol{k}_\parallel}|\nu_{L,\boldsymbol{k}_\parallel}|^2 + \Omega_{U,\boldsymbol{k}_\parallel}|\chi_{L,\boldsymbol{k}_\parallel}|^2, \tag{2.46}$$

$$\omega_{X,\boldsymbol{k}_\parallel} = \Omega_{L,\boldsymbol{k}_\parallel}|\chi_{L,\boldsymbol{k}_\parallel}|^2 + \Omega_{U,\boldsymbol{k}_\parallel}|\nu_{L,\boldsymbol{k}_\parallel}|^2, \tag{2.47}$$

$$\Omega_{R,\boldsymbol{k}_\parallel} = \Omega_{L,\boldsymbol{k}_\parallel}\nu_{L,\boldsymbol{k}_\parallel}\chi_{L,\boldsymbol{k}_\parallel} - \Omega_{U,\boldsymbol{k}_\parallel}\chi_{L,\boldsymbol{k}_\parallel}\nu_{L,\boldsymbol{k}_\parallel}, \tag{2.48}$$

Through solving Eqs. (2.41), (2.46), (2.47), and (2.48), we obtain $\Omega_{L,\boldsymbol{k}_\parallel}$ and $\Omega_{U,\boldsymbol{k}_\parallel}$ as a function of $\omega_{C,\boldsymbol{k}_\parallel}$, $\omega_{X,\boldsymbol{k}_\parallel}$, and $\Omega_{R,\boldsymbol{k}_\parallel}$,

$$\Omega_{L,\boldsymbol{k}_\parallel} = \frac{1}{2}\left(\omega_{C,\boldsymbol{k}_\parallel} + \omega_{X,\boldsymbol{k}_\parallel}\right) - \sqrt{\frac{1}{4}\Delta_{\boldsymbol{k}_\parallel}^2 + \Omega_{R,\boldsymbol{k}_\parallel}^2}, \tag{2.49}$$

$$\Omega_{U,\boldsymbol{k}_\parallel} = \frac{1}{2}\left(\omega_{C,\boldsymbol{k}_\parallel} + \omega_{X,\boldsymbol{k}_\parallel}\right) + \sqrt{\frac{1}{4}\Delta_{\boldsymbol{k}_\parallel}^2 + \Omega_{R,\boldsymbol{k}_\parallel}^2}, \tag{2.50}$$

where

$$\Delta_{\boldsymbol{k}_\parallel} = \omega_{C,\boldsymbol{k}_\parallel} - \omega_{X,\boldsymbol{k}_\parallel}. \tag{2.51}$$

The frequency difference between the lower and upper polariton is $2\sqrt{\frac{1}{4}\Delta_{\boldsymbol{k}_\parallel}^2 + \Omega_{R,\boldsymbol{k}_\parallel}^2}$, and the minimum value is achieved when $\Delta_{\boldsymbol{k}_\parallel} = 0$, that is, the bare frequencies of both microcavity photon and exciton are equal. In this simplified model, the minimal frequency between the lower and upper polariton is exact $2\Omega_{R,\boldsymbol{k}_\parallel}$ which is also called the Rabi splitting frequency. The Hopfield coefficients of the lower polariton are

$$|\chi_{L,\boldsymbol{k}_\parallel}|^2 = \frac{1}{2}\left(1 + \frac{\Delta_{\boldsymbol{k}_\parallel}}{\sqrt{4\Omega_{R,\boldsymbol{k}_\parallel}^2 + \Delta_{\boldsymbol{k}_\parallel}^2}}\right), \tag{2.52}$$

$$|\nu_{L,\boldsymbol{k}_\parallel}|^2 = \frac{1}{2}\left(1 - \frac{\Delta_{\boldsymbol{k}_\parallel}}{\sqrt{4\Omega_{R,\boldsymbol{k}_\parallel}^2 + \Delta_{\boldsymbol{k}_\parallel}^2}}\right). \tag{2.53}$$

The frequency of the microcavity photons is given in Eq. (2.1), and if we define the detuning energy δ such that at $|\boldsymbol{k}_\parallel| = 0$, we have $\delta = \hbar\Delta_{\boldsymbol{0}} = \hbar(\omega_{C,\boldsymbol{0}} - \omega_{X,\boldsymbol{0}})$. Thus, we

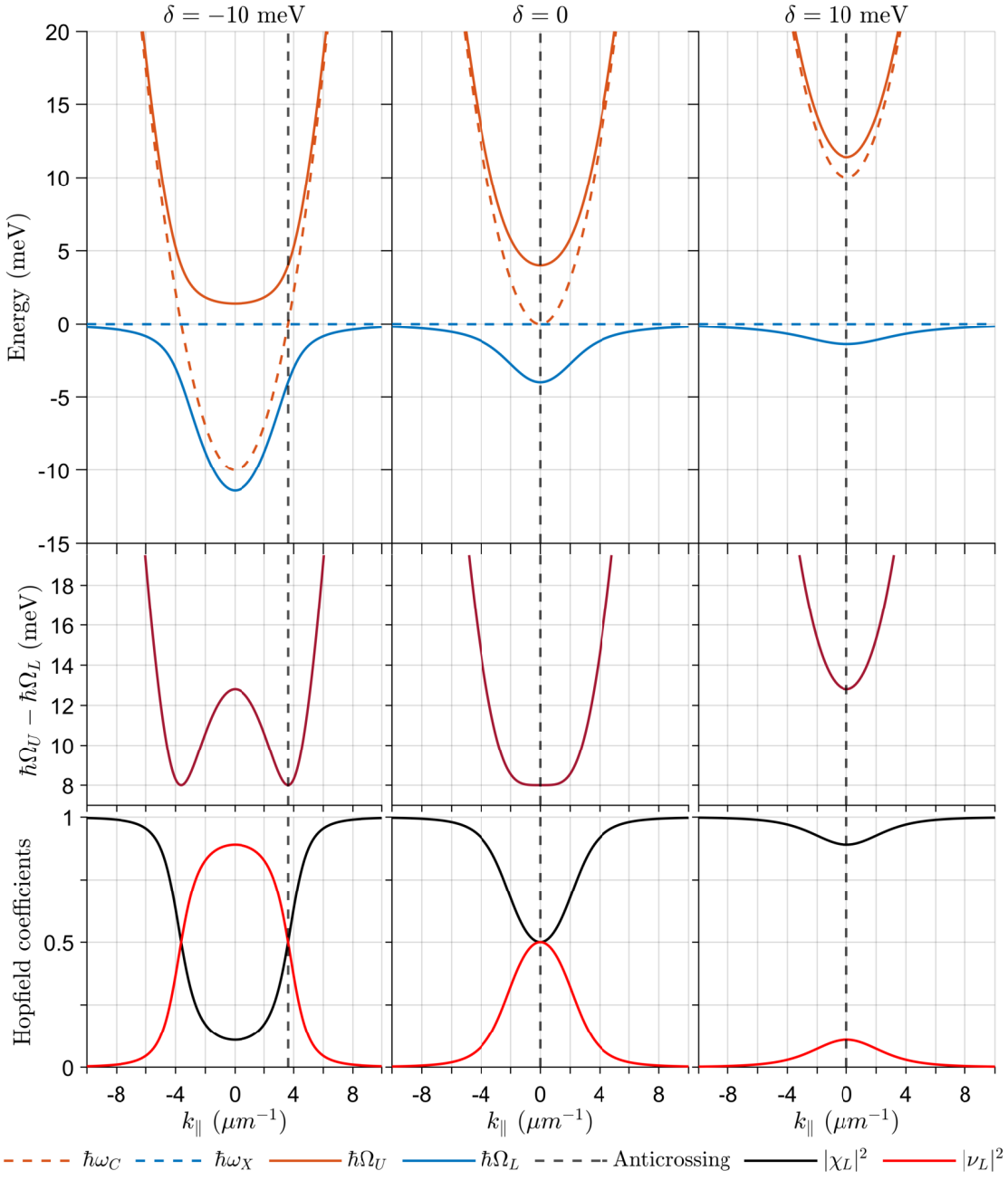

FIGURE 2.8: (Top panel) The spectrum of the polaritonic system as a function of the in-plane wavevector. The upper (lower) polariton branch is shown in the solid orange (blue) line, and the uncoupled bare energy of the cavity photons and exciton is, respectively, shown in the dashed orange and blue lines. (Middle panel) Energy difference between the upper and lower polariton. (Bottom panel) The Hopefield coefficients of the lower polariton. The red line refers to the photonic ratio and the black line represents the excitonic part. Parameters: $m_C^* = 5.0 \times 10^{-5}\, m_0$, $m_X^* = 0.6\, m_0$, and the coupling between the exciton and photon is taken as constant, with $\hbar\Omega_R = 4.0$ meV.

have

$$\hbar\omega_{C,k_\parallel} \approx \delta + \frac{\hbar^2}{2m_C^*}k_\parallel^2, \tag{2.54}$$

$$\hbar\omega_{X,k_\parallel} \approx \frac{\hbar^2}{2m_X^*}k_\parallel^2, \tag{2.55}$$

where we make the excitonic dispersion relation also follow the parabolic shape like what the microcavity photon does and m_X^* is the effective mass of the exciton. Since the exciton is much heavier than the microcavity photon, namely $m_X^* \gg m_C^*$, excitonic frequency is usually considered constant; however, the photonic frequency is more responsive to the in-plane wavevector.

The spectrum of polaritons with negative, zero, and positive detuning is shown in the top left, top middle, and top right panels of Fig. 2.8, respectively. The middle panels present the energy difference between the UP and LP, and there the minimum value means the Rabi energy in the top panels; besides, as shown in the black dashed line, at the exact position of the in-plane wavevector where the Rabi frequency and minimal energy difference take place, the difference of the Hopfield coefficients between the cavity mode and exciton mode of LP reaches the minimal, as shown in the bottom panels. Especially for the negative and zero detuning, at the anticrossing point, their Hopfield coefficients share 0.5 each, which means that the polariton consists of half photonic and half exciton components.

From the top panels of Fig. 2.8, it seems that anticrossing also takes place where the bare frequencies of the cavity mode and exciton mode cross, which is true when the system is in the SC regime while not in the USC regime. When the system is in the USC regime, the rotation wave approximation is broken; thus, the antiresonant term from the interaction term of Eq. (2.37) should also be taken into account, resulting in a blue shift in the in-plane wavevector for the Rabi frequency (see papers [35, 38] for examples from intersubband polariton).

2.3 Exciton polariton condensates

2.3.1 Ideal non-interacting Bose gas

Polaritons are bosonic quasiparticles at the low-density limit of electron-hole pairs. The Pauli exclusion principle states that electrons, being fermions with half-integer spin, cannot have more than two electrons per quantum state; however, the excitons, being the quasibosons with integer spin, can break the inherent limit from electrons'

fermionic nature. Recalling the Bose-Einstein statistics

$$f(E_i) = \frac{1}{e^{(E_i-\mu)/k_BT} - 1}, \tag{2.56}$$

where E_i is the energy of i-th state, k_B the Boltzmann constant, μ the chemical potential, and T is the temperature. For bosons, μ should be negative or zero; thus, the probability of finding a particle at ground state energy with $E_i = 0$, is close to infinity with $T \to 0$, while, the probability of finding particles at higher energy states is close to zero. When we increase the temperature, more particles at excited states are expected. Moreover, we can always set a special temperature T_{BE} such that the probability of finding the particle in the excited state is high enough to find N_B particles for all excited states. Thus, we arrive at

$$\sum_{i\in\{\text{excited states}\}} \frac{1}{e^{(E_i-\mu)/k_BT_{BE}} - 1} = N_B. \tag{2.57}$$

To obtain the threshold temperature T_{BE}, the sum over all the excited state in Eq. (2.57) can be transformed to continuum states, namely

$$\sum_{i\in\{\text{excited states}\}} = \int_0^\infty \rho(E)dE, \tag{2.58}$$

where

$$\rho(E) = \frac{Vm^{*3/2}}{\sqrt{2}\pi^2\hbar^3}\sqrt{E} \tag{2.59}$$

is the density of state in energy space of free bosons in 3D. Substituting Eqs. (2.58) and (2.59) into Eq. (2.57) and setting $\mu = 0$ from Eq. (2.57) due to the condition that there is only one particle at excited states at T_{BE}, we have

$$\frac{Vm^{*3/2}}{\sqrt{2}\pi^2\hbar^3}\int_0^\infty \frac{\sqrt{E}}{e^{E/k_BT_{BE}} - 1}dE = N_B. \tag{2.60}$$

The T_{BE} from Eq. (2.60) indicates that for $T \geqslant T_{BE}$, the number of bosons at excited states can exceed one. In other words, for $T < T_{BE}$, all the bosons are in the ground state. Thus, T_{BE} can be extracted through solving Eq. (2.60) and we have

$$T_{BE} = \frac{2\pi\hbar^2}{k_Bm^*}\Big[\frac{n}{\zeta(3/2)}\Big]^{2/3} \tag{2.61}$$

where $n = N_B/V$ is the density of bosons, and

$$\zeta(s) = \sum_{n=1}^{\infty}\frac{1}{n^s} = \frac{1}{\Gamma(s)}\int_0^\infty \frac{x^{s-1}}{e^x - 1}dx \tag{2.62}$$

is the Riemann zeta function and $\Gamma(s)$ is the Gamma function, and $\zeta(3/2) \approx 2.612$ is obtained from Eq. (2.62). In section 2.2.2, we have shown from an analytical perspective that to ensure the bosonic approximation of the electron-hole paired quasiparticles is still held, the low-density limit is required. Equation (2.61) describes that the lower the density of the boson gas, the higher the threshold temperature of condensates is; besides, the small effective mass can also increase the threshold temperature. This is why polariton is a good candidate because the light branch of polaritons contributes to the small effective mass. This is worth mentioning that Eq. (2.61) is only accurate for ideal noninteracting boson gas in 3D rather than for the polaritons produced in the quasi-2D QW systems. Still, it demonstrates the relation between effective mass, temperature, and density of the bosonic gas in achieving the phase transition with the Bose-Einstein condensates.

2.3.2 Exciton-polariton condensates

Thanks to the coupling with the photons, the effective mass is significantly light; for GaAs, around 10^{-5} of the electron mass can be obtained. Because the polaritons are Bose-like quasiparticles with much lighter effective mass than the bare electron, it is easier to produce condensation in such a system than in an atomic system. On the basis of the ideal bosonic model of Eq. (2.61), one expects a higher threshold temperature to produce the polariton condensates. Nonresonant and resonant pumping are two main methods of producing polariton condensates.

For the nonresonant pumping, in the beginning, the excitons with high energy are created through nonresonant pumping, then quickly releax to the LP accompanied by the longitudinal-optical phonon. Later on, the excitons keep cooling down on the LP through the exciton-exciton scattering or the interaction between the exciton and the acoustic photon, resulting in a further relaxation of excitons to a lower region of the LP. This region is usually called the "bottleneck" region, where the energy difference between the LP and UP is close to the Rabi frequency with a low scattering rate of the polariton and acoustic phonon. As the polariton on the bottleneck region accumulates to a certain degree over time, enhancement of the final-state stimulation is expected. Thus, parametric scattering describing that some polaritons quickly fall to the bottom of the LP, and some scatter to the higher-energy region of the LP, takes place, which eventually gives rise to the polariton condensates.

Let us explain this phonon relaxation in more detail. On the LP with high momentum, there are much more excitons than photons, so the quasiparticles there are still dominated by the excitons; in other words, we can say polariton with almost zero photonic components. When the excitons reach the bottleneck region, there are more photons resulting in polaritons with relatively short lifetime (more photonic components) compared to the exciton. Due to the short lifetime of the polaritons (ranging from 1 ps

to 100 ps), the coupling between the excitonic branch of the polariton and the acoustic phonon is less efficient because the relaxation time is comparable to the polariton lifetime. Parametric scattering, accompanied by energy and momentum conservation, causes the polaritons to fall to the lower momentum ($|\boldsymbol{k}_{\parallel}| \approx 0$ for zero or positive detuning or $|\boldsymbol{k}_{\parallel}| > 0$ for negative detuning [39]) of LP.

For resonant pumping, resonant polaritons are directly pumped into the bottom of the LP with zero in-plane momentum to produce the condensates.[2] In the thesis, we mainly consider the nonresonant pumping because of the rich nonlinearity occurring at not only the condensates but also the processing involved with the phonon-induced relativization and the parametric scattering.

If we define the threshold pumping power above which condensation occurs, the system's energy responds differently to the pumping power dependence. Note that we consider only continuous-wave (CW) pumping in this thesis. When the pumping power increases before reaching the threshold, the system's energy increases linearly to the input power; however, when it reaches the threshold power, the energy will quickly drop from the bottleneck region due to the parametric scattering; later on, the energy increases nonlinearly versus the pumping power due to the blue shift from the polariton-polariton interaction when the pumping power crosses the threshold. The condensation also brings about the phase transition from pumping to condensates.

2.3.3 Generalized Gross-Pitaevskii model

To numerically simulate the whole process, the system can be simplified into two parts: the reservoir and the condensates. The former is described through the rate equation involving pumping, scattering to the bottleneck, and condensates. The latter system, which encompasses the pumping, decay, and scattering processes involving the polariton-polariton interaction and the polariton-reservoir interaction, is characterized by the 2D generalized Gross-Pitaevskii equation (GPE). It is worth noting that the derivation of this GPE is based on the principles of mean-field theory, which simplifies complex interactions in the system. The GPE coupled with the reservoir rate equation

[2] Condensates can also be produced through resonant pumping directly into the region where the parametric scattering takes place with the highest scattering rate or somewhere with the lower or higher energy of the branch where the excitons can eventually scatter to the ground state but with lower scattering rate. For more details from the theoretical perspective of the parametric scattering, one may look at the review paper [40].

is given by [41]

$$
\begin{aligned}
i\hbar\frac{\partial}{\partial t}\Psi(t,\boldsymbol{r}_{\parallel}) &= \Big\{-\frac{\hbar^2}{2m^*}\nabla_{\parallel}^2+\alpha|\Psi(t,\boldsymbol{r}_{\parallel})|^2+G\Big[n_X(t,\boldsymbol{r}_{\parallel})+\frac{\eta}{\Gamma_X}P(\boldsymbol{r}_{\parallel})\Big] \\
&\quad +i\frac{\hbar}{2}\big[Rn_X(t,\boldsymbol{r}_{\parallel})-\gamma\big]\Big\}\Psi(t,\boldsymbol{r}_{\parallel}), \qquad (2.63)\\
\frac{\partial}{\partial t}n_X(t,\boldsymbol{r}_{\parallel}) &= -\big[\Gamma_X+R|\Psi(t,\boldsymbol{r}_{\parallel})|^2\big]n_X(t,\boldsymbol{r}_{\parallel})+P(\boldsymbol{r}_{\parallel}). \qquad (2.64)
\end{aligned}
$$

Equation (2.64) is the rate equation describing dynamics from the 2D nonresonant pump $P(\boldsymbol{r}_{\parallel})$ to the condensates; Γ_X is the damping term of the reservoir, and R is the scattering rate from the reservoir to the condensate. Equation (2.63), describing the dynamics of the condensates, where $G = 2g|\chi|^2$ and $\alpha = g|\chi|^4$ are the polariton-reservoir and polariton-polariton interaction strengths, respectively, g is the exciton-exciton dipole interaction strength, $|\chi|^2$ is the excitonic Hopfield fraction of the polariton introduced in section 2.2.3; γ is the decay rate of the polariton, and η quantifies additional blueshift coming from dark excitons which do not scatter into the condensate.

To avoid solutions containing "Not a Number" (known as NaN), in numerical computing, at each spatial point, the initial condition of Ψ is assigned with the complex random noises defined by

$$\Psi_{t=0} = \varepsilon, \qquad (2.65)$$

where

$$\varepsilon = 10^{-16}(g_{\text{rand}} + ig_{\text{rand}}). \qquad (2.66)$$

Notice that the two random number generator g_{rand} shown above usually differ for real and imaginargy part of the wavefunction. The condition of Eq. (2.65) is applied for this thesis, when it comes to the numerical solution to the GPE. Also, in chapter 3, since using the split-step Fourier method, computing is prepared in multiple infinitesimal time steps. At each time step, the complex noise ε is also applied at each time step.

The formalism of polariton condensates shown in Eq. (2.63) is valid under the condition of linear pumping that produces the equal number of spin-up and spin-down polaritons, as demonstrated in Fig. 2.7. For the uncoupled components of the polariton, in the presence of the magnetic field, the energy of the cavity mode remains the same, but the exciton energy is modified by the Zeeman effect and the diamagnetic shift. As shown in Fig. (2.8), this shift in exciton energy alters the detuning, suggesting that a majority of the interactions, such as scattering from the reservior to the condensate, polariton-polariton interactions, and polariton-reservoir interactions, depend on the magnetic field. It turns out that the inherent properity of the polaritons is also modified by the

magnetic field. Furthermore, the interaction and scattering among the polariton and reservoir excitons with spin-up and spin-down configurations are not included, which goes beyond the scope of the formalism discussed here involving spinless polaritons. Consequently, Eqs. (2.63) and (2.64) are no longer applicable in this context. Please see Ref. [30] for more details including polarization properties of polaritons.

2.3.3.1 Linear regime

The nonlinear term can be omitted if the pumping strength is just above the threshold. Thus, $|\Psi| \approx 0$ can be replaced in Eqs. (2.63) and (2.64). Assuming the reservoir rate equation is in the stationary condition, we have $\partial_t n_X(t, \boldsymbol{r}_\parallel) = 0$ from Eq. (2.64), so that we can simplify the 2D GPE in linear regime:

$$i\hbar\frac{\partial}{\partial t}\Psi(t,\boldsymbol{r}_\parallel) = \Big\{ -\frac{\hbar^2}{2m^*}\nabla_\parallel^2 + \frac{G}{\Gamma_X}(1+\eta)P(\boldsymbol{r}_\parallel) + i\frac{\hbar}{2}\Big[\frac{R}{\Gamma_X}P(\boldsymbol{r}_\parallel) - \gamma\Big]\Big\}\Psi(t,\boldsymbol{r}_\parallel). \quad (2.67)$$

The nonresonant pumping directly contributes to the real and complex potential, as shown in Eq. (2.67) when the system is just above the threshold. Equation (2.67) also indicates that the blue shift from the nonresonant pump also shares similar patterns in the pump profile, which makes it possible to tailor the potential landscape by engineering the laser at the beginning. In chapters 4 and 5, the anisotropic pump shapes are studied despite using the nonlinear form from Eqs. (2.63) and (2.64), based on Eq. (2.67), we can conclude that the anisotropic shapes originating from the pump preserve a similar pattern from the reservoir to the condensates. The GPE in linear regime from Eq. (2.67) can also be further simplified by adding the real and imaginary potential and a driven resonant electric field directly:

$$i\hbar\frac{\partial}{\partial t}\Psi(t,\boldsymbol{r}_\parallel) = \Big[-\frac{\hbar^2}{2m^*}\nabla_\parallel^2 + (V_r + iV_i)f(\boldsymbol{r}_\parallel) - i\frac{\hbar}{2}\gamma\Big]\Psi(t,\boldsymbol{r}_\parallel) + E(\boldsymbol{r}_\parallel)e^{-i\omega_s t}, \quad (2.68)$$

where $f(\boldsymbol{r}_\parallel)$ is the 2D spatial profile of the potential, V_r and V_i quantify the real and imaginary parts of the potential, and $E(\boldsymbol{r}_\parallel)$ is a resonant driving field with frequency ω_s. One can see that with steady-state solutions $\Psi(t,\boldsymbol{r}_\parallel) = \psi(\boldsymbol{r}_\parallel)e^{-i\omega_s t}$, Eq. (2.68) can be transformed into a nonhomogeneous Helmholtz equation. From Eq. (2.68), it is more intuitive to build the connections between the polariton flow and the hydrodynamics. Of course, the potential terms V_r and V_i should be nonlinear in the realistic model of Eq. (2.63) joined with the reservoir rate equation of Eq. (2.64). More discussions of Eq. (2.68) can be found in chapter 4.

2.3.3.2 Stochastic projection

The GPE, as referenced in Eq. 2.63, is derived based on the assumptions of mean-field theory where the interactions between polaritons are treated as averaged and constant for each particle. This approach neglects fluctuations arising from the quantum field of the polaritons, and, as a result, its capacity to capture the intricate details of particle correlations within the system is limited.

To address this issue inherent to mean-field theory, researchers have introduced the Stochastic Gross-Pitaevskii Equation (SGPE). The SGPE, a Langevin type equation, is derived from the GPE under the truncated Wigner approximation [42]. Unlike the GPE, the SGPE incorporates random fluctuations, thereby more accurately representing the quantum nature of polaritons and their interactions. The quantum fluctuations and correlations, neglected in the standard GPE, are reintroduced in this stochastic version. In this way, the SGPE provides a more complete picture of the dynamics of a quantum system, allowing for a more nuanced understanding of polariton interactions. The SGPE is given by

$$\begin{aligned} i\hbar\frac{\partial}{\partial t}\Psi(t,\boldsymbol{r}_{\parallel}) &= \Big\{-\frac{\hbar^2}{2m^*}\nabla_{\parallel}^2+\alpha|\Psi(t,\boldsymbol{r}_{\parallel})|^2+G\Big[n_X(t,\boldsymbol{r}_{\parallel})+\frac{\eta}{\Gamma_X}P(\boldsymbol{r}_{\parallel})\Big] \\ &\quad +i\frac{\hbar}{2}\big[Rn_X(t,\boldsymbol{r}_{\parallel})-\gamma\big]\Big\}\Psi(t,\boldsymbol{r}_{\parallel})+i\hbar\frac{dW}{dt}. \end{aligned} \tag{2.69}$$

The last term on the RHS of Eq. (2.69) stands for a complex white noise operator. The white noise satisfies,

$$\langle dW_i dW_j\rangle = 0, \tag{2.70}$$

$$\langle dW_i^* dW_j\rangle = \frac{\gamma+Rn_X}{2\Delta A}dt\delta_{i,j}. \tag{2.71}$$

Here, i and j refer to different spatial grid points (see chapter 3), and ΔA is the area of each grid cell. From Eq. (2.69), we can see that the noise operator directly adds the perturbation to the condensate phase and amplitude at each time step and in every spatial grid. The stochastic projection is used in chapter 5 in order to measure how fast a system can recover from the perturbation produced by the noise operator, and the method for the measurement is introduced in section 2.3.3.3.

It is worth addressing that the truncated Wigner approximation we used here from Ref. [42] is valid if the inequality

$$\gamma \gg \frac{g}{\Delta A} \tag{2.72}$$

is satisfied. Using the parameters from chapter 5, we obtain $\gamma\Delta A/g \approx 29.9 \gg 1$.

2.3.3.3 First-order spatial coherence

The equal-time spatial coherence between two regions of 2D complex map $\Psi(t, \boldsymbol{r}_\parallel)$ can be given by the normalized complex first-order coherence function, which is usually denoted as $g^{(1)}$, is given by

$$\mu_{\mathcal{LM}} = \frac{\langle \psi_{\mathcal{L}}{}^* \cdot \psi_{\mathcal{M}} \rangle}{\sqrt{\langle \psi_{\mathcal{L}}{}^* \cdot \psi_{\mathcal{L}} \rangle \cdot \langle \psi_{\mathcal{M}}{}^* \cdot \psi_{\mathcal{M}} \rangle}}, \tag{2.73}$$

where $\psi_{\mathcal{L}}$ and $\psi_{\mathcal{M}}$ is two subset of $\Psi(t, \boldsymbol{r}_\parallel)$ with spatial region $\mathcal{L}$ and $\mathcal{M}$ (see Fig. 2.9), respectively. Note that the dimensions of $\mathcal{L}$ and $\mathcal{M}$ cropped from the entire spatial grid are the same.

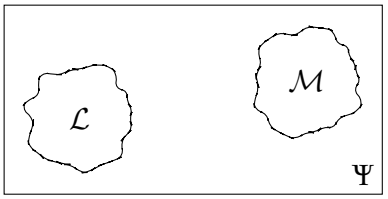

FIGURE 2.9: Sketch of two regions denoted $\mathcal{L}$ and $\mathcal{M}$ from 2D wavefunction Ψ.

The time average operator $\langle \dots \rangle$ from Eq. (2.73) is defined as

$$\langle \psi_{\mathcal{L}}{}^* \cdot \psi_{\mathcal{M}} \rangle = \left(T_{\text{coh}} \int_{\text{Cropped}} d\boldsymbol{r}_\parallel \right)^{-1} \int_{T_{\text{coh}}} \int_{\text{Cropped}} \psi_{\mathcal{L}}{}^*(\boldsymbol{r}_\parallel, t) \cdot \psi_{\mathcal{M}}(\boldsymbol{r}_\parallel, t) d\boldsymbol{r}_\parallel dt, \tag{2.74}$$

where T_{coh} is the time duration of time-averaged coherence and $\int_{\text{Cropped}} d\boldsymbol{r}_\parallel$ is the cropped area of $\mathcal{L}$ and $\mathcal{M}$. The modulus of the first-order coherence function satisfies the relation $|\mu_{\mathcal{LM}}| \leqslant 1$, and its argument whereas its argument represents their average phase difference

$$\theta_{\mathcal{LM}} = \arg(\mu_{\mathcal{LM}}) \tag{2.75}$$

represents their average phase difference. In chapters 3, a parallel computing algorithm of calculating Eq. 2.73 is introduced, and the mutual coherence between different pairs of $\mathcal{L}$ and $\mathcal{M}$ of the condensate in the polariton lattices is applied in chapter 5. Note that in the absence of the perturbation from the white noise (see section 2.3.3.2), when the system is in the stationary state, any arbitrary regions $\mathcal{L}$ and $\mathcal{M}$ are perfectly correlated (reaching unity for $|\mu_{\mathcal{LM}}|$). In the presence of the perturbation, $|\mu_{\mathcal{LM}}|$ is expected to decrease.

2.4 Conclusions

This chapter introduces the polariton system from a theoretical perspective in the second quantization formalism. From pure photonic mode to pure excitonic mode, the

photonic and excitonic dispersion relations share a similar parabola-like form near the band edge, shown in Figs. 2.2 and 2.5. The geometric condition also applies to the effective mass of both photonic and excitonic modes. The microcavity photons are produced from the confinement of mirrors, and the effective mass can be tuned by the cavity directly (see section 2.2.1); meanwhile, the excitonic effective mass is also largely affected by the confinement from the quasi-2D quantum well (see section 2.2.2). The polaritons of part photonic components and part excitonic components introduced in section 2.2.3 are formed under the SC regime. The Hopfield coefficients, which characterize the ratio of photonic and excitonic components, are core parameters because they can tune the effective mass of the polariton. Cryogenic temperatures (around $10K$) are required for inorganic materials due to the effective mass of light that originates mainly from the photonic branch of the polariton. Once the condensates occur when the pump power density is above the threshold, the excitonic branch plays a main role in the repulsive polariton-polariton interaction. In addition, such a nonlinear interaction of the GPE (see section 2.3.3) can lead to a blueshift outside the pumping region, which is the main argument for chapter 4, making it promising to have all-optical polariton devices.

The interface between the phase transition occurs when the system is just above the threshold. To study the condensates near the threshold, the linear regime, where the condensates are weak enough to neglect the nonlinear terms in both the main GPE and reservoir rate equations, is usually applied (see section 2.3.3.1) for theoretical studies. By employing the stochastic projection to the RHS of the general GPE, to what degree the system responds to the white Gaussian noise is known by measuring the time-integrated spatial mutual coherence function. In chapter 5, the stochastic methods introduced in sections 2.3.3.2 and 2.3.3.3 are used, to make a comparison with triangular- or circular-tailored spots in the polariton lattice. Until now, only half of the introduction has been completed, and the rest concerning the numerical algorithm and the computational language with parallel computing are addressed in the chapter 3.

Chapter 3

Introduction to numerical methods with graphics processing unit

3.1 Introduction

This chapter introduces numerical methods for simulating polariton condensates, along with the associated, custom-built computational tool primarily based on the graphics processing unit (GPU). As presented in section 2.3.3, the main GPE describing the polariton condensates is a partial differential equation of first order in time and second order in space. The split-step Fourier method (SSFM) [43] is particularly chosen for all numerical simulations treated in this thesis to make the equation easy to solve in the framework of a parallel computing system. Moreover, utilizing the concept of SSFM in machine learning offers a novel approach, known as Fourier neural oeprator, to tackling partial differential equations in a more efficient way [44]. Researchers have explored the use of a CPU-based GPE solver [45–48]. Besides, the GPU and SSFM based solver has been investigated [49] and can be applied for finding the solution of the GPE [50–52]. One advantage of employing SSFM is the ability to convert the spatial second derivative into a linear problem using the fast Fourier transform (FFT). In particular, the computation tool for the application of SSFM is based on the NVIDIA Compute Unified Device Architecture (CUDA)[1] and is written in C++ utilizing mainly the CUDA Runtime Application Programming Interface (API) and partially the Driver API [53].

This chapter is arranged as follows: In section 3.2, I will briefly introduce SSFM with the example of the GPE from Eq. (2.63). Section 3.3 introduces the basic principles of CUDA from both hardware and software perspectives. In section 3.4, combining the

[1] Although different APIs of parallel computing architectures are available, for example, the Open Computing Language (OpenCL), different from CUDA in terms of the grammar or exclusive features, the general idea and algorithm behind the architecture may be similar.

SSFM and CUDA introduced in the first two sections, the algorithm of the GPE solver is shown. In addition, CUDA reduction methods for the summation of the total number of particles, used to estimate the threshold power of the system, and the first-order correlation factors of two quantities, mentioned in section 2.3.3.3, are also introduced.

3.2 Split-step Fourier method

The SSFM, a method to seek the numerical solution of the time-dependent linear or nonlinear Schrödinger equation widely used in quantum mechanics or optics, deals with higher-order time and spatial derivatives. The essence of SSFM is the divide-and-conquer algorithm. The time and spatial domains are sliced into infinitesimal time steps and small grids to reduce computational complexity. In this thesis, the first order in time and second order in space, as in Eq. (2.63), are taken into account.

Let us first consider the time domain and assume that the total length of time can be divided into multiple infinitesimal steps of equal spacing in which each step is denoted as Δt. Thus, only the spatial domain is considered for each infinitesimal time interval $[t, t + \Delta t]$. The second-order derivative in space is not trivial to solve directly; however, with the help of the Fourier transform (FT), the second-order derivative in real space can be reduced into a linear problem in Fourier space. Then, the inverse Fourier transform (IFT) is applied after operations in Fourier space to put the quantity back in the real space. Despite the fact that the second-order derivative can be omitted, there is a clear disadvantage that iteration over significant pairs of FT and IFT can also lead to significant consumption of computing resources.

However, the boost of the FFT algorithm and the inverse FFT (IFFT) greatly reduces the time complexity from $\mathcal{O}(N^2)$ to $\mathcal{O}(N \log N)$ where N stands for the size of the data [54]. For computational software, `FFTW`, a widely used open source FFT library, has been architected to run on CPUs [55]; however, this is still computationally expensive, in the case of a large spatial computational grid and the need to compute large datasets in parallel. The GPU-intensive library called `cuFFT` from NVIDIA Toolkit [53] brings parallelism to FFT, enabling the efficiency of SSFM involving massive iterations of FFT and IFFT operations. In this thesis, the numerical results dealing with large polariton lattices are shown in chapter 5 benefit significantly from `cuFFT` library.

Let us focus on the general concept of SSFM as an example of solving the two-dimensional GPE from Eq. (2.63). The Hamiltonian from the GPE can be rearranged into two parts:

$$\frac{\partial}{\partial t}\Psi(t, \boldsymbol{r}_{\parallel}) = \left(\widehat{\mathcal{L}} + \widehat{\mathcal{N}}\right)\Psi(t, \boldsymbol{r}_{\parallel}), \tag{3.1}$$

where

$$\widehat{\mathcal{L}} = i\frac{\hbar}{2m^*}\nabla_{\parallel}^2, \tag{3.2}$$

$$\widehat{\mathcal{N}} = -i\frac{\alpha}{\hbar}|\Psi(t,\boldsymbol{r}_{\parallel})|^2 - i\frac{G}{\hbar}\Big[n_X(t,\boldsymbol{r}_{\parallel}) + \frac{\eta}{\Gamma_X}P(\boldsymbol{r}_{\parallel})\Big] + \frac{1}{2}\big[Rn_X(t,\boldsymbol{r}_{\parallel}) - \gamma\big]. \tag{3.3}$$

$\widehat{\mathcal{L}}$ and $\widehat{\mathcal{N}}$ are linear and nonlinear operators, respectively. A direct solution of Eq. 3.1 gives

$$\Psi(t+\Delta t,\boldsymbol{r}_{\parallel}) = e^{\left(\widehat{\mathcal{L}}+\widehat{\mathcal{N}}\right)\Delta t}\Psi(t,\boldsymbol{r}_{\parallel}). \tag{3.4}$$

Since both operators do not commute, namely $[\hat{\mathcal{L}},\hat{\mathcal{N}}] \neq 0$, we have $e^{\widehat{\mathcal{L}}+\widehat{\mathcal{N}}} \neq e^{\widehat{\mathcal{L}}}e^{\widehat{\mathcal{N}}}$. However, through the Baker–Campbell–Hausdorff (BCH) formula at second-order

$$\ln\left(e^{\widehat{\mathcal{L}}\Delta t}e^{\widehat{\mathcal{N}}\Delta t}\right) \approx \widehat{\mathcal{L}}\Delta t + \widehat{\mathcal{N}}\Delta t + \frac{1}{2}[\widehat{\mathcal{L}},\widehat{\mathcal{N}}]\Delta t, \tag{3.5}$$

we can further split the exponential term. To get better accuracy, as a result of the strang splitting, Eq. (3.5) is rearranged to

$$\ln\left(e^{\frac{1}{2}\widehat{\mathcal{N}}\Delta t}e^{\widehat{\mathcal{L}}\Delta t}e^{\frac{1}{2}\widehat{\mathcal{N}}\Delta t}\right) \approx \widehat{\mathcal{L}}\Delta t + \widehat{\mathcal{N}}\Delta t + \frac{1}{16}[[\widehat{\mathcal{N}},\widehat{\mathcal{L}}],\widehat{\mathcal{N}}]\Delta t^3, \tag{3.6}$$

which is obtained by applying the BCH twice. The comparison of Eqs. (3.5) and (3.6) shows that the latter gives higher accuracy at the third order of the time step. Thus, by substituting Eq. (3.6) into Eq. (3.4), we obtain

$$\Psi(t+\Delta t,\boldsymbol{r}_{\parallel}) = e^{\frac{1}{2}\widehat{\mathcal{N}}\Delta t}e^{\widehat{\mathcal{L}}\Delta t}e^{\frac{1}{2}\widehat{\mathcal{N}}\Delta t}\Psi(t,\boldsymbol{r}_{\parallel}). \tag{3.7}$$

Although Eq. (3.7) gives a clean solution at the time interval $[t, t+\Delta t]$ with third-order approximation, there remains a question to be answered if the operation sequence should be taken into account for the nonlinear term $|\Psi(t,\boldsymbol{r}_{\parallel})|^2$ that is appearing twice in both nonlinear operators $\widehat{\mathcal{N}}$ defined from Eq. (3.7)? The answer is that it is crucial that Ψ also follows the squence to maintain precision to a certain degree. Javanainen and Ruostekoski have concluded that as long as each Ψ of operators $\widehat{\mathcal{N}}$ and $\widehat{\mathcal{L}}$ in Eq. (3.7) is updated to the latest value, the third-order approximation is still valid, which is also applied to the case when we exchange both operators $\widehat{\mathcal{N}}$ and $\widehat{\mathcal{L}}$ in Eq. (3.7) [56]. To be clear, the procedure for the evolution of the wavefunction at the time interval $[t, t+\Delta t]$ is shown in the following

$$\begin{array}{ccc}
\Psi(t,\boldsymbol{r}_{\parallel}) \xrightarrow{\Psi:=\Psi+\varepsilon} e^{\frac{1}{2}\widehat{\mathcal{N}}\left[|\Psi(t,\boldsymbol{r}_{\parallel})|^2\right]\Delta t}\Psi(t,\boldsymbol{r}_{\parallel}) & \xrightarrow{\Psi_1(t,\boldsymbol{r}_{\parallel})} & e^{\widehat{\mathcal{L}}\Delta t}\Psi_1(t,\boldsymbol{r}_{\parallel}) \\
 & & \Big\downarrow \Psi_2(t,\boldsymbol{r}_{\parallel}) \\
\Psi(t+\Delta t,\boldsymbol{r}_{\parallel}) & \longleftarrow & e^{\frac{1}{2}\widehat{\mathcal{N}}\left[|\Psi_2(t,\boldsymbol{r}_{\parallel})|^2\right]\Delta t}\Psi_2(t,\boldsymbol{r}_{\parallel})
\end{array} \tag{3.8}$$

Here, ε is the random noise defined in Eq. (2.66). It can be seen that in (3.8) at each step with nonlinear operator $\widehat{\mathcal{N}}[|\Psi|^2]$ the nonlinear term $|\Psi|^2$ comes out of the previous step and is updated to its latest value.

Let us focus on the nonlinear operation $e^{\widehat{\mathcal{L}}\Delta t}\Psi_1(t, \boldsymbol{r}_\parallel)$ where the FT from the real space to the momentum space takes place. The Schrödinger involving the linear operator $\widehat{\mathcal{L}}$ and wavefunction $\Psi_1(t, \boldsymbol{r}_\parallel)$ can be expressed as

$$\frac{\partial}{\partial t}\Psi_1(t, \boldsymbol{r}_\parallel) = \widehat{\mathcal{L}}\Psi_1(t, \boldsymbol{r}_\parallel). \tag{3.9}$$

Taking the FT of both sides of the Eq. (3.9), we arrive at the relationship

$$\frac{\partial}{\partial t}\mathcal{F}[\Psi_1(t, \boldsymbol{r}_\parallel)] = \mathcal{F}[\widehat{\mathcal{L}}\Psi_1(t, \boldsymbol{r}_\parallel)] = \widehat{\mathcal{P}}\mathcal{F}[\Psi_1(t, \boldsymbol{r}_\parallel)], \tag{3.10}$$

where $\mathcal{F}[\dots]$ stands for the operation of the FT and the momentum operator is

$$\widehat{\mathcal{P}} = -i\frac{\hbar}{2m^*}\boldsymbol{k}_\parallel^2. \tag{3.11}$$

Thus, by replacing the linear operator $\widehat{\mathcal{L}}$ with the momentum operator $\widehat{\mathcal{P}}$, the second-order spatial derivative is dropped. To be able to replace the operator in Eq. (3.10), the wavefunction should first be Fourier transformed to the Fourier space, then multiply the exponential term containing the momentum operator, and finally Ψ_2 is obtained through the inverse Fourier transform. Thus, the procedure (3.8) at time interval $[t, t + \Delta t]$ becomes

$$\begin{array}{ccccc} \Psi(t, \boldsymbol{r}_\parallel) & \xrightarrow{\Psi:=\Psi+\varepsilon} & e^{\frac{1}{2}\widehat{\mathcal{N}}\left[|\Psi(t,\boldsymbol{r}_\parallel)|^2\right]\Delta t}\Psi(t, \boldsymbol{r}_\parallel) & \xrightarrow{\Psi_1(t,\boldsymbol{r}_\parallel)} & e^{\widehat{\mathcal{P}}\Delta t}\mathcal{F}\left[\Psi_1(t, \boldsymbol{r}_\parallel)\right] \\ & & & & \Big\downarrow{\scriptstyle \Psi_2(t,\boldsymbol{k}_\parallel)} \\ \Psi(t + \Delta t, \boldsymbol{r}_\parallel) & \longleftarrow & e^{\frac{1}{2}\widehat{\mathcal{N}}\left[|\Psi_2(t,\boldsymbol{r}_\parallel)|^2\right]\Delta t}\Psi_2(t, \boldsymbol{r}_\parallel) & \xleftarrow[\Psi_2(t,\boldsymbol{r}_\parallel)]{} & \mathcal{F}^{-1}\left[\Psi_2(t, \boldsymbol{k}_\parallel)\right] \end{array} \tag{3.12}$$

In procedure (3.12), $\mathcal{F}^{-1}[\dots]$ stands for the operation of the IFT. To complete the calculation, the $\Psi(t + \Delta t, \boldsymbol{r}_\parallel)$ obtained at the end of the procedure (3.12) is transferred to $\Psi(t, \boldsymbol{r}_\parallel)$ multiple times until the system reaches the final time. The procedure (3.12) is the core part of the SSFM, and a CUDA-enabled library `cuFFT`, is used to accelerate FFT and IFFT, and is introduced in subsequent sections.

3.3 Parallel computing with CUDA

Unlike the conventional CPU-based architecture, where CPU cores are much more limited, GPU has many more cores, even in consumer products. A comparison of CPU and GPU architecture is illustrated in Fig. 3.1. The terminologies "core" for both CPU and

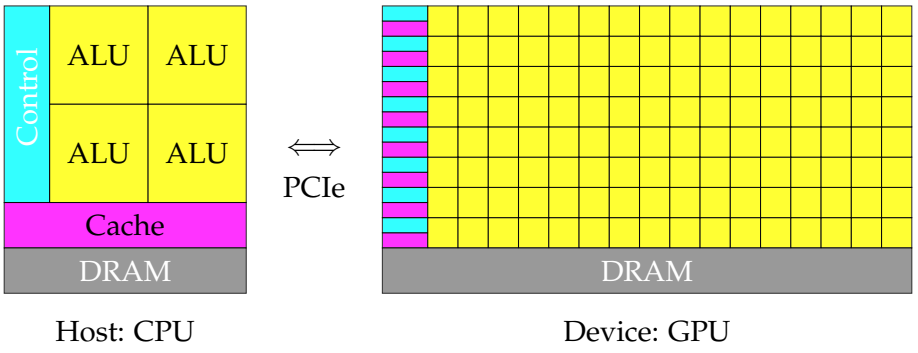

FIGURE 3.1: The comparison and the communication between the CPU and GPU architecture. (Figure is adapted from *CUDA C++ Programming Guide* from NVIDIA [57])

GPU mentioned earlier, though, have different implications. For instance, dual physical cores in an INTEL CPU can have up to four virtual threads, known as hyperthreading, and each physical core consists of an arithmetic logic unit (ALU), a logic control unit, and caches, while the NVIDIA CUDA core usually refers to a large number of execution units following the concept of "Single Instruction, Multiple Data" (SIMD) [57].[2] Thanks to the SIMD feature, CUDA is used for the first time for deep convolutional neural networks, known as AlexNet, in image identification in 2012 [58].

Generally speaking, each thread of a CPU comes with an execution of a task at a fast speed, but is limited by the number of threads running concurrently; however, there are thousands of threads running in parallel in GPU but with a slower execution speed per thread. There are always advantages and disadvantages when choosing the preferable architecture for executing certain tasks. Figure 3.1 depicts the main difference between a CPU and a GPU in that unlike a CPU where each core has its control unit and can access the CPU's fast memory (cache), in a GPU, cores are organized into groups, with each group controlled by a single control unit and sharing access to a cache. Both the CPU and the GPU are connected to dynamic random-access memory (DRAM); the CPU directly accesses the system's DRAM, while the Nvidia GPU, designed for CUDA, operates using its dedicated memory, often referred to as GPU global memory[3], a specific variant of DRAM, to handle its computations.

Before attempting to go into detail, keep in mind that parallel computing is not confined to a particular type of hardware, such as a GPU. Instead, it is a concept that applies to any hardware capable of concurrent operations, including multicore CPUs, which can also perform parallel processing up to a certain extent. In other words, parallel programming is fundamentally about algorithm design rather than the specifics of the underlying hardware. For instance, in a parallel computing network, various units can

[2]The NVIDIA CUDA core usually means an execution unit that can perform a single-precision floating-point (FP32) operation per clock cycle, and there is no direct comparison of threads and cores between CPU and GPU.

[3]It is worthy noting that the memory configurations differ for different hardware archetectures. For example, the unified memory that the CPU and GPU can access is part of the Apple M1 series chips.

be interconnected, and each unit can comprise different elements, such as CPUs, GPUs, Field Programmable Gate Arrays (FPGAs), or other computational units.

3.3.1 Host and device

To have parallel computing that fulfills the potential of such a complex system, the challenging part is how the task is divided into multiple parts that are conquered by different hardware and how these components efficiently communicate with each other. Usually, the terminology "heterogeneous computing" is used when different computing units are involved. This chapter uses a heterogeneous computing system consisting of only an INTEL x86-64 CPU and a single NVIDIA GPU with a compute capability of 8.6. The CPU and GPU are connected through Peripheral Component Interconnect Express (PCIe) (see Fig. 3.1), which is limited by the bandwidth between the CPU and GPU. Before applying SSFM with the power of the GPU, basic concepts of the GPU architecture and CUDA API should be introduced first. In this section, only the details related to the integration of SSFM and CUDA are covered. For anyone looking for a complete guide to CUDA, the official document *CUDA C++ Programming Guide* from NVIDIA [57] is recommended.

To complete the story, as depicted in Fig. 3.1, we will introduce the terms "host" and "device" in section 3.3.3. In the context of the system examined in this thesis, these terminologies, frequently used in software discussions, denote that functions are typically launched in the CPU (host) and executed in the GPU (device).

3.3.2 Thread and memory hierarchy

In the hardware hierarchy, a GPU is composed of several parts known as streaming multiprocessors. These multiprocessors are where threads run concurrently, if they belong to the same multiprocessor. The GPU's structure can be explained from both physical and logical standpoints, which in turn, determine the number of threads that can be practically employed.

Let us first consider the physical perspective. In the context of a GPU with compute capability 8.6, a set of 32 threads is referred to as a 'warp'. Threads within a warp are scheduled sequentially, starting from 0 through 31. The maximum number of warps each multiprocessor can host is 48. As such, the total number of resident threads per multiprocessor is calculated by multiplying the number of threads in a warp (32) by the maximum number of warps per multiprocessor (48), resulting in 1536 resident threads.

From a logical viewpoint, each multiprocessor can be partitioned into several 'thread blocks', with each block containing up to 1024 threads. In this role, the multiprocessor orchestrates the scheduling of thread blocks and the number of threads within each

block. For the GPU with a compute capability of 8.6, a maximum of 16 resident thread blocks can be scheduled within each multiprocessor. If we disregard the physical limitations, theoretically, the total number of threads per multiprocessor can be as high as 1024 multiplied by 16, which equals 16384. However, in practice, due to physical constraints, this figure cannot exceed 1536 resident threads per multiprocessor.

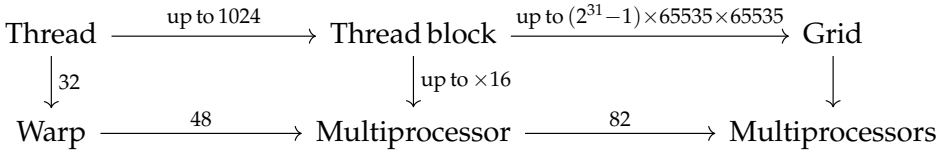

FIGURE 3.2: A simplified thread structure of a GPU from both physical and logical perspectives. The information is based on compute capability 8.6 with 82 multiprocessors.

One crucial point to note is that once a warp is invoked, even if not all threads within it are being actively executed, the remaining idle threads[4] are still considered unavailable for other instructions. Thus, one of the strategies for choosing the number of threads per thread block is to have an integer multiple of the number of threads per warp, namely 32. Furthermore, once the data size is fixed, distributing a proper number of threads and thread blocks is very important to use the GPU resources fully. Figure 3.2 illustrates the relations between the thread blocks structure from the programming's perspective and the warp-multiprocessors from the physical perspective.

Up to now, only the thread-related feature is shown and the details of the memory feature[5] that also plays a core rule can be found in the official document [57]. This section aims to deliver two messages: the first is that in CUDA, data are processed with a group of CUDA threads, and the second is that the performance of the computation highly depends on the optimization of the initiation of the threads. For the following discussion, we will pay more attention to the programming side and limit ourselves to the case of using a single multiprocessor.

3.3.3 Kernel and launch parameters

In practical CUDA coding, the address of a single thread is obtained through keyword `threadIdx`, `blockIdx`, and `blockDim`, which return, respectively, the thread address of its current thread block, the block address of the grid, and the dimension of the grid. These keywords, indicating the address of each thread, can return vector up to three

[4]The idle threads stand for these threads that are inactive and waiting for computations.

[5]For example, all the threads in the same thread block can have access to the "shared memory" with limited size. Thus, the size of the shared memory also becomes a bottleneck with respect to the dimension of each thread block. The shared memory is much faster than the GPU global memory, so it is ideal for some applications requiring certain data to be repeatedly used for certain operations. The operation of image blurring calculated through the convolution of the original image and the mask is a good example of using shared memory, since the mask can be stored in shared memory.

directions of x, y and z. To give an example of the allocation of the thread from these parameters defined in the Device API [53], given the number of threads and dimension of the threads blocks, the global unique address of all the threads printed in the sequence is shown as

$$\texttt{Id} = \texttt{threadIdx.x} + \texttt{blockIdx.x} * \texttt{blockDim.x}, \tag{3.13}$$

where `Id` refers to a specific thread address, and only the x-direction of the input parameters are considered. Alternatively, Eq. (3.13) can also be expressed in 2D:

$$\texttt{Id\_x} = \texttt{threadIdx.x} + \texttt{blockIdx.x} * \texttt{blockDim.x}, \tag{3.14}$$

$$\texttt{Id\_y} = \texttt{threadIdx.y} + \texttt{blockIdx.y} * \texttt{blockDim.y}, \tag{3.15}$$

$$\texttt{Id} = \texttt{Id\_x} + \texttt{stride\_x} * \texttt{Id\_y}, \tag{3.16}$$

where `stride_x` can be the length along one direction of a 2D vector. The thread address is not limited by the expression mentioned above; this also reminds us of the logical side of thread blocks and the flexibility based on the physical structure. Figures 3.3 sketches the 2D thread blocks structure with an example of taking `blockDim=(3,3)` and `gridDim=(3,3)`.

The self-defined function in CUDA is called the "kernel", which provides the instruction of threads assigned from the launch parameters. The launch parameters that determine the structure of thread blocks are called from syntax `<<< ... >>>`. For example, we show below the addition of two arrays stored in the GPU global memory `A` and `B` with length `N`, then transferring the result to `C`. Such the kernel is defined by

```
// Self-defined kernel executed from the device.
__global__ void vector_addition(int N, double* A, double* B, double* C)
{
    for (int Id = threadIdx.x + blockIdx.x * blockDim.x;
        Id < N; Id += blockDim.x * gridDim.x)
    {
        C[Id] = A[Id] + B[Id];
    }
}
```

The iteration goes through all the elements from `A` and `B`; meanwhile, at each iteration, the addition operation is applied while passing the results to `C` at the same thread address of `Id` as the `A` and `B`. The declaration `__global__` guarantees that the function can be called in both the host (CPU) and device (GPU). Condition `Id<N` ensures that each element of `A` and `B` is extracted. What if the input data size is larger than the maximum number of threads that we set on all the thread blocks? Here, the grid-stride

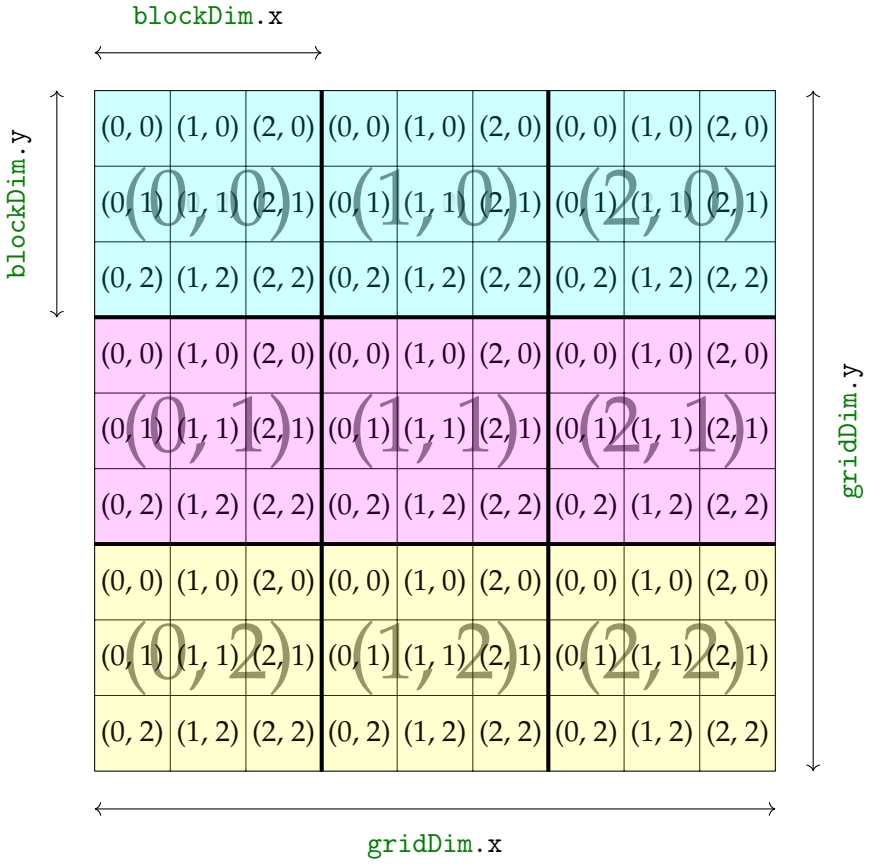

FIGURE 3.3: Illustration of the thread blocks structure in 2D. Each small block refers to a specific 2D thread address, and each large block means a specific 2D thread block address. `blockDim.x * blockDim.y` is the number of threads per thread block and `gridDim.x * gridDim.y` gives the total number of thread blocks.

`blockDim.x * gridDim.x` works like every time we run out of all the threads in grid, the iteration starts again with the step of the total number of threads per grid [59]. The kernel of this addition operation is launched on the host with launch parameters defined at run time. And the example of launching the kernel function in host is given by

```
// Call the kernel with launch parameters from the host.
int main()
{
    ...
    vector_addition<<<dimBlock, dimThreadBlocks>>>(N, A, B, C);
    ...
}
```

Here, the launch parameters are `dimBlock` and `dimThreadBlocks`. A complete vector addition example can be found in *CUDA C++ Programming Guide* from NVIDIA [57]. This kernel can also be understood in this way: It is an instruction sent to each thread

attached with its ID inside a set of threads `<<<dimBlock, dimThreadBlocks>>>` and thousands of threads are receiving an instruction, which is the kernel, and the bulit-in varibales `threadIdx.x` and `blockIdx.x` help each thread find its unique position inside the GPU. The goal of parallel computing is to fully utilize GPU resources. To make sure that all the blocks are filled, one practical choice of the launch parameters can be given by

$$\texttt{dimThreadBlocks} = \text{floor}\left(\frac{\texttt{N + dimBlock - 1}}{\texttt{dimBlock}}\right). \tag{3.17}$$

Given a 256×256 matrix with data size $N = 65536$ and $\texttt{dimBlock} = 512$, using Eq. 3.17, we arrive at $\texttt{dimThreadBlocks} = 128$.

3.4 Gross-Pitaevskii equation solver

In this section, we will show an application attached with pseudocode code to solve the GPE with SSFM and CUDA introduced in sections 3.2 and 3.3. Recall the procedure (3.12)

$$\cdots \Psi \xrightarrow{\Psi:=\Psi+\varepsilon} e^{\frac{1}{2}\widehat{\mathcal{N}}\left[|\Psi|^2\right]\Delta t}\Psi \xrightarrow{\Psi_1} e^{\widehat{\mathcal{P}}\Delta t}\mathcal{F}\left[\Psi_1\right] \xrightarrow{\Psi_2^k} \mathcal{F}^{-1}\left[\Psi_2^k\right] \xrightarrow{\Psi_2} e^{\frac{1}{2}\widehat{\mathcal{N}}\left[|\Psi_2|^2\right]\Delta t}\Psi_2 \longrightarrow \Psi \cdots \tag{3.18}$$

in which the first and the last Ψ refer to the input wavefunction and output wavefunction at time interval $[t, t + \Delta t]$, respectively.

3.4.1 Application to split-step Fourier transform

Algoithm 1 illustrates the overview of the GPE solver. Although the coupled reservoir rate equation from Eq. (2.64) and the stochastic projection from section 2.3.3.2 and chapter 5 are very important, here we limit ourselves to a simplified case by considering only the main GPE from Eq. 2.63. The calculation of the mutual spatial coherence function from section 2.3.3.3 is still taken into account to demonstrate the algorithm in the absence of the stochastic term.

All input matrices, as well as relevant parameters, are described in **Input** of Algoithm 1. It is worth mentioning that the 2D computational grid used here is initialized in a concatenated row-major order array. We want to use the concatenated array because it is much simpler for pointwise operations; for example, the matrix addition of 2D arrays introduced in section 3.3.3 can be executed through the non-nested loop. However, using the concatenated array does not imply the loss of dimensional information. Typically, once the spatial grid is determined, the dimensions of the columns or rows of

Algorithm 1: Gross-Pitaevskii Equation Solver

Input: D: Matrix row and column dimensions
d: Cropped matrix row and column dimensions
Δt: Time step size
Δx, Δy: Grid cell dimensions along the x and y axes
T: Total simulation time (where ceil$[T/\Delta t] = T/\Delta t$ holds)
T_{ave}: Time-integrated intensity duration
T_μ: Time-integrated spatial coherence duration
N_n: Node count in the polariton lattice
$\{\sum_{i=0}^{D-1}\sum_{j=0}^{D-1}\Psi(x_i, y_j)\}$: Wavefunction (complex-valued matrix)
$\{\sum_{i=0}^{D-1}\sum_{j=0}^{D-1}\mathcal{P}(k_i, k_j)\}$: Momentum operator (complex-valued matrix)
$\{\sum_{i=0}^{D-1}\sum_{j=0}^{D-1}\mathcal{N}(x_i, y_j)\}$: Nonlinear operator (complex-valued matrix)
$\{\sum_{i=0}^{D-1}\sum_{j=0}^{D-1} I(x_i, y_j)\}$: Time-integrated intensity (real-valued matrix)
$\{\sum_{t_n=0}^{T/\Delta t+1} N(t_n)\}$: Particle count (real-valued matrix)
$\{\sum_{l=0}^{N_n-1}\mu(l)\}$: Mutual spatial coherence (complex-valued matrix)
`dimBlock`: Thread count per block
`dimThreadBlocks`: Thread block count per grid

Output:
Final time Ψ
Updated I, N, μ

Initialize: Transfer data from host to device:
$\Psi_{\text{dev}} \leftarrow \Psi$, $\mathcal{P}_{\text{dev}} \leftarrow \mathcal{P}$, $\mathcal{N}_{\text{dev}} \leftarrow \mathcal{N}$, $I_{\text{dev}} \leftarrow I$, $N_{\text{dev}} \leftarrow N$, $\mu_{\text{dev}} \leftarrow \mu$
Initialize I_{dev}, Ψ_{dev}, and μ_{dev} to zero

for $t_n = 0, 1, \ldots, T/\Delta t$ **do**
  Inject background noise into Ψ_{dev}: $\Psi_{\text{dev}} \leftarrow \Psi_{\text{dev}} + \varepsilon$
  Execute Sum-Kernel<<<`dimBlock, dimThreadBlocks`>>>(N_{dev}, Ψ_{dev}, D)
  Perform SSFM-CELL(Ψ_{dev}, $\mathcal{P}_{\text{dev}}$, $\mathcal{N}_{\text{dev}}$, D, Δt, `dimBlock`, `dimThreadBlocks`)
  if $t_n\Delta t > T - T_{\text{ave}}$ **then**
    Execute TI-Intensity-Kernel<<<`dimBlock, dimThreadBlocks`>>>(I_{dev}, Ψ_{dev}, T_{ave}, D)
  if $t_n\Delta t > T - T_\mu$ **then**
    Perform TI-COH-CELL(μ_{dev}, Ψ_{dev}, T_μ, N_n, d, D, `dimBlock`, `dimThreadBlocks`)
Execute Sum-Kernel<<<`dimBlock, dimThreadBlocks`>>>(N_{dev}, Ψ_{dev}, D)
then scale N_{dev} by grid cell area: $N_{\text{dev}} \leftarrow N_{\text{dev}} \cdot \Delta x \Delta y$
Transfer data from device to host: $\Psi \leftarrow \Psi_{\text{dev}}$, $I \leftarrow I_{\text{dev}}$, $N \leftarrow N_{\text{dev}}$, $\mu \leftarrow \mu_{\text{dev}}$
return Ψ, I, N, μ

a 2D array are known. For most CUDA libraries, such a catenated data layout is well supported.

In this context, the temporal progression of SSFT is observed from 0 to T, with increments of Δt at each step. To calculate the real-time number of particles, the kernel, which presents the summation of the matrix, denoted Sum-Kernel, is used through the parallel reduction method of Ref. [60]. The operation of SSFM in time interval $[t, t + \Delta t]$ is packaged into a sequence of kernels called SSFT-CELL (see Algoithm 2). In this pseudocode, we focus on the time-integrated operation such as the intensity and the mutual

spatial coherence (see section 2.3.3.3), which are obtained, respectively, through kernel TI-Intensity-Kernel (see Algoithm 3) and a sequence of kernels denoted TI-CohCell (see Algoithm 4). As mentioned in section 3.3.3, all the kernels of Algoithm 1 are launched from the host and executed on the device. Moreover, all the size of the predefined matrix in the host are known. To obtain the best performance, one goal of CUDA computing is to reduce the data transfer between the host and the device [61] due to the fact that the data transfer between them is expensive, so it is better to complete all tasks before sending the data back to the host.

3.4.2 Algorithm of the self-defined kernels

Defining the kernel in CUDA is not very different from how the function is defined in CPU, as long as extra attention is paid to the thread and memory hierarchy (see section 3.3.2). The algorithms shown later may also be useful to the application running on multicore-enabled CPUs or different hardware/software devices/network. In section 3.4.2.1, I will briefly introduce the parallel reduction algorithm, widely used for calculating the number of particles and finding the maximum/minimal value of the arrays. In section 3.4.2.1, the algorithms related to SSFM in time interval $[t, t + \Delta t]$ (see procedure 3.18) are explained. The physical quantities extracted in the real-time procedure, such as the time-integrated intensity and the time-integrated spatial mutual coherence factor, are detailed in section 3.4.2.3.

3.4.2.1 Parallel reduction

jThe number of particles in the wavefunction at arbitrary time t is obtained by integration over all spatial space, that is, $\int |\Psi(t, \boldsymbol{r}_{\parallel})|^2 d\boldsymbol{r}_{\parallel}$. Consider the rectangular approximation method. Integration is converted into a matrix summation problem multiplied by the area of each grid of the spatial space (see line number 9 of Algoithm 1). The economic way of performing matrix summation in CUDA is through parallel reduction, although it is less trivial than how it is executed in the CPU; for example, in the CPU, we can loop through the whole matrix with the addition operator applied at each iteration. For CUDA, the data is stored in different thread blocks (see section 3.3), and the reduction algorithm performs the summation of each thread block independently. As shown in Fig. 3.4, the reduction is expressed as a tree-based approach for a single thread block.

In our practical application scenarios, data are further transferred from the GPU's global memory to its shared memory[6]. Each thread block has shared memory, similar to the

[6]Note that the reduction layout from Fig. 3.4 can lead to shared memory bank conflicts, resulting in lower bandwidth usage. The example of a non-optimized case shown in Fig. 3.4 is for brevity, but it is indicative of demonstrating the core of the parallel reduction. For more details on the optimization of the parallel reduction, one may check Ref. [60].

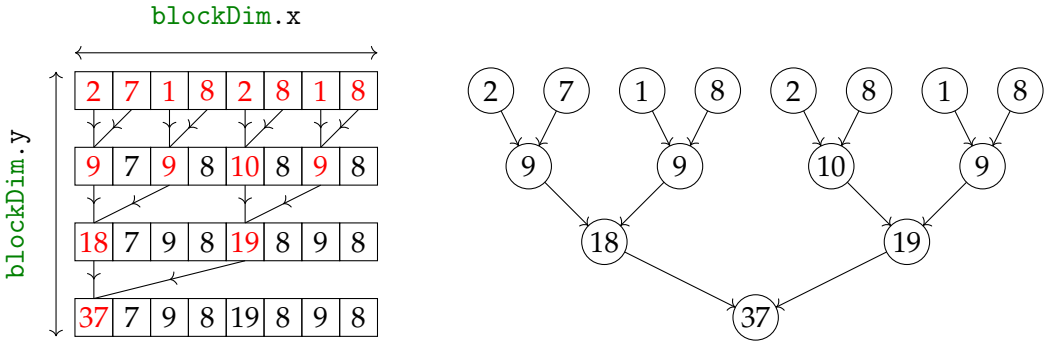

FIGURE 3.4: Illustration of the parallel reduction algorithm shown in (left) a single black thread and (right) the tree. (The figure is adapted from Ref. [60])

CPU cache. All threads in the same thread block can access shared memory faster than global memory. To prepare the data for shared memory, we still need to transfer them from the global memory first, meaning that if the target data sets are used only once, it may not be worth transferring them to shared memory. We want to use shared memory for the reduction because the tree-based approach requires the repetitive usage of the same sets of data to perform the summation at different levels. The application of the parallel reduction algorithm used here can also be modified to find the maximal or minimal values of an array by replacing the addition operation with the comparison operation.

3.4.2.2 Operations related to the Fourier transform

Algorithm 2: Split-Step Fourier Method for Time Interval $[t, t + \Delta t]$

procedure SSFM-CELL(Ψ_{dev}, $\mathcal{P}_{\text{dev}}$, $\mathcal{N}_{\text{dev}}$, D, Δt, `dimBlock`, `dimThreadBlocks`)
  $\Psi_1 \leftarrow \mathcal{N}$-Kernel<<<`dimBlock, dimThreadBlocks`>>>($\mathcal{N}_{\text{dev}}(\Psi_{\text{dev}})$, Ψ_{dev}, D, Δt)
  $\Psi_1^k \leftarrow$ `cuFFT`$[\Psi_1$, `CUFFT_FORWARD`$]$
  $\Psi_1^k \leftarrow$ ZeroFrequencyShift-Kernel<<<`dimBlock, dimThreadBlocks`>>>(Ψ_1^k, D)
  $\Psi_2^k \leftarrow \mathcal{P}$-Kernel<<<`dimBlock, dimThreadBlocks`>>>($\mathcal{P}_{\text{dev}}$, Ψ_1^k, D, Δt)
  $\Psi_2^k \leftarrow$ ZeroFrequencyShift-Kernel<<<`dimBlock, dimThreadBlocks`>>>(Ψ_2^k, D)
  $\Psi_2 \leftarrow$ `cuFFT`$[\Psi_2^k$, `CUFFT_INVERSE`$]$
  $\Psi_2 \leftarrow$Normalization-Kernel<<<`dimBlock, dimThreadBlocks`>>>(Ψ_2, D)
  $\Psi_{\text{dev}} \leftarrow \mathcal{N}$-Kernel<<<`dimBlock, dimThreadBlocks`>>>($\mathcal{N}_{\text{dev}}(\Psi_2)$, Ψ_2, D, Δt)
  return Ψ_{dev}

The SSFM-CELL referring to the procedure 3.18 is illustrated in Algoithm 2. In CUDA, taking `cuFFT` for FFT first and then applying the IFFT, one cannot obtain the same input data, but a normalization of the output data divided by the data size after the IFFT is required. Algoithm 2.1 illustrates a self-defined kernel about normalization. The iterations from both dimensions have access to the data following the thread blocks data structure introduced in section 3.3.3. To simplify the procedure, we have assumed that the data size is smaller than the total number of threads in a grid; otherwise, the

grid-stride `blockDim.x * gridDim.x` should be added to the loop (see an example of the addition operation from section 3.3.3). After execution, the matrix Ψ_{dev} is updated, so it is unnecessary to allocate a new address to the memory for the output data.

Algorithm 2.1: Normalization Kernel for `cufft` Inverse Computation

1: **kernel:** Normalization-Kernel(Ψ_{dev}, D)
2: `Id_x` $\leftarrow$ `threadIdx.x + blockIdx.x * blockDim.x`
3: `Id_y` $\leftarrow$ `threadIdx.y + blockIdx.y * blockDim.y`
4: **if** (`Id_x` $< D$) && (`Id_y` $< D$) **then**
5: $\quad \Psi_{dev}(\texttt{Id\_x}, \texttt{Id\_y}) = \Psi_{dev}(\texttt{Id\_x}, \texttt{Id\_y})/D^2$
6: **return** Ψ_{dev}

In line number 4 and 6 of Algoithm 2, two zero-frequency shifting kernels are called because after the first `cuFFT` the data from the center are shifted to the edges. However, the operation involved with the momentum operator should be performed in the initialized default ordering at the beginning; besides, after the operation with the momentum operator, we still need to shift the 2D data from the center to the edges because the input data ordering of the IFFT obtained from `cuFFT` (line number 7 of Algoithm 2) also expects a shifted data ordering. Since the data size is always an even number (power

Algorithm 2.2: Implementing Zero-Frequency Shift in Even-Sized 2D Data

1: **kernel:** ZeroFrequencyShift-Kernel(Ψ_{dev}, D)
2: `Id_x` $\leftarrow$ `threadIdx.x + blockIdx.x * blockDim.x`
3: `Id_y` $\leftarrow$ `threadIdx.y + blockIdx.y * blockDim.y`
4: **if** (`Id_x` $< D$) **then**
5: $\quad i \leftarrow (\texttt{Id\_x} + D/2)$ **MOD** D
6: $\quad$ **if** (`Id_y` $< D$) **then**
7: $\quad\quad j \leftarrow (\texttt{Id\_y} + D/2)$ **MOD** D
8: $\quad\quad \Psi_{dev}(i, j) = \Psi_{dev}(\texttt{Id\_x}, \texttt{Id\_y})$
9: **return** Ψ_{dev}

of two, see section 3.3.2), it is identical for shifting the data from both center-to-edge (forward) and edge-to-center (inverse) directions. Algoithm 2.2 illustrates the kernel of the zero-frequency shifting. The kernel for nonlinear operation and momentum (lin-

Algorithm 2.3: Nonlinear Operator Kernel Implementation

1: **kernel:** $\mathcal{N}$-Kernel($\mathcal{N}_{dev}(\Psi_{dev})$, Ψ_{dev}, D, Δt)
2: `Id_x` $\leftarrow$ `threadIdx.x + blockIdx.x * blockDim.x`
3: `Id_y` $\leftarrow$ `threadIdx.y + blockIdx.y * blockDim.y`
4: **if** (`Id_x` $< D$) && (`Id_y` $< D$) **then**
5: $\quad \Psi_{dev}(\texttt{Id\_x}, \texttt{Id\_y}) = \exp\left[\frac{1}{2} * \mathcal{N}_{dev}(\texttt{Id\_x}, \texttt{Id\_y})\right] * \Psi_{dev}(\texttt{Id\_x}, \texttt{Id\_y})$
6: **return** Ψ_{dev}

ear) operation is given, respectively, by Algoithm 2.3 and Algoithm 2.4. We need to remember that both wavefunctions and exponential terms are complex-valued matrices, and the pointwise product of two complex matrices needs to be treated separately

in CUDA in real and complex components. The matrix representing the linear operator

Algorithm 2.4: Momentum Operator Kernel Implementation

1: **kernel:** $\mathcal{P}$-Kernel($\mathcal{P}_{\text{dev}}$, Ψ_{dev}, D, Δt)
2: `Id_x` $\leftarrow$ `threadIdx.x + blockIdx.x * blockDim.x`
3: `Id_y` $\leftarrow$ `threadIdx.y + blockIdx.y * blockDim.y`
4: **if** (`Id_x` $< D$) && (`Id_y` $< D$) **then**
5: $\quad \Psi_{\text{dev}}(\texttt{Id\_x}, \texttt{Id\_y}) = \exp\left[\mathcal{P}_{\text{dev}}(\texttt{Id\_x}, \texttt{Id\_y})\right] * \Psi_{\text{dev}}(\texttt{Id\_x}, \texttt{Id\_y})$
6: **return** Ψ_{dev}

in momentum space is a constant [see Eq. 3.11]; instead, the nonlinear operator contains all the information about pumping configurations, reservoir density, scattering, and decay [see Eq. 3.3]. Since the Ψ_{dev} after each kernel from Algoithm 2 is up to date, the accuracy up to Δt^3 still holds (see Section 3.2).

3.4.2.3 Time-integrated operation

The time-integrated intensity is frequently used in chapter 4 and chapter 5. The kernel to carry out the intensity integrated in time is given by Algoithm 3. The conditional statement of line number 5 or 7 of Algoithm 1 determines whether or not the integrated operation in time is executed. In practice, the time step between wavefunctions can be

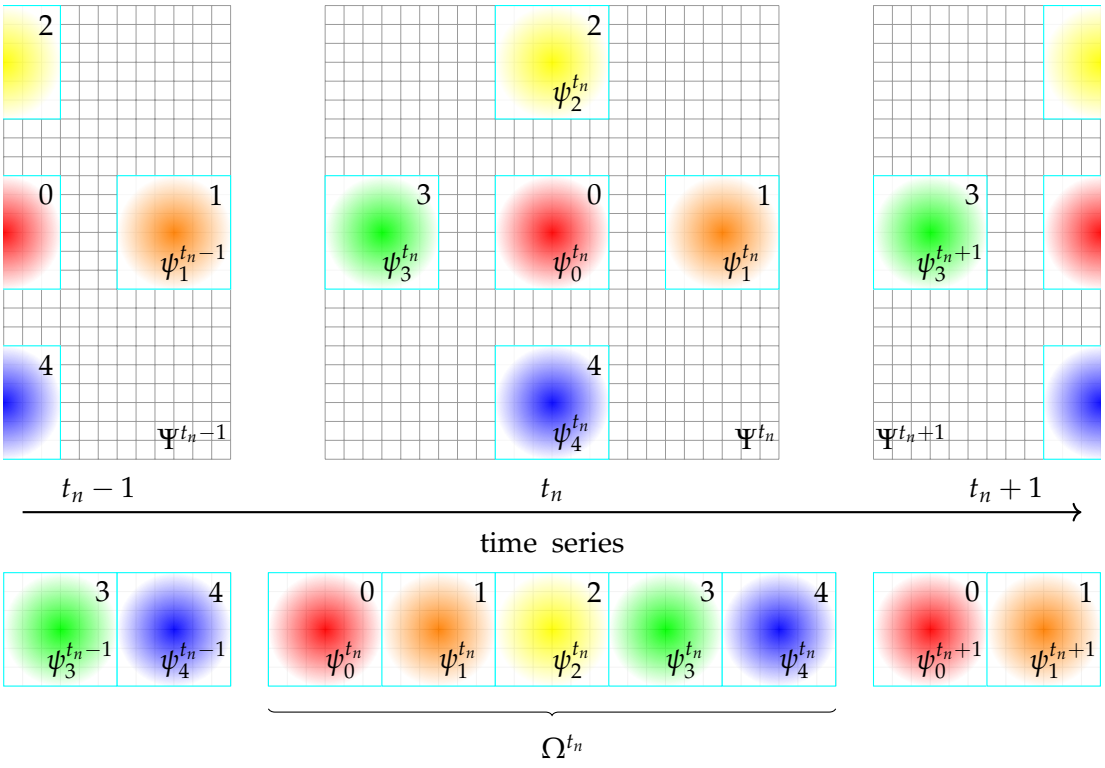

FIGURE 3.5: Sketch of the time-integrated mutual coherence factor presented in the time-sequence-spatial grid.

chosen on a custom basis, which also applies to the kernel of the time-integrated spatial coherence function (see Algoithm 4).

The realization of time-integrated intensity is straightforward: When the conditional statement is true, the intensity of the complex-valued real-time wavefunctions is calculated; then the addition of the current and the previously obtained intensity is executed and eventually is divided by the averaged time period. Repeat the kernel $T_{\text{ave}}/\Delta t$ times, and the final time updated I_{dev} is the one we expect. The mutual coherence func-

Algorithm 3: Time-Integrated Intensity Calculation of Wavefunctions

1: **kernel:** TI-Intensity-Kernel(I_{dev}, Ψ_{dev}, T_{ave}, D)
2: `Id_x` $\leftarrow$ `threadIdx.x + blockIdx.x * blockDim.x`
3: `Id_y` $\leftarrow$ `threadIdx.y + blockIdx.y * blockDim.y`
4: **if** $(\texttt{Id\_x} < D)\&\&(\texttt{Id\_y} < D)$ **then**
5: $\quad I_{\text{dev}}(\texttt{Id\_x}, \texttt{Id\_y}) = (I_{\text{dev}}(\texttt{Id\_x}, \texttt{Id\_y}) + |\Psi_{\text{dev}}(\texttt{Id\_x}, \texttt{Id\_y})|^2)/(T_{\text{ave}}/\Delta t)$
6: **return** I_{dev}

tion first defined in Eq. (2.73) is given by

$$\mu_{\mathcal{LM}} = \frac{C_{\mathcal{LM}}}{\sqrt{C_{\mathcal{MM}} \cdot C_{\mathcal{LL}}}}, \tag{3.19}$$

$$C_{\mathcal{LM}} = \langle \psi_{\mathcal{L}}{}^* \cdot \psi_{\mathcal{M}} \rangle, \;\; C_{\mathcal{LL}} = \langle \psi_{\mathcal{L}}{}^* \cdot \psi_{\mathcal{L}} \rangle, \;\; C_{\mathcal{MM}} = \langle \psi_{\mathcal{M}}{}^* \cdot \psi_{\mathcal{M}} \rangle. \tag{3.20}$$

Here, as shown in Fig. 3.5, for simplicity, we consider that the grid space consists of 5 nodes, namely $N_n = 5$ of Algoithm 1, indexed from 0 to 4. The first thing is to crop the regions with $d \times d$ dimensions where all nodes are located, then resemble them in a new array prepared for future operation. Thus, $C_{\mathcal{LM}}$ can be expressed as

$$C_{\mathcal{LM}} = \frac{1}{T_{\text{coh}}/\Delta t} \sum_{t_n=(T-T_{\text{coh}})/\Delta t}^{T/\Delta t} C_{\mathcal{LM}}^{t_n}, \tag{3.21}$$

$$C_{\mathcal{LM}}^{t_n} = \frac{1}{d^2 \Delta x \Delta y} \sum_{i=0}^{d-1} \sum_{j=0}^{d-1} \psi_{\mathcal{L}}^{t_n *}(x_i, y_j) \cdot \psi_{\mathcal{M}}^{t_n}(x_i, y_j). \tag{3.22}$$

Since both $(T_{\text{coh}}/\Delta t)^{-1}$ and $(d^2 \Delta x \Delta y)^{-1}$ are constant, these terms can be canceled when calculating $\mu_{\mathcal{LM}}$ [see Eq. (3.19)]. Equation (3.22) expresses that wavefunctions on $\mathcal{L}$ and $\mathcal{M}$ are mapped onto the matrix with the same dimension; however, in CUDA, they are regrouped into a $d \times N_n d$ matrix denoted Ω^{t_n}. Assume that the wavefunctions over area $\mathcal{L}$ are taken to multiply with all possible wavefunctions over $\mathcal{M}$, **MOD** operation is needed when the thread iterates through Ω^{t_n}, as illustrated in Algoithm 4.1

Algoithm 4 illustrates the procedure for calculating the mutual spatial coherence function, in the time interval $[t, t + \Delta t]$, of polariton lattices consisting of N_n nodes. Before the calculation, we crop the matrix N_n with dimension $d \times d$ and reassemble them into the complex-valued matrix Ω^{t_n} (see Fig. 3.5 for the case with $N_n = 5$). The multiplication of two chosen matrices [see Eq. (3.22)], which are subsets of Ω^{t_n}, is illustrated in

Algorithm 4: Computation of Time-Integrated Spatial Coherence

1: **procedure** TI-COH-CELL(μ_{dev}, Ψ_{dev}, T_μ, N_n, d, D, `dimBlock`, `dimThreadBlocks`)
2: Initialize:
▷ *Prepare complex-valued matrices for the following quantities:*
▷ *Cropped wavefunctions:*
$\{\sum_{i=0}^{d-1}\sum_{j=0}^{N_n d-1}\Omega^{t_n}(x_i, y_j)\}$ (complex-valued matrix)
▷ *Multiplied wavefunctions (type $\mathcal{LM}$):*
$\{\sum_{i=0}^{d-1}\sum_{j=0}^{N_n d-1} C^{t_n}_{\mathcal{LM}}(x_i, y_j)\}$ (complex-valued matrix)
▷ *Multiplied wavefunctions (type $\mathcal{MM}$):*
$\{\sum_{i=0}^{d-1}\sum_{j=0}^{N_n d-1} C^{t_n}_{\mathcal{MM}}(x_i, y_j)\}$ (complex-valued matrix)
▷ *Summation of the type $\mathcal{LM}$ matrix:*
$\{\sum_{l=0}^{N_n d-1}\text{SumC}^{t_n}_{\mathcal{LM}}(l)\}$ (complex-valued matrix)
▷ *Summation of the type $\mathcal{MM}$ matrix:*
$\{\sum_{l=0}^{N_n d-1}\text{SumC}^{t_n}_{\mathcal{MM}}(l)\}$ (complex-valued matrix)
▷ *Extract regions $0, 1, ...N_n - 1$, from Ψ_{dev} and assign to Ω^{t_n}*
3: $\Omega^{t_n} \leftarrow \{\sum_{l=0}^{N_n-1}\psi_l^{t_n}\}$
▷ *Execute CUDA kernel to compute $C^{t_n}_{\mathcal{LM}}$ and $C^{t_n}_{\mathcal{MM}}$ using Ω^{t_n}.*
4: C^{t_n}-Kernel<<<`dimBlock, dimThreadBlocks`>>>($C^{t_n}_{\mathcal{LM}}$, Ω^{t_n}, N_n, d, $\mathcal{LM}$)
5: C^{t_n}-Kernel<<<`dimBlock, dimThreadBlocks`>>>($C^{t_n}_{\mathcal{MM}}$, Ω^{t_n}, N_n, d, $\mathcal{MM}$)
▷ *Execute CUDA kernel to calculate the summation for each $C^{t_n}_{\mathcal{LM}}$ and $C^{t_n}_{\mathcal{MM}}$, results are stored in $\text{SumC}^{t_n}_{\mathcal{LM}}$ and $\text{SumC}^{t_n}_{\mathcal{MM}}$.*
6: Sum-Kernel<<<`dimBlock, dimThreadBlocks`>>>($\text{SumC}^{t_n}_{\mathcal{LM}}$, $C^{t_n}_{\mathcal{LM}}$, $N_n d$)
7: Sum-Kernel<<<`dimBlock, dimThreadBlocks`>>>($\text{SumC}^{t_n}_{\mathcal{MM}}$, $C^{t_n}_{\mathcal{MM}}$, $N_n d$)
▷ *Compute temporary spatial coherence, μ^{tem}_{dev} based on the sums from previous step.*
8: $\mu^{\text{tem}}_{\text{dev}} \leftarrow \text{SumC}^{t_n}_{\mathcal{LM}} / \sqrt{\text{SumC}^{t_n}_{\mathcal{MM}} \cdot \text{SumC}^{t_n}_{\mathcal{LL}}}$
▷ *Calculate final spatial coherence, μ_{dev} by averaging it with μ^{tem}_{dev} over time step $T_{\text{coh}}/\Delta t$.*
9: $\mu_{\text{dev}} \leftarrow (\mu_{\text{dev}} + \mu^{\text{tem}}_{\text{dev}})/(T_{\text{coh}}/\Delta t)$
10: **return** μ_{dev}

Algorithm 4.1. The summation of the matrix $C^{t_n}_{\mathcal{LM}}$ and $C^{t_n}_{\mathcal{LL}}$ is taken (see line number 6 and 7 of Algoithm 4.0) through the Sum-Kernel, which aims to sum up different segments of a matrix, is the same one defined in Algoithm 1, and both are realized with the parallel reduction defined in section 3.4.2.1.

The mutual coherence factor over the area $\mathcal{L}$ and $\mathcal{M}$ at time t_n is obtained directly from Eq. (3.19) by replacing C^{t_n} with the sum denoted SumC^{t_n} (see line number 8 of Algoithm 4). The last step is similar to the way the time-integrated intensity is calculated: iterating through the current coherence factor with the previous one and then dividing by $T_\mu \Delta t$ over the period. In addition to the brevity, the wavefunctions belonging to region $\mathcal{L}$, which are multiplied by the rest of the regions (see Algoithm 4.1), can also be uploaded to the shared memory for fast operation because the matrix is used repeatedly. Similar data arrangement in the shared memory can also be found in summation over the whole or part of the matrix (parallel reduction see section 3.4.2.1),

Algorithm 4.1: Kernel Implementation for Cropped Matrix Dot Product

kernel: C^{t_n}-Kernel(C^{t_n}, Ω^{t_n}, N_n, d, instruction)
`Id_x` $\leftarrow$ `threadIdx.x + blockIdx.x * blockDim.x`
`Id_y` $\leftarrow$ `threadIdx.y + blockIdx.y * blockDim.y`
if (`Id_x` $< d$)&&(`Id_y` $< N_n d$) **then**
    if instruction $= \mathcal{LM}$ is ture **then**
        C^{t_n}(`Id_x`, `Id_y`) $= {\Omega^{t_n}}^*$(`Id_x` **MOD** `d`, `Id_y` **MOD** `d`) $\cdot\, \Omega^{t_n}$(`Id_x`, `Id_y`)
    if instruction $= \mathcal{MM}$ is ture **then**
        C^{t_n}(`Id_x`, `Id_y`) $= {\Omega^{t_n}}^*$(`Id_x`, `Id_y`) $\cdot\, \Omega^{t_n}$(`Id_x`, `Id_y`)
return C^{t_n}

and the Gaussian convolution of the pump profile and the step function (see chapters 4 and 5).

3.5 Conclusions

The chapter begins by delving into an examination of SSFM, alongside a detailed exploration of the CUDA hardware and software structure. The discussion culminates with the introduction of a novel algorithm that facilitates the efficient integration of SSFM and CUDA.

Section 3.2 explains not only why the SSFM works to solve the nonlinear Schrödinger equation, but also to what extent the accuracy it could achieve under what circumstances. To balance precision and performance, the time step we chose through this thesis is $\Delta t = 0.01$ ps, which also gives a larger energy scale, compared to Δt larger than we chose, for a given sampling time in the energy spectrum simulation (not shown in this chapter for the brevity of the introduction). The accuracy used in this thesis is $\mathcal{O}(\Delta t^3)$ corresponding to Eq. (3.7), but one can have higher order like $\mathcal{O}(\Delta t^4)$ and $\mathcal{O}(\Delta t^5)$ by modifying the expression of Eq. (3.7) which can be found in Ref. [56]. The GPE simulation usually requires boundary conditions in real and momentum space, which go, respectively, to the nonlinear operator [see Eq. (3.3)] and linear operator [see Eq. (3.2)]. There are Dirichlet and periodic boundary conditions in most cases of GPE simulation. Extra care should be taken with Dirichlet boundary conditions, especially when pumping is strong near the boundary. In such cases, the reflection cannot be neglected, but can still be diminished by either making the spatial grid larger due to the constant lifetime of the polaritons or creating a perfectly matched layer (PML) around the boundary where the incoming polariton flow can be absorbed. However, sometimes to match the real case in the experiment or to artificially produce such a feature on the boundary, it does not mean that we have to diminish the reflection every time we perform the simulation. Still, we can always make one layer of fake boundary to satisfy the condition we need, then add another PLM as the real boundary.

Section 3.3 gives a brief introduction to the CUDA from both hardware and software perspectives. Due to the coherent integration with the thread and memory hierarchy, the launch parameters may vary based on different devices to achieve the best performance. For simplicity, more attention is paid to the thread block structure because it has the closest connection with the programming side. The launch parameters, which determine how the task is divided and conquered, are organically changing for different data inputs or for the purpose of manipulating the data. Only tweaking the thread block structure is not enough to achieve high bandwidth usage per kernel, and memory management plays an important role in optimization through CUDA programming.

Section 3.4 shows the main algorithm that integrates with the GPE, the time-integrated intensity, and the time-integrated spatial coherence factor. The parallel reduction introduced in section 3.4.2.1 provides an example of summing up all the elements of a matrix consisting of multiple submatrices which do not effectively communicate with each other. The divide-and-conquer idea behind parallel reduction can also help build the computing network. For example, to obtain the summation of an extremely large matrix based on many CPU-based devices linked together, one may expect a similar algorithm used in GPU is applied to this network. An earlier work on parallel reduction can be found in Ref. [62].

The GPU solver incorporates two types of functions: self-defined kernels and integrated kernels provided directly by the CUDA API. An example of the latter is the `cuFFT` function from Algoithm 2. These built-in functions can be initiated without specifying launch parameters, as the optimization is performed automatically based on current hardware information.

Chapter 4

Reservoir optics with exciton-polariton condensates

4.1 Introduction

The GPE governing the polariton flow presented in section 2.3.3 is similar to the Maxwell equation ruling the electromagnetic wave, which naturally leads to the question: Can the polariton flow be concentrated the same way that a planar light wave does through the lens? This question will be answered in this chapter, and the system with all-optical polariton beyond the scope of the conventional light-lens setup will be studied. At the microscale level, progress related to guiding and focusing planar light waves has been made in the scope of miniaturized optical technologies, reliant on dispersion management, ranging from microlens arrays [63] to optical circuitry and logic gates [64], has been made. A variety of techniques exist to focus planar light, such as metamaterials [65, 66], plasmonic lenses [67–69], phase change materials [70], photonic crystals [71, 72], and disordered materials [73]. Despite this, the lensing performed on samples usually cannot be reversed for different configurations.

This chapter introduces an all-optical planar microlensing approach in a semiconductor system, as illustrated in Figs. 2.3 and 4.1. The approach focuses on microcavity polariton condensates with reversible lens configurations. This is made possible as the shape of the blueshift potential landscape closely resembles that of the nonresonant pump, and can be reprogrammed through the spatial light modulator (see section 2.3.3). Many works have also combined the optical control provided by nonresonant lasers in conjunction with engineered photonic potentials such as micropillars,

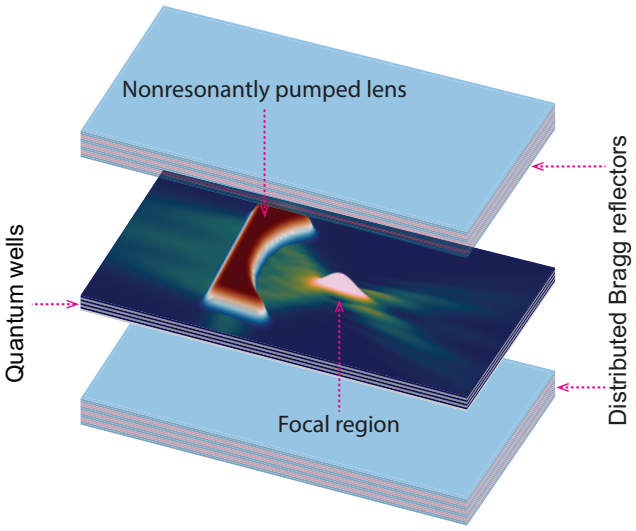

FIGURE 4.1: Sketch of the nonresonant lensing effect with exciton-polariton condensates in a semiconductor microcavity. Quantum well excitons are photoexcited through nonresonant pumping (dark red profiles), while the cavity mirrors (symmetrically distributed Bragg reflectors) provide photon confinement and strong coupling.

microwires, or wedged cavities (i.e., photonic potential gradient) which led to the development of optically controllable interferometers [74, 75]. Alongside these developments in optical control, there is a growing variety of cheaper room temperature materials that operate in the strong coupling regime [9–11] that opens new perspectives on the role of exciton-polaritons in future optical-based technologies [76, 77].

This thesis explores the spatial control of propagating exciton-polariton condensates using nonresonant excitation beams shaped into a planoconcave microlens (see Fig. 4.1). The excitation beam induces a static reservoir of incoherent excitons, which provide both gain and blueshift to the polariton modes [12, 14]. Consequently, excited polaritons experience a complex-valued effective potential landscape that can amplify and phase modulate transmitted waves. When the excitation beam is removed, the reservoir rapidly decays, allowing for rewriting new and different potential landscapes on the same sample location. Recently, similar flexibility with phonon polaritons was demonstrated in a hexagonal boron nitride heterostructure [78].

So far, several studies have addressed the potential of nonresonant all-optical control to manipulate the flow of condensate polaritons. Planar waveguiding effects [79, 80], amplification [15, 16], tailoring the condensate momentum distribution [81], and directional superfluids near equilibrium [82], ring-like potential landscape [83, 84] are studied. A transistor switch is all-optically designed in a source-barrier setup [85] and [86] where the source (nonresonant laser) creates a ballistic flow on polaritons that travel due to a potential gradient engineered into the photonic cavity. When a barrier (another nonresonant laser) is switched on in the path of the traveling polaritons, they are reflected, which characterizes the 'off' state. However, no planar microlensing of

exciton-polaritons has been widely investigated. Considering that lenses are fundamental optical elements in many scientific disciplines, there is an important missing piece in the existing literature on all-optical polariton control.

The rest of the chapter is organized as follows: In section 4.2, as a preparation for the more complicated non-linear polariton system, microlensing with both negative and positive meniscus lens in a damped two-dimensional (2D) Schrödinger system corresponding to the linear (noninteracting) polariton regime is studied. In section 4.3, a source condensate that approximately emits a coherent plane wave polariton flow is nonresonantly excited. This flow impinges on the planoconcave microlens generated by a second nonresonant beam. The response of the condensate waves against this additional microlens potential and developing an argument for the operational requirements of efficient reservoir lensing is analyzed. In section 4.4, a simpler idea of using only a lens-shaped beam pumped above the condensation threshold is investigated, resulting in the spontaneous formation of condensate profiles strongly focused away from their pumped region. Finally, the general conclusion of the reservoir optics scheme is drawn in section 4.5.

4.2 Planar polariton microlensing in the linear regime

Recall a simplified case in the linear regime of GPE in chapter 2 of Eq. (2.67) by adding the wavevector $\boldsymbol{k}_{\parallel}^{s}$,

$$i\hbar\frac{\partial}{\partial t}\Psi(t,\boldsymbol{r}_{\parallel}) = \Big[-\frac{\hbar^2}{2m^*}\nabla_{\parallel}^2 + (V_r + iV_i)f(\boldsymbol{r}_{\parallel}) - i\frac{\hbar}{2}\gamma\Big]\Psi(t,\boldsymbol{r}_{\parallel}) + E(\boldsymbol{r}_{\parallel})e^{-i(\omega_s t - \boldsymbol{k}_{\parallel}^{s}\cdot\boldsymbol{r}_{\parallel})}, \quad (4.1)$$

here V_r and V_i quantify, respectively, the real and imaginary parts of the lens potential with a spatial profile $f(\boldsymbol{r}_{\parallel})$, and $E(\boldsymbol{r}_{\parallel})$ to produce the planar wave is a coherent (resonant) driving field with frequency ω_s and wavevector $\boldsymbol{k}_{\parallel}^{s}$.

Here, the complex lens potential of $(V_r + iV_i)f(\boldsymbol{r}_{\parallel})$ is considered an optically generated potential in polariton systems [**?**] although many other methods are available for designing polaritonic potential landscapes [87]. When it comes to the simulation, the limited resolution coming from spatial light modulators and finite exciton diffusion is accounted by applying Gaussian blurring (convolution) on a step function,

$$f(\boldsymbol{r}_{\parallel}) = \frac{1}{2\pi w^2}\int F(\boldsymbol{r}'_{\parallel})e^{-|\boldsymbol{r}_{\parallel}-\boldsymbol{r}'_{\parallel}|^2/2w^2}\,d\boldsymbol{r}'_{\parallel} \quad (4.2)$$

where

$$F(\boldsymbol{r}_{\parallel}) = \begin{cases} 1 & \text{for } \boldsymbol{r}_{\parallel} \in \mathcal{G} \\ 0 & \text{else,} \end{cases} \quad (4.3)$$

where $\mathcal{G}$ is the lens area. This thesis uses 2.0 μm full-width-at-half-maximum (FWHM) to calculate all lens shapes with a Gaussian blur corresponding to $w \approx 0.85\,\mu m$. To cancel the time-dependent part, the steady-state solutions $\Psi(\boldsymbol{r}_\parallel, t) = \psi(\boldsymbol{r}_\parallel)e^{-i\omega_s t}$ is substituted into Eq. 4.1 leaving the time-independent Schrödinger equation,

$$\hbar\omega_s\psi = \left[-\frac{\hbar^2}{2m^*}\nabla_\parallel^2 + (V_r + iV_i)f(\boldsymbol{r}_\parallel) - i\frac{\hbar}{2}\gamma\right]\psi + E(\boldsymbol{r}_\parallel)e^{ik_\parallel^s\cdot\boldsymbol{r}_\parallel}. \tag{4.4}$$

The spatial profile of the lens slowly decays from the deep inside the potential region with 1 to the edge with 0. Taking the approximation $f(\boldsymbol{r}_\parallel) \approx 1$, the homogeneous Helmholtz equation is obtained,

$$\nabla_\parallel^2\psi + k_\parallel^2\psi = 0, \tag{4.5}$$

$$k_\parallel^2 = \frac{2m^*}{\hbar^2}\left[\hbar\omega_s - V_r - i\Big(V_i - \frac{\hbar}{2}\gamma\Big)\right]. \tag{4.6}$$

Under resonant driving, $k_\parallel^s = \sqrt{2m^*\omega_s/\hbar}$, the refractive index of the complex-valued potential with respect to the source is,

$$n' = \sqrt{1 - \frac{V_r}{\hbar\omega_s} - \frac{i}{\hbar\omega_s}\Big(V_i - \frac{\hbar}{2}\gamma\Big)}. \tag{4.7}$$

Here, only propagating waves and not evanescent waves inside the lens region are considered meaning that $V_r < \hbar\omega_s$ from Eq. (4.7). To separate the real and imaginary parts of the refractive index, the system is taken to have net losses everywhere and thus $V_i - \hbar\gamma/2 < 0$, so it reads

$$n' = n + i\kappa, \tag{4.8}$$

where

$$n = \sqrt{1 - \frac{V_r}{\hbar\omega_s}}, \tag{4.9}$$

$$\kappa = \frac{|V_i - \hbar\gamma/2|}{\hbar\omega_s n}. \tag{4.10}$$

Here, to obtain the above form, the assumption that the real detuning is larger than the imaginary detuning $|V_i - \frac{\hbar\gamma}{2}| \ll |V_r - \hbar\omega_s|$ is taken.

4.2.1 Negative meniscus lens

Here an example of a negative meniscus lens is considered. For a planoconcave-shaped potential whose edge (i.e., FWHM) is depicted with a solid green line in Figs. 4.2(b) and 4.2(e), recall the Lensmaker's equation in the ray optics limit where the focal length

f_N follows,

$$f_N = \frac{R}{1 - n_N}. \tag{4.11}$$

Here, the subscript N denotes the negative meniscus lens, and R is the radius of curvature of the back surfaces of the lens. In the case of planar microlenses, whose characteristic spatial scale is only several wavelengths, the focal length will deviate from Eq. (4.11) due to pronounced scattering and interference of the waves impinging on the

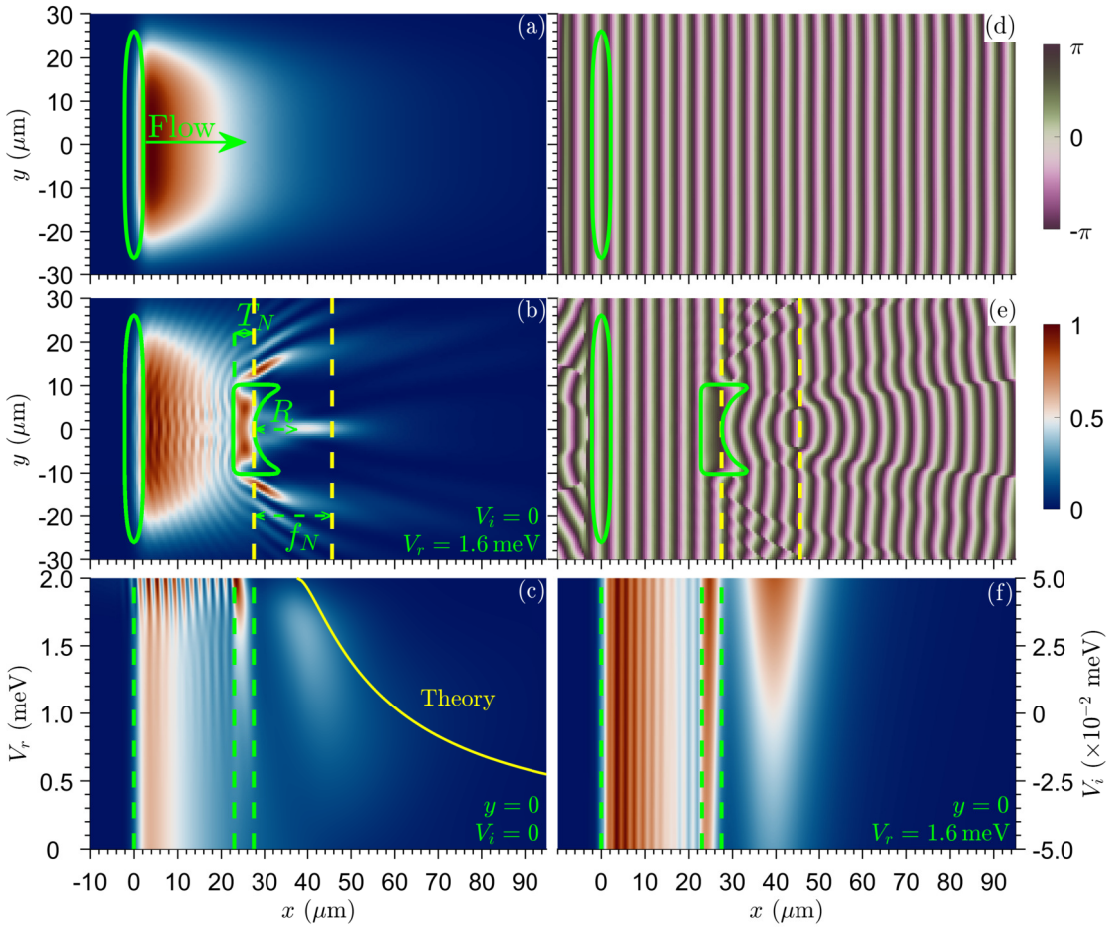

FIGURE 4.2: (a),(b) The normalized density, $|\Psi|^2$, and (d),(e) phase, $\arg(\Psi)$, of the wave function without (a),(d) and with (b),(e) the planoconcave-shaped-lens potential. The source and lens are outlined with solid green lines. (c),(f) Line profile of the wavefunction density along the lens axis ($y = 0$) as a function of varying real (c) and imaginary (f) parts of the potential. In (b) and (e), the yellow dashed lines indicate the principal plane of the lens and the focal point with distance f_N. The green vertical dashed lines in (c) and (f) indicate the source location and the front and back surface of the lens.

lens. Thus, the steady state of Eq. (4.1) is numerically solved with CUDA (see chapter 3) under resonant excitation of plane waves that pass through the planoconcave microlens. The parameters, based on state-of-the-art inorganic microcavities, for the generation of polariton condensates [31] are chosen: $\gamma^{-1} = 5.5\,\text{ps}$ and $m^* = 4.9 \times 10^{-5} m_0$ where m_0 is the mass of free electrons.

Since $n_N = 1$ and $n_N < 1$ are outside and inside the lens, respectively, an incident planar wavefront from the left will transmit through the lens to converge into a cylindrical wavefront on the right side. The numerical solution for the steady states of Eq. (4.1) under resonant excitation on the left side of the lens with a profile, $E(\boldsymbol{r}_\parallel) \propto \exp[-x^2/(2\sigma_x^2) - y^2/(2\sigma_y^2)]$ whose FWHM is outlined green in Fig. 4.2(a) centered at $x = 0$ is obtained. The energy of the source excitation is set to $\hbar\omega_s = 2.0\,\text{meV}$ so as to have a rapidly varying phase front and remain within the parabolic (dispersion) regime. The corresponding steady-state density and phase profiles of $\Psi(\boldsymbol{r}_\parallel)$ without any lens potential are shown in Figs. 4.2(a) and 4.2(d).

When a planoconcave potential $V(\boldsymbol{r}_\parallel)$, of size in the order of several wavelengths ($\lambda_s \approx 3.9\ \mu\text{m}$), is introduced, both transmitted and scattered waves contribute in a complicated way to the focal region on the right side of the lens [see Fig. 4.2(b)]. Here, we set $R = 10.0\,\mu\text{m}$ and the lens' thickness $T_N = 4.5\,\mu\text{m}$ which corresponds to $n_N \approx 0.4472$ and $f_N \approx 18.1\,\mu\text{m}$ indicated by the yellow dashed lines in Figs. 4.2(b) and 4.2(e). A focal region (i.e., the whiteish region of converged/focused waves) that lies outside the lens curvature R and within the ray-optic focal length f_N [Eq. (4.11)], as a consequence of the microscopic nature of the lens shape, is observed. We stress that the low polariton intensity in the focal region is dominated by the rapid decay rate γ used in our simulation. However, condensation of polaritons with long lifetimes reaching $\gamma^{-1} = 270\,\text{ps}$ has also been demonstrated [88], leading to longer propagation lengths and timescales to manipulate the condensate flow.

Figure 4.2(c) shows the line profile of the wavefunction density at $y = 0$ to vary the real potential strength V_r. The focal region shrinks and the focal length decreases as the potential strength increases in qualitative agreement with Eq. (4.11) (solid yellow line). It is worth mentioning that from Eq. (4.6), one can, in principle, achieve epsilon-near-zero ($n_N = 0$) lensing, which has been studied extensively in metamaterials [89], by tuning the excitation frequency. However, at $\hbar\omega_s \approx V_r$, incident waves undergo stronger reflection, leading to a pronounced interference pattern, as in Fig. 4.2(b) to the left of the lens. In addition, varying the imaginary part of the potential V_i in Fig. 4.2(f) shows a clear amplification of the transmitted waves in accordance with the imaginary part of the refractive index in Eq. (4.10).

4.2.2 Positive meniscus lens

For a potential with a double-concave-shaped spatial profile $f(\boldsymbol{r}_{\parallel})$, we recall the Lensmaker's equation in the ray optics limit where the focal length f_P follows,

$$\frac{1}{f_P} = (n_P - 1)\left[\frac{1}{R_1} - \frac{1}{R_2} + \frac{(n_P - 1)T_P}{n_P R_1 R_2}\right]. \tag{4.12}$$

Here, the subscript P denotes the positive meniscus lens, $R_{1,2}$ are the radius of curvature of the front and the back surfaces of the lens, respectively (left and right edges), and T_P represents the lens thickness. In the case of using a positive meniscus lens where

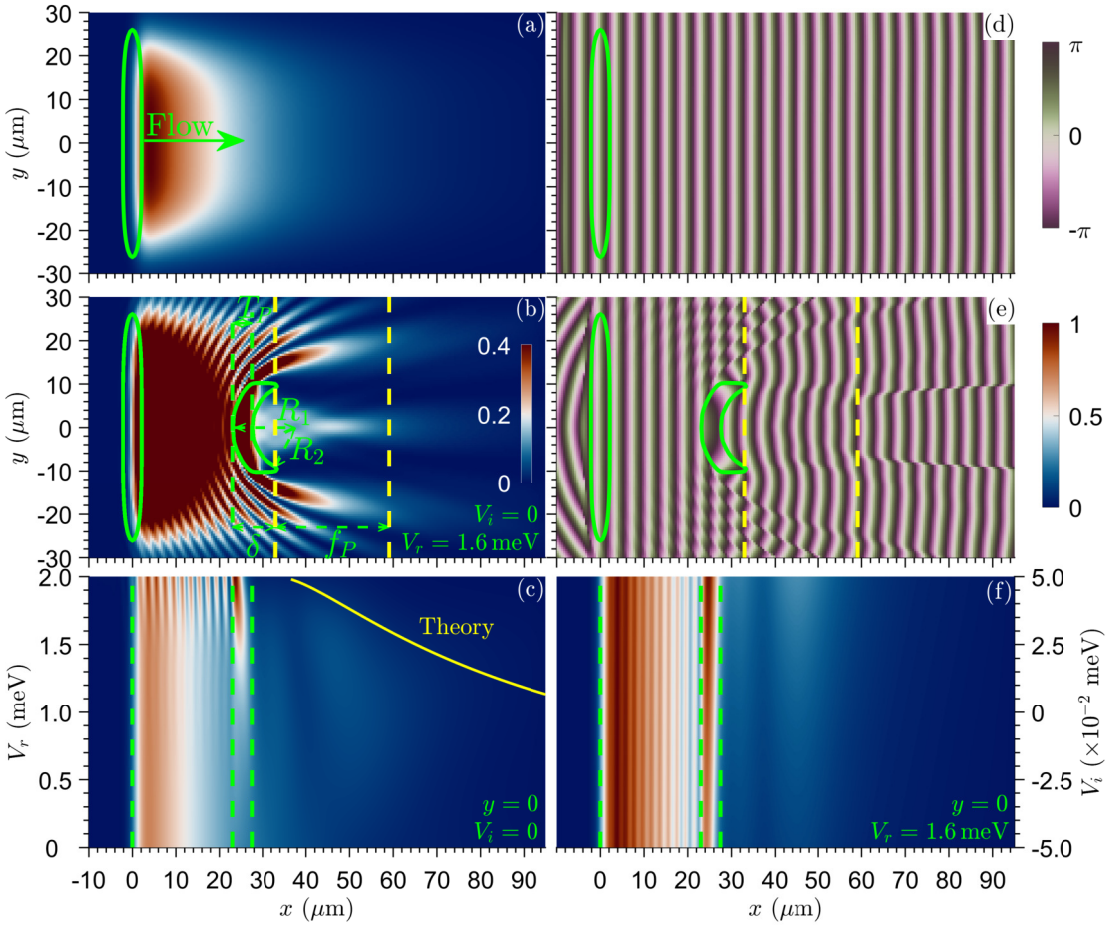

FIGURE 4.3: (a),(b) The normalized density, $|\Psi|^2$, and (d),(e) phase, $\arg(\Psi)$, of the wave function without (a),(d) and with (b),(e) the lens potential. The source and lens are outlined with solid green lines. (c),(f) Line profile of the wavefunction density along the lens axis ($y = 0$) as a function of varying real (c) and imaginary (f) parts of the potential. In (b), to detail the focal region, the value of the normalized density greater than 0.4 is saturated in the colormap. In (b) and (e), the yellow dashed lines indicate the principal plane of the lens and the focal point with distance f_P, and δ is the distance between the front surface and the principal plane (the first yellow dashed line from left to right). The green vertical dashed lines in (c) and (f) indicate the source location and the front and back surfaces of the lens, and T indicates the distance between two green dashed lines.

$R_1 > 0$, the thickness T_P of the lens in Eq. (4.12) needs to be taken into account. It is instructive to define the distance,

$$\delta = f_P \frac{T_P}{R_1}\left(\frac{1}{n_P} - 1\right), \tag{4.13}$$

which refers to the distance between the front surface in the positive meniscus lens and the principal point [see Fig. 4.3(b)]. The radius of the front and back surfaces of the lens is, respectively, $R_1 = 14.5\,\mu$m and $R_2 = 10.0\,\mu$m, and the thickness of the lens $T_P = 4.5\,\mu$m. The radius of the back surface, the thickness of the lens, and the resonant source are the same as those used in Fig. 4.2. For a lens with $V_r = 1.6\,$meV and $V_i = 0\,$meV, $\delta \approx 10.0\,\mu$m and $f_P \approx 26.1\,\mu$m are obtained using Eq. (4.7) in to get the effective refractive index n.

Figure 4.3 shows the same numerical experiment as in Fig. 4.2 using a positive meniscus lens this time. Compared to the negative meniscus lens results, an enhanced scattering of the incident plane wavefront onto the positive meniscus is obtained, resulting in a poorer focused transmission. This result is in contrast to the case presented in Fig. 4.8, where a positive meniscus emitter focuses waves more efficiently than a planoconcave lens (detailed in section 4.4).

4.3 Planar reservoir microlensing with polariton condensates

4.3.1 Generalized Gross-Pitaevskii model

Having characterized the effects of the 2D planoconcave microlens on an incoming plane wave, now the nonlinear regime with condensates of polaritons is taken into account. Recall the 2D GPE coupled to a driven exciton reservoir from Eqs. (2.63) and (2.64),

$$\begin{aligned} i\hbar\frac{\partial}{\partial t}\Psi(t,\boldsymbol{r}_\parallel) &= \Big\{-\frac{\hbar^2}{2m^*}\nabla_\parallel^2 + \alpha|\Psi(t,\boldsymbol{r}_\parallel)|^2 + G\Big[n_X(t,\boldsymbol{r}_\parallel) + \frac{\eta}{\Gamma_X}P(\boldsymbol{r}_\parallel)\Big] \\ &\quad + i\frac{\hbar}{2}\big[Rn_X(t,\boldsymbol{r}_\parallel) - \gamma\big]\Big\}\Psi(t,\boldsymbol{r}_\parallel), \end{aligned} \tag{4.14}$$

$$\frac{\partial}{\partial t}n_X(t,\boldsymbol{r}_\parallel) = -\big[\Gamma_X + R|\Psi(t,\boldsymbol{r}_\parallel)|^2\big]n_X(t,\boldsymbol{r}_\parallel) + P(\boldsymbol{r}_\parallel). \tag{4.15}$$

The parameters used in all simulations of this chapter are based on negatively detuned cavities, $|\chi|^2 = 0.4$, with GaAs-type quantum wells, $g = 1\,\mu$eV$\,\mu$m^2. The remaining parameters are taken similar to those used to describe recent experiments, $\hbar R = 2.8g$; $\eta = 5$; and $\Gamma_X = \gamma$ [22, 23]. We also note that our findings do not critically depend on the parameter values, which can be adjusted through the system properties (e.g.,

exciton-photon detuning or the exciton dipole moment by the appropriate choice of the semiconductor material).

Let us quantify the nonresonant pump as $P(\boldsymbol{r}_\parallel) = P_0 f(\boldsymbol{r}_\parallel)$ where P_0 is a positive scalar denoting the power density of the pump laser and $f(\boldsymbol{r}_\parallel)$ is its profile. It is instructive to define the condensation threshold, which, formally, is a bifurcation point that separates the so-called normal (uncondensed) state ($|\Psi| = 0$) and the condensed state ($|\Psi| \neq 0$). The threshold can be identified as the point where a single frequency component of our system in the linear regime crosses from negative to positive imaginary value (i.e., small $|\Psi|$ starts to grow exponentially over time). Alternatively, one can also estimate the threshold of Eq. (4.14) numerically by expanding the reservoir's steady state,

$$N = \frac{P(\boldsymbol{r}_\parallel)}{\Gamma_X + R|\Psi|^2} = \frac{P(\boldsymbol{r}_\parallel)}{\Gamma_X}\left[1 - \frac{R}{\Gamma_X}|\Psi|^2 + \mathcal{O}(|\Psi|^4)\right] \tag{4.16}$$

and compare the contribution between the zeroth and the first-order terms. Integrating through space, we can write the following inequality:

$$\frac{R}{\Gamma_X}\int f(\boldsymbol{r}_\parallel)|\Psi|^2\, d\boldsymbol{r}_\parallel < \epsilon. \tag{4.17}$$

Here, $\epsilon \ll 1$ is some small, reasonably chosen numerical tolerance to determine the threshold. Physically, this expression simply states that any nonlinear effects on the reservoir are small around the threshold. In this weak nonlinear regime discussed in section 2.3.3.1, the potential generated by the pump is approximately,

$$V(\boldsymbol{r}_\parallel) \simeq \frac{P(\boldsymbol{r}_\parallel)}{\Gamma_X}\left[G\,(1+\eta) + i\frac{\hbar}{2}R\right]. \tag{4.18}$$

Separating the real and imaginary parts gives,

$$V_r = \frac{P_0}{\Gamma_X}G(1+\eta), \tag{4.19}$$

$$V_i = \frac{P_0}{2\Gamma_X}\hbar R. \tag{4.20}$$

For a homogeneous pump $P(\boldsymbol{r}_\parallel) = P_0$, the threshold power corresponds to the balance of gain and dissipation $V_i - \hbar\gamma/2 = 0$, which gives $P_{0,th} = \gamma\Gamma_X/R$. For inhomogeneous pump spots, the threshold power is larger due to additional planar losses of waves from the spatially finite-gain region.

4.3.2 Numerical results on reservoir lensing

Consider two separate pumps $P(\boldsymbol{r}_\parallel) = P_S(\boldsymbol{r}_\parallel) + P_L(\boldsymbol{r}_\parallel)$, of characteristic sizes D_S and D_L, which are referred to as the *source* and the *lens* as introduced in section 4.2 and depicted in Fig. 4.1. Denote the complex-valued potential coefficients for the source

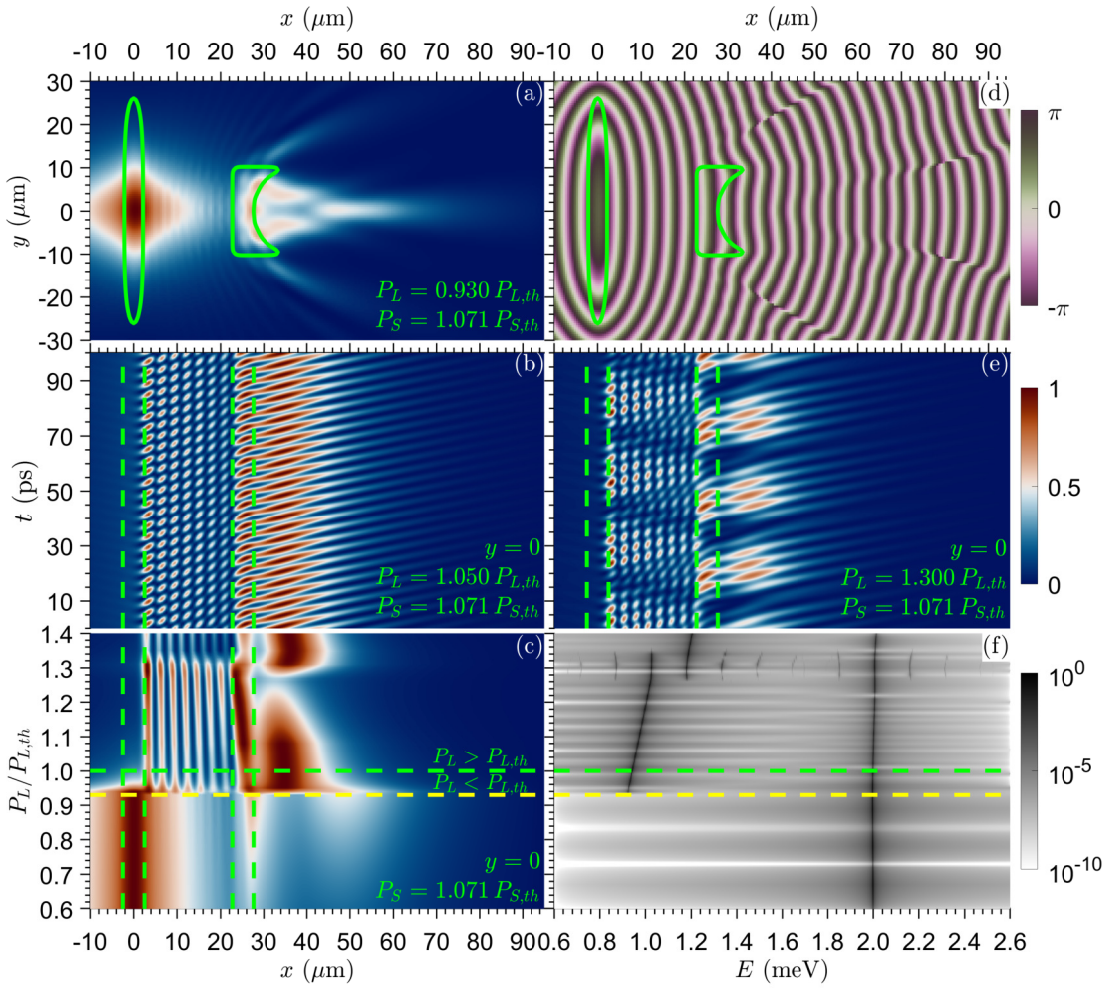

FIGURE 4.4: (a) Normalized density $|\Psi|^2$ and (d) phase map $\arg(\Psi)$ of the condensate in the steady state under nonresonant pumping. (b),(e) Time-resolved density line profile along $y = 0$ for two different pump powers. (c) Time-integrated density line profile, and (f) corresponding spectral weight for varying lens power. Data are normalized at each step in $P_L/P_{L,th}$. The FWHM of the pump profiles is outlined with green solid lines. The green vertical dashed lines indicate the outer and inner boundaries of the source and lens at $y = 0$. The horizontal green dashed line indicates the threshold of the isolated lens. The horizontal yellow dashed line indicates the onset of periodic dynamics characterized by more than one spectral peak.

and lens potentials by $V_S = V_{r,S} + iV_{i,S}$ and $V_L = V_{r,L} + iV_{i,L}$, respectively. Conservation of energy tells us that polaritons generated at the source will obtain kinetic energy following:

$$V_{r,S} = 2\frac{\hbar^2\pi^2}{m^*\lambda^2}. \tag{4.21}$$

Let us list some requirements in order to obtain steady-state lensing of polariton waves with wavelength λ coming from the source and passing through the lens:

(i) $D_L > \lambda$, the lens has to be large enough to refract the incident waves.

(ii) $0 < V_{r,S} - V_{r,L} = \Delta$, waves must be propagating in the lens.

(iii) $P_L < P_{L,\text{th}}$, the lens should be below the threshold.

(iv) $P_S > P_{S,\text{th}}$, the source must be above the threshold.

Here, $P_{S(L),\text{th}}$ are the threshold powers of the isolated source (lens) pumps.

One can rewrite requirements (i) and (ii) in terms of the model parameters, respectively,

$$D_L > \hbar\pi\sqrt{\frac{2\Gamma_X}{m^* P_{0,S} G(1+\eta)}} = \lambda, \tag{4.22}$$

$$0 < \frac{P_{0,S} - P_{0,L}}{\Gamma_X} G(1+\eta) = \Delta. \tag{4.23}$$

Here, $P_{0,S(L)}$ denotes the power density of the nonresonant source (lens) pump. Therefore, it becomes evident that increasing $P_{0,S}$ will satisfy both requirements. However, Δ needs to be reasonably bounded to obtain good focusing of transmitted waves. This is evident from the variable maximum intensity in the focal region in Fig. 4.2(c). Therefore, arbitrarily increasing $P_{0,S}$ does not guarantee good focusing of polariton waves. Also, notice that requirement (iii) is not strict, as we will see later.

The reservoir lensing scheme in Fig. 4.4 is demonstrated by numerically solving the generalized Gross-Pitaevskii and reservoir model. Set the profile of the source pump to be cigar-shaped to generate plane waves approximately

$$f_S(\boldsymbol{r}_\parallel) = \exp\left[-\frac{x^2}{2\sigma_x^2} - \frac{y^2}{2\sigma_y^2}\right] \tag{4.24}$$

in which $\sigma_x \ll \sigma_y$. The lens is taken to be planoconcave shaped with $R = 10.0\,\mu$m and $T_N = 4.5\,\mu$m. The FWHM of the source and lens are outlined with solid green curves in Figs. 4.4(a) and 4.4(d). It is worth noting that their threshold powers are different because of the different profiles of the source and the lens.

One of the main differences between the resonant scheme discussed in section 4.2 and the current nonresonant scheme is the vivid localization of the source condensate along the vertical direction shown in Fig. 4.4(a). This effect stems from the anisotropic gain region that favors modes with minimal losses, and effective attractive interactions between the condensate and the reservoir due to the gain-saturation mechanism [90]. However, the enhancement of propagating waves in the focal region can be clearly observed in Fig. 4.4(a), partly due to amplification from the lens gain. The phase map shown in Fig. 4.4(d) is very different from that in Fig. 4.2(d), which arises from the large detuning between the source waves and the lens potential in simulation, i.e., $\Delta = V_{r,S} - V_{r,L} \approx 2.0\,\text{meV} - 0.8\,\text{meV} = 1.2\,\text{meV}$. To reduce detuning Δ and achieve

stronger focusing, the lens could be pumped harder. However, this triggers condensation inside the lens, and requirement (iii) is violated. Moreover, reinforcing “ballistic" interactions between the source and the lens region have lowered the lens threshold [91, 92] (yellow dashed line in Fig. 4.4). These complex wave dynamics make it therefore a nontrivial task to arbitrarily adjust the detuning Δ to obtain stronger focusing while—at the same time—keeping the lens pump below the threshold.

If, on the other hand, requirement (iii) is relaxed and the lens power is made variable, then interesting nonlinear physics becomes enhanced. Figure 4.4(c) shows the time-integrated line profile of the wavefunction density at $y = 0$ for varying lens power P_L, and the corresponding energy spectrum in Fig. 4.4(f). As discussed at the beginning of the section, the system favors a steady-state behavior when P_L is small, characterized by a single clear spectral line in Fig. 4.4(f). In this regime, the results are similar to those of a static lens potential impinged by resonantly excited waves discussed in section 4.2. However, as the lens power increases, an additional spectral line appears and non-stationary periodic solutions form as a result of intricate interactions between the condensate polaritons generated at the source and the lens, in agreement with experiments [93, 94]. It is worth mentioning that such solutions are also captured in a density matrix treatment [95]. An example of two such solutions in the time domain is shown in Figs. 4.4(b) and 4.4(e). Clear ≈ 252 GHz intensity beatings in the focal region can be observed in Fig. 4.4(b) whereas Fig. 4.4(e) shows two dominant beat frequencies.

4.4 Reservoir lenses above threshold

There are limitations to the source and lens scheme in the previous section, which cannot be quantified nicely, given the complex wave dynamics at play. Firstly, reinforcing behavior between the source and lens regions results in lowered threshold gain of the interacting system, which can lead to condensation into extended quasinormal standing wave modes supported by both the source and the lens region. This is a general feature of interacting dissipative systems, such as coupled lasers or interacting polariton condensates [91, 92]. Second, the source pump size would, in general, need to be larger than the lens in order to avoid Δ becoming too large (that is, smaller source pumps need to be driven with higher power and thus emit waves with higher energy). This can lead to thermally induced self-trapping of the source condensate [96].

To overcome these issues, a more simple case is considered, in which the source pump $P_S(\boldsymbol{r}_\parallel) = 0$ is omitted and only the lens $P_L(\boldsymbol{r}_\parallel)$ is driven above the threshold. Indeed, the lens region then plays the role of a carefully designed anisotropic planar emitter from which waves radiate to interfere constructively. Figures 4.5 and 4.6 present the steady condensate state for pump profiles shaped, respectively, into a planoconcave lens and a double concave lens and driven above the threshold. Polariton waves generated in

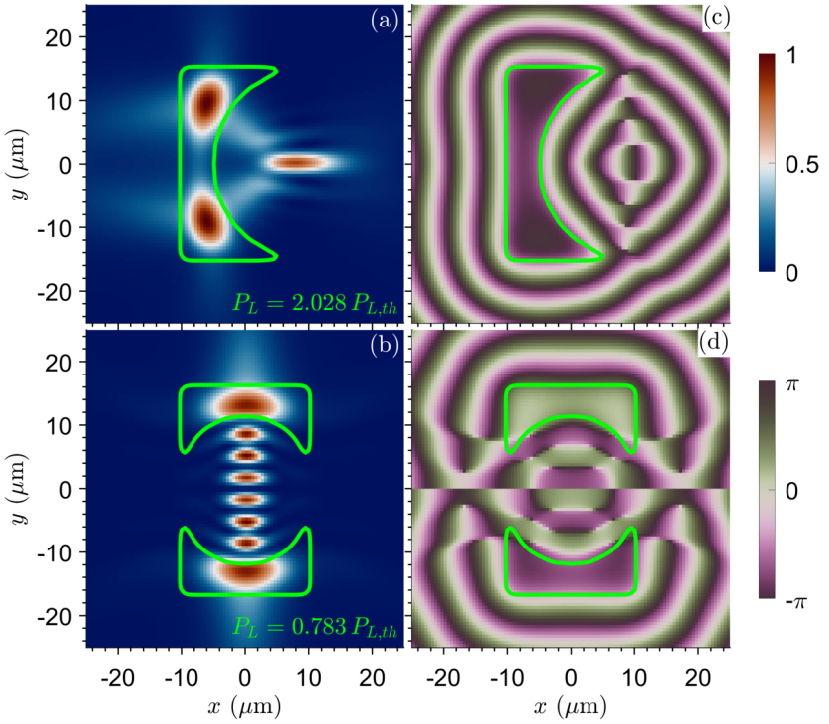

FIGURE 4.5: (a),(b) Steady-state condensate density $|\Psi|^2$ and (c),(d) phase $\arg(\Psi)$ for two different nonresonant pump configurations. The nonresonant pump is shaped into a (a) planoconcave lens showing clear focusing of the emitted waves outside the pumping area, and a (b) planoconcave resonator made from two lenses (emitter) facing each other. Note that each lens is below the threshold, but the system/resonator as a whole has a lower threshold and thus supports a standing wave condensate at lower powers. The FWHM of the pump profiles is outlined in green.

the pump region propagate along the direction normal to the lens surface and form a strong focal region with a clear phase shift.

When the "lens" power is increased, then the contrast between the condensate density within and outside the lens region increases, as shown in Figs. 4.7(a) and 4.7(b) for the planoconcave lens and Figs. 4.8(a) and 4.8(b) for the double concave lens. For single pump configurations, the condensate density line profile along the lens axis is plotted[1]. These results underpin the potential of using anisotropic-shaped nonresonant excitation beams to generate high-density polariton condensates spatially separated from any influence of the background exciton reservoir, such as strong dephasing or spatial hole burning effects.

Moreover, the potential for designing planar resonators by setting two identical lens-shaped pump profiles facing each other [see Figs. 4.5(b), 4.5(d), 4.6(b), and 4.6(d)]

[1]Note that states of spontaneously broken time-reversal symmetry $|\Psi(k_x,k_y)| \neq |\Psi(k_x,-k_y)|$ arise more often when driving the condensate far above threshold [91]. These states are suppressed when the role of the static potential term in Eq. (4.14) is enhanced. Therefore, in Figs. 4.7 and 4.8 we set $\eta = 5 \rightarrow 180$ and, to keep the ratio V_r/V_i in Eqs. (4.19) and (4.20) fixed, we also change $\hbar R = 2.8g \rightarrow 84.2g$. This has only minor quantitative effects on the results and aids in the simulation convergence to symmetric states

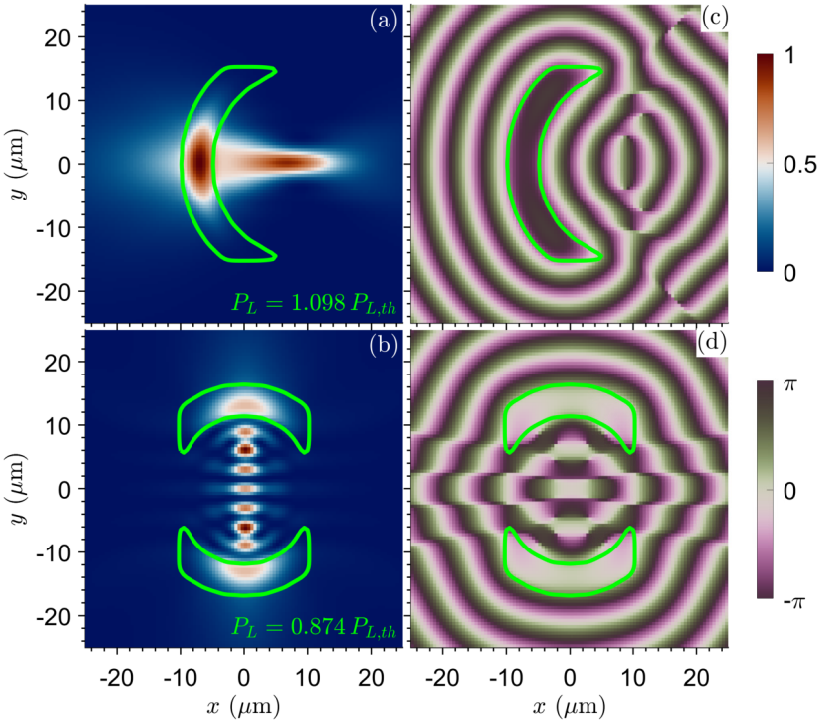

FIGURE 4.6: (Left column) Condensate density $|\Psi|^2$ and (Right column) phase $\arg(\Psi)$ in the steady state. The nonresonant pump is shaped into a (a) positive meniscus lens showing clear focusing of the emitted planar waves outside the pumping area and a (b) positive meniscus resonator made from two lenses facing each other. Note that each individual lens is below the threshold, but the system/resonator as a whole has a lower threshold and thus supports a standing-wave condensate at lower powers. The FWHM of the pump profiles is outlined in green.

is investigated. A clear standing condensate wave forms, strongly localized along the horizontal direction. The mode number of this planar standing wave can easily be adjusted by changing the distance between two lenses or their pump power [94]. Moreover, the pump polarization of each pump lens can also be adjusted to design standing condensate waves with intricate polarization patterns [97]. These results open a pathway for the generation of structured, high-density, polariton condensates spatially separated from the direct influence of the reservoir by simply adjusting the geometric configuration and the excitation power of the nonresonant pump.

Compared with the configurations of both lenses shown in Figs 4.7 and 4.8, the even stronger localization and higher density of the condensate outside the pump region are observed for a double concave lens (positive meniscus lens). However, compared to the results in the linear regime shown in section 4.2, the enhanced scattering of the incident plane wavefront onto the positive meniscus is observed, resulting in poorer focused transmission. This result is in contrast to the case presented in Fig. 4.8 where a positive meniscus emitter focuses waves more efficiently than a planoconcave lens.

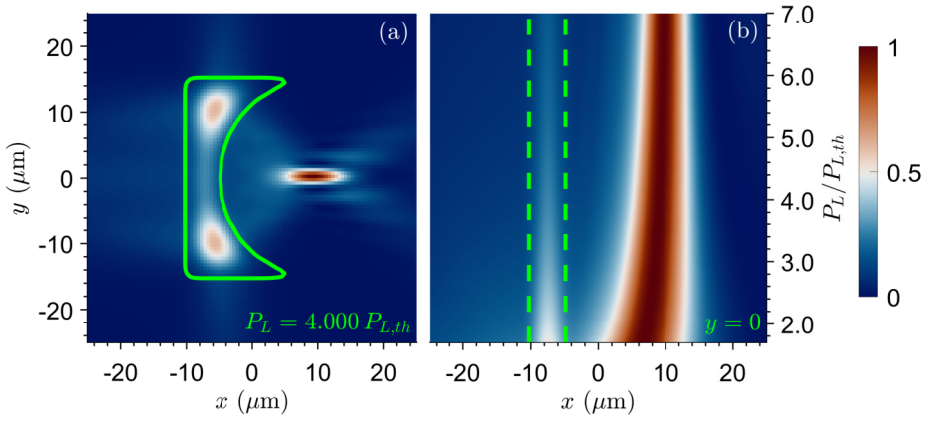

FIGURE 4.7: (a) Condensate density for a planoconcave-shaped nonresonant pump at high powers and (b) line profile along $y = 0$ for varying power. The vertical green dashed lines indicate the pumped region.

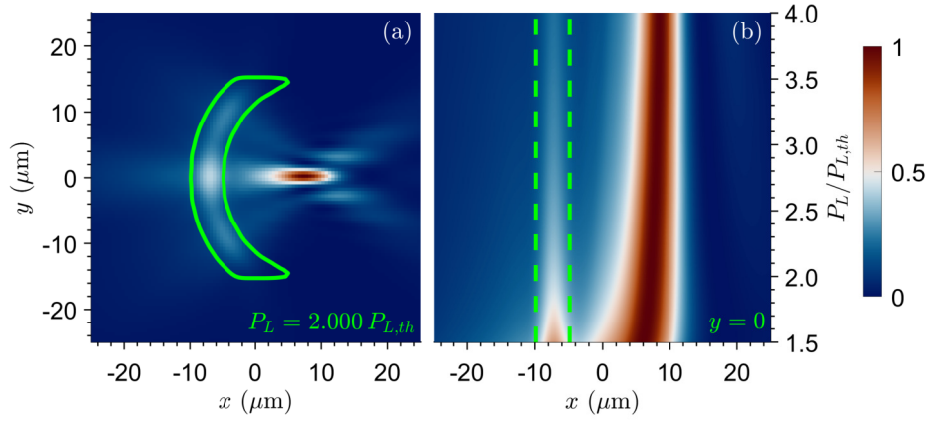

FIGURE 4.8: (a) Condensate density for a double-concave-shaped nonresonant pump at high powers and (b) line profile along $y = 0$ for varying power. The vertical green dashed lines indicate the pumped region.

4.5 Conclusions

This chapter demonstrates how a pumped planoconcave lens can strongly focus polariton condensate wavelets. These wavelets may either impinge on the lens or be generated internally when the lens is driven above the threshold. Furthermore, it shows that the nonresonant nature of these lenses can lead to tunable, high-contrast, condensate density oscillations at the focal point, reaching frequencies as high as 250 GHz. From an application perspective, such pumped lens elements might offer a building block in generating a directional flow of optical information and focused high-density polariton condensates with large nonlinear energy scales, which form an essential ingredient in

any information processing scheme. The all-optical aspect is, then, particularly exciting when considering circuitry whose elements can be easily reprogrammed.

In summary, this chapter theoretically investigates all-optical planar microlensing techniques applied to exciton-polariton condensates. The lenses are created using spatially patterned nonresonant excitation profiles that provide both gain and blueshift to the polariton modes. It is worth mentioning that the scheme studied in this chapter should not be confused with that of resonant control [98, 99] where auxiliary “condensates" are directly injected to provide spatially patterned polariton blueshift.

In this chapter, the condensate dynamics within a source-and-lens pump setup (as shown in Fig. 4.1) is first studied. A comparison of the rich nonlinear dynamics with that of linear Schrödinger wave mechanics is provided. Scanning across pump power parameters, we demonstrate that a departure of the steady condensate state, resembling the linear Schrödinger dynamics, into a stable limit cycle state characterized by multiple spectral peaks and rapid ($\approx$ 252 GHz) density oscillations in the focal region. This result holds promise for polaritonic clock generators in integrated circuits [100]. Next, we study the condensate behavior within a simpler setup, one that consists of a single lens-shaped pump driven above threshold. This results in highly anisotropic condensate emission and a strong focusing of condensate waves outside the pump region. This opens possibilities in generating polariton condensates that are separated from detrimental reservoir dephasing effects and might obtain unprecedented coherence times, favorable for highly sensitive planar matter-wave interferometers [74].

The possible reservoir devices and their applications are not limited to the examples shown in this chapter. It is worth mentioning that the microlensing experiment with similar configuration shown in Figs. 4.5(a) has been carried out after the theoretical prediction described here [101]. The potential of this work to stimulate future theoretical and experimental applications of reservoir optics in polariton condensates is promising. For example, one might add such planar lenses at the apertures of pumped waveguides considered in [79] or even at the end of a staircase potential such as in [81], to collect polariton waves and prevent diffraction and signal losses in future polaritonic circuitry. Indeed, the anisotropic shape of the lenses and their ability to focus (concentrate) polariton condensates put them in a unique position to operate as nonlinear directional elements for information processing in the same spirit as planar optical transistors. The findings in this chapter are also relevant to atomtronics [102, 103] where arbitrary all-optical control over the atom’s potential landscape is possible [104].

4.6 Disclaimer

Y. Wang performed the numerical simulation and all authors of [105] contributed to the analysis of the simulation results. The theoretical modeling was developed by Y. Wang

and H. Sigurdsson. The content, including text and figures, presented in this chapter is adapted from the paper:
Y. Wang, H. Sigurdsson, J. D. Töpfer, and P. G. Lagoudakis, *Reservoir optics with exciton-polariton condensates*, Physical Review B **104**, 235306 (2021) [105].

Chapter 5

Enhanced coupling between ballistic polariton condensates through tailored pumping

5.1 Introduction

There has been a tremendous effort dedicated to scaling up the number of coupled polariton condensates to form extended systems. The notable candidates for large-scale networks and lattices of polariton condensates are etched micropillar arrays [106, 107], metal-deposited cavity surface [108], etch-and-overgrowth techniques [109, 110], surface acoustic waves [111], and structured nonresonant light source using spatial light modulators [112, 113]. On the one hand, designing lattices of polariton condensates can offer new insight into the non-Hermitian physics of driven-dissipative quantum fluids obeying Bloch's theorem with strong nonlinearities [114]. On the other hand, the large state space and strong nonlinearities of a coupled polariton condensate network could offer a platform for classical or even quantum computing protocols [115] given the ease of optical write-in and read-out of polaritons (being part photonic) [116]. A common challenge in the design of extended polariton condensate systems is to establish internode coupling that is strong enough to overcome the detrimental effects of disorder and noise, which would otherwise diminish the system's coherence.

This chapter proposes an all-optical method to enhance spatial coupling and coherence between nonresonantly driven ballistic polariton condensates [94]. To achieve this, tailored pump spots with reduced rotational C_n symmetry, which generate, refract, and focus high-momentum condensate polariton waves between nearest neighbors, are numerically modeled. This can be easily achieved in practice using liquid crystal spatial light modulators [81]. As a case study, the idea is made by numerically solving the

generalized stochastic GPE (see section 2.3.3.2) for a honeycomb lattice tiled with triangular pump spots (C_3) in comparison to more conventional cylindrically symmetric Gaussian spots. Similar structures have been exploited in photonic crystal slabs to generate band gaps [117] but have not been widely explored in the context of polariton fluids. The method presented in this chapter can be applied to optically driven lattices of polariton condensates, which have currently reached the capacity of hundreds of coherently coupled condensates [113]. The results could also advance the performance of polariton platforms to explore XY spin materials [20, 118], topological physics [23, 24], vorticity [112, 119], and band structure engineering [120, 121].

5.2 Anisotropic pump shapes for polariton condensation

Recall the 2D GPE coupled to a driven exciton reservoir defined in chapter 2 from Eqs. (5.1) and (2.64),

$$\begin{aligned} i\hbar\frac{\partial}{\partial t}\Psi(t,\boldsymbol{r}_\parallel) &= \Big\{-\frac{\hbar^2}{2m^*}\nabla_\parallel^2+\alpha|\Psi(t,\boldsymbol{r}_\parallel)|^2+G\Big[n_X(t,\boldsymbol{r}_\parallel)+\frac{\eta}{\Gamma_X}P(\boldsymbol{r}_\parallel)\Big] \\ &\quad +i\frac{\hbar}{2}\big[Rn_X(t,\boldsymbol{r}_\parallel)-\gamma\big]\Big\}\Psi(t,\boldsymbol{r}_\parallel), \qquad (5.1) \\ \frac{\partial}{\partial t}n_X(t,\boldsymbol{r}_\parallel) &= -\big[\Gamma_X+R|\Psi(t,\boldsymbol{r}_\parallel)|^2\big]n_X(t,\boldsymbol{r}_\parallel)+P(\boldsymbol{r}_\parallel). \qquad (5.2) \end{aligned}$$

Set the parameters similar to our previous works based on slightly negatively detuned cavities with InGaAs quantum wells: $m^* = 0.28\,\mathrm{meV\,ps^2\,\mu m^{-2}}$, $|\chi|^2 = 0.4$, $g = 1\,\mu\mathrm{eV\,\mu m^2}$, $\hbar R = 2.0g$, $\eta = 2$, and $\gamma^{-1} = \Gamma_X^{-1} = 5.5\,\mathrm{ps}$. The nonresonant pump is written $P(\boldsymbol{r}_\parallel) = P_0 f(\boldsymbol{r}_\parallel)$ where P_0 is the power density multiplied by a spatial profile that satisfies $\max(f) = 1$.

5.3 Shaping the polariton outflow

The numerical results of steady-state solutions of Eq. (5.1) using pump profiles $f(\boldsymbol{r}_\parallel)$ tailored to guide polariton waves into desired patterns will be analyzed in this section. The reason why the guidance of the waves can work is that a local pumping region (i.e., spot) produces a co-localized complex potential landscape felt by the generated polaritons. In the low-density regime (see section 2.3.3.1), this potential is written as,

$$V(\boldsymbol{r}_\parallel) = \frac{P(\boldsymbol{r}_\parallel)}{\Gamma_X}\left[(1+\eta)G+i\hbar\frac{R}{2}\right]. \qquad (5.3)$$

From the above equation one can appreciate two things:

(i) The real part is positive because excitons interact repulsively ($G > 0$) which means that polaritons are blueshifted at the spot location.

(ii) The imaginary part is also positive, which means that above a certain critical power $P_0 = P_{\text{th}}$ the condensation threshold is reached (stimulation exceeds losses) and coherent polaritons are amplified at the spot location until the reservoir clamps and the condensate stabilizes.

For small pumping spots, the resulting steady state is a *ballistic condensate* [12, 122] shown in Fig. 5.1. For cylindrically symmetric spots [see Figs. 5.1(a) to 5.1(c)], the real space condensate density is co-localized with the spot and coherent polariton waves are radially emitted in all directions with high momentum, as evidenced from the sharp density ring in momentum-space. When multiple small spots are pumped and displaced from each other, fascinating phenomena such as spontaneous synchronization and multimodal emission can occur due to the complex non-Hermitian coupling between neighboring condensates [17, 94, 113, 121]. The condensate coupling is mediated by propagating polariton waves in the plane of the cavity (near field) and should not be confused with out-of-plane coupling like in the far field of laser arrays [123].

However, if the pump spot is not cylindrically symmetric, then the generated polariton waves will experience refraction and interference, giving rise to anisotropic streams of condensate polaritons, as shown in Figs. 5.1(d)–5.1(f) for a triangular spot. Such a shaping of the pump spot can be realized using spatial light modulators in the incident excitation, which allows focusing almost arbitrary excitation patterns into the microcavity plane [81]. This has enabled the demonstration of all-optical in-plane polariton waveguides [79, 80], transistor switches [85, 86], amplification [15, 16], tailored momentum distribution [81], and microlensing [105]. Notice how the triangular-shaped condensate in Fig. 5.1(e) rotates by $\pi/3$ with respect to its pump pattern in Fig. 5.1(d). This can be understood from the following consideration. Inside the pump spot, low-momentum polariton waves ($k \sim 0$) are amplified and subsequently dispersed, flowing out of the pump spot and elastically converting their (pump-induced) potential energy into kinetic energy. The waves that hit the edges of the triangle close to normal incidence scatter very little, whereas polaritons hitting the corners of the triangle are at an oblique incidence and scatter more strongly. This leads to enhanced flow of condensate particles along the normals of triangle edges, effectively forming the dual pattern of the pump (i.e., pump edges map to condensate corners). The same holds for higher-order polygonal-shaped pump spots. This interpretation can be easily verified by solving an initial value problem of a two-dimensional Schrödinger equation wherein a Gaussian wave packet centered at $k = 0$ and $\boldsymbol{r}_{\parallel} = 0$ in momentum and real space is propagated in time. The following will show that shaping multiple spots into triangles, as opposed to the conventional Gaussian-shaped spots, focuses and enhances the interaction between adjacent condensates, resulting in lowered threshold and increased coherence in the extended polariton system.

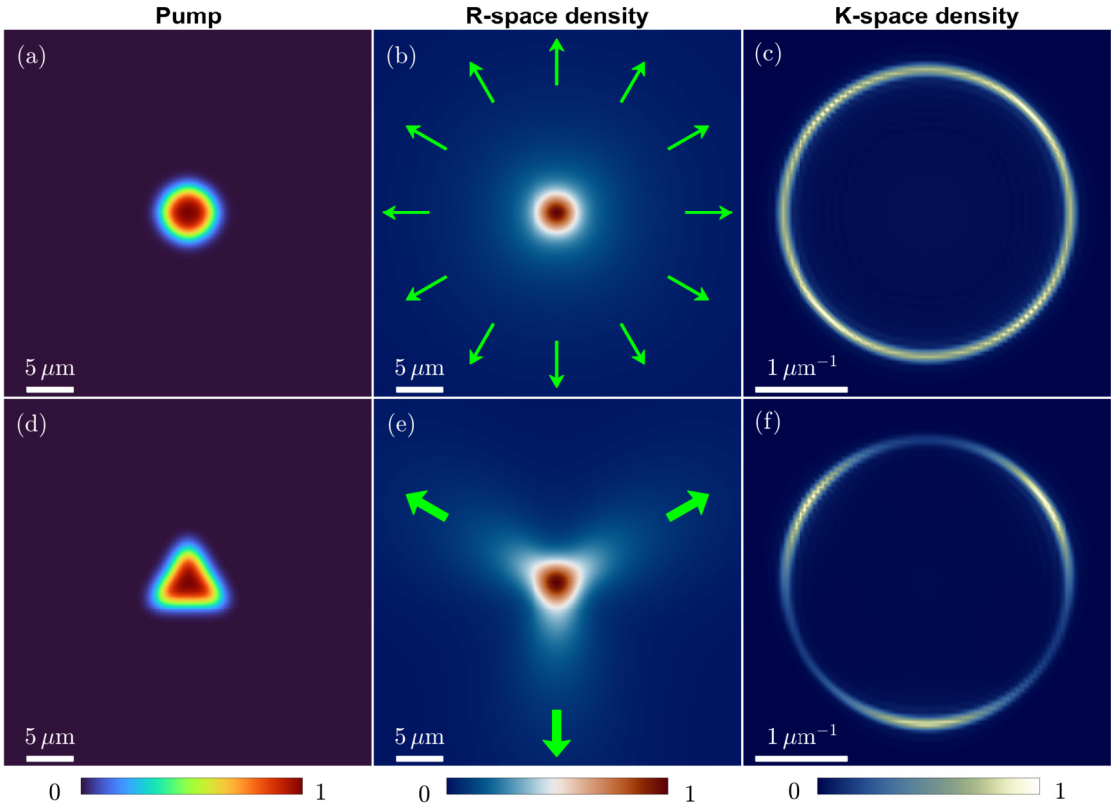

FIGURE 5.1: (a),(d) Circular and triangular pump configurations and corresponding normalized condensate steady-state solutions $|\Psi|^2$ in (b),(e) real space and in (c),(f) momentum space. The green arrows in (b) illustrate the condensate flow emitted in all directions, and in (e), the thicker green arrows show the anisotropic and concentrated condensate flow. Notice how the triangular-shaped condensate in (e) is rotated by $\pi/3$ with respect to the pump in (d).

Since different pump profiles usually have different condensation threshold power densities, the triangular spot needs to be calibrated against the circular (Gaussian) spot so that they share the same threshold power density $P_{\text{th},T} = P_{\text{th},C}$. Under this condition, polaritons experience the same blueshift at their respective spots, and thus populate momentum components of similar magnitude in Fourier space [compare Fig. 5.1(e) with 5.1(f)] enabling a more fair comparison. This calibration is achieved by fixing the parameters of the model (5.1) and adjusting the side length of the triangle until $P_{\text{th},T} = P_{\text{th},C}$ for a given full-width-at-half-maximum of the circular spot.

After calibrating the system, the anisotropy of the ballistic flow from the steady condensate state by integrating the particle density $N = \int |\Psi|^2 d\boldsymbol{r}_{\parallel}$ over two segmented regions, denoted N_A and N_B, shown schematically in Figs. 5.2(a) and 5.2(b) for varying curvature $\kappa = 1/R$ of the triangle spot sides, is quantified. For the circular pump, the curvature satisfies $\kappa R_0 = 1$ where R_0 is its radius, whereas for the circumscribed triangle $\kappa = 0$ [see Fig. 5.2(c)]. For a cylindrically symmetric spot, the ratio is $N_A/N_B = 1$

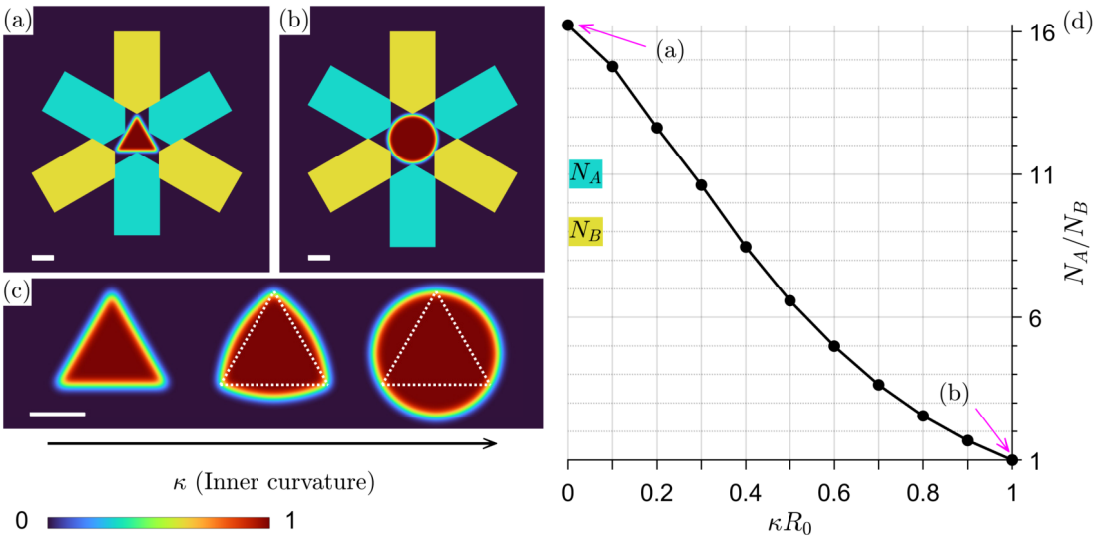

FIGURE 5.2: (a),(b) Triangular and circular pump profiles (red color) with overlaid schematic blue and yellow integration areas to determine the amount of condensate anisotropy in the system. (c) Example of pump profiles with zero, intermediate, and maximal inner curvature denoted $\kappa = 1/R$. The white dotted line indicates the circumscribed triangle. (d) The ratio of condensate particles (integrated density) between the blue and yellow areas N_A/N_B to vary the curvature for a fixed power density above the threshold. The white bar in (a)–(c) is 10 μm and the radius of the circular pump is $R_0 = 11.5\,\mu$m.

[see Fig. 5.2(d)] as expected since the steady condensate state also becomes cylindrically symmetric. Approaching the equilateral triangle shape, $\kappa \to 0$, the ratio increases dramatically to almost $N_A/N_B \approx 16$, underlining the strong focusing of the ballistic polariton outflow from the sides of the triangular pump spots.

The coupling strength between adjacent condensates pumped with triangular spots of different relative orientations is characterized. Four distinct hexagonal pumping patterns [Figs. 5.3(a)–5.3(d)] and their corresponding condensate densities $|\Psi|^2$ at $P_0 = 1.1P_{\text{th}}$ [Figs. 5.3(e)–5.3(h)] are considered here. The first three patterns can be categorized as side-side-, side-vertex-, and vertex-vertex-facing triangles. In Fig. 5.3(i), it is shown that the condensate population $N = \int |\Psi|^2 \, d\boldsymbol{r}_{\|}$ when scanning the pumping power density in time (linearly) while numerically integrating Eq. (5.1). The results show that the lowest threshold belongs to the side-side-facing pattern in Fig. 5.3(a), while the highest threshold belongs to the vertex-vertex-facing pattern in Fig. 5.3(c). This result intuitively makes sense because the polariton outflow is strongest from the sides of the triangular pump spots, which enhances the overlap and coupling between neighbors, and weakest from the vertices, in agreement with the results from Figs. 5.1 and 5.2.

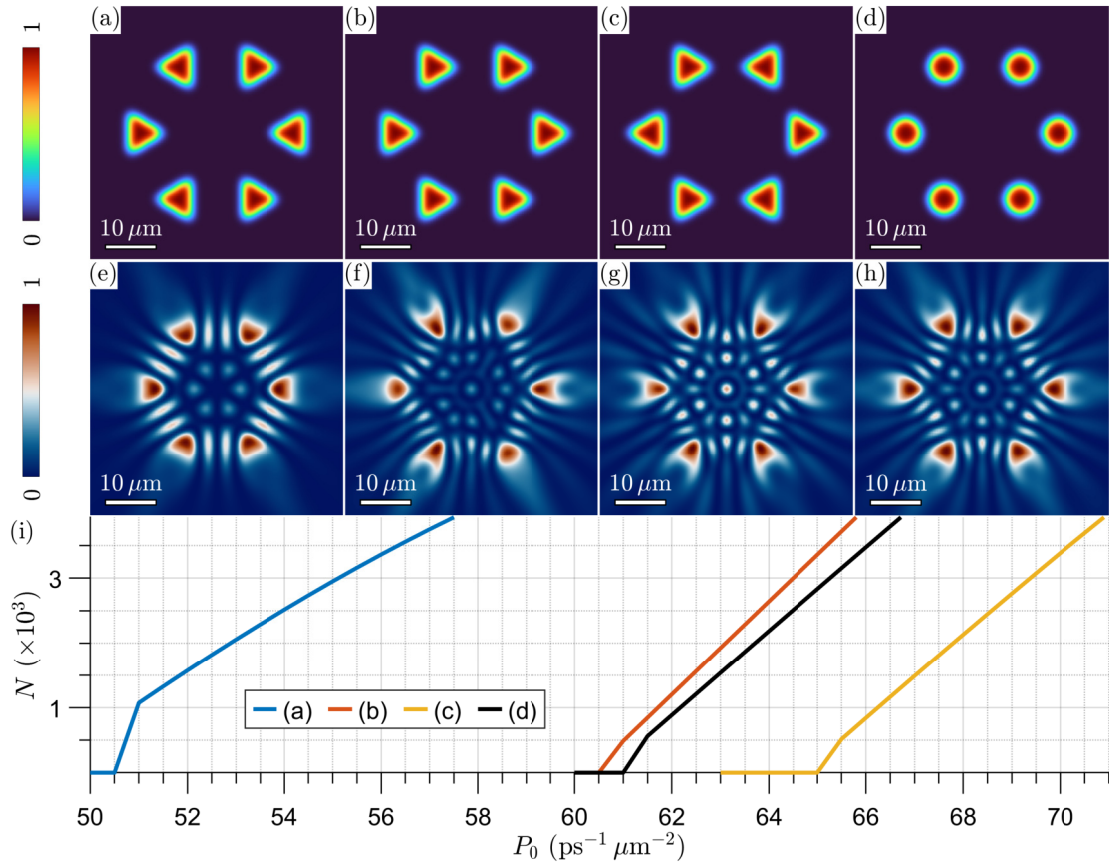

FIGURE 5.3: Pump profiles structured into a hexagon with different relative orientations of the triangular spots: (a) side-side-, (b) side-vertex-, and (c) vertex-vertex-facing nearest neighbors. (d) A reference hexagon of circular spots. (e)–(h) Corresponding normalized condensate densities at $P_0 = 1.1P_{\text{th}}$. (i) Corresponding number of condensate particles for increasing power density marking the different condensation thresholds for each configuration.

5.4 Spatial coherence enhancement

The enhanced coupling between side-side facing triangular pump spots shown in Fig. 5.3 implies stronger spatial coherence in an extended system of polariton condensates, which is an essential property to study large-scale emergent phenomena such as macroscopic vorticity [119], universal behaviors and Kibble-Zurek scaling [124], and simulation of spin systems [20, 118]. Here, we demonstrate this enhancement of the condensate coherence length by tiling a large honeycomb lattice of side-side facing triangular pump spots like in Fig. 5.3(a). The resulting condensate solution is shown in Fig. 5.4(a).

In order to calculate the mutual coherence between any two spatial locations of the condensate in the lattice, the SGPE in the truncated Wigner approximation [42], discussed in section 2.3.3.2. Here, a complex white noise operator $i\hbar dW/dt$ is appended

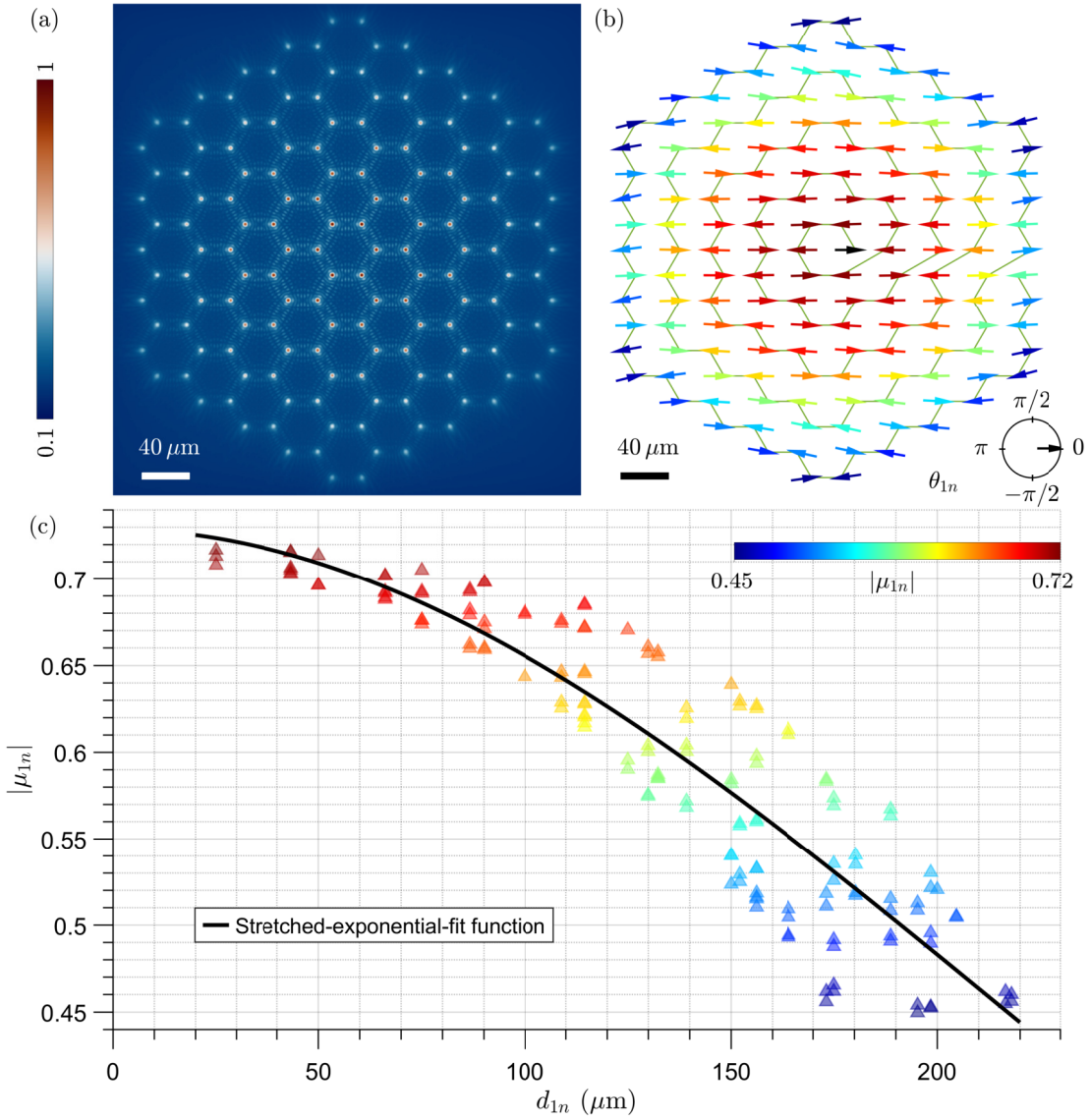

FIGURE 5.4: (a) Normalized time-integrated condensate density $\langle|\Psi|^2\rangle$ for triangular pump spots arranged into a honeycomb lattice. (b) Corresponding extracted mutual complex coherence function μ_{1n}. The color scale and the orientation of the arrows depict the magnitude $|\mu_{1n}|$ and the phase θ_{1n}, respectively. The central black arrow indicates the reference spot with zero phase. (c) The modulus of the coherence function as a function of the absolute distance between the first and n-th spots $|\boldsymbol{r}_{\parallel 1} - \boldsymbol{r}_{\parallel n}| = d_{1n}$. The black line is a fit of the stretched exponential function 5.9 which gives effective coherence length of $L_{\mathrm{coh}} = 279.3\,\mu$m.

to Eq. (5.1) representing small random fluctuations added at every time step with correlators satisfying,

$$\langle dW_i dW_j \rangle = 0, \tag{5.4}$$

$$\langle dW_i^* dW_j \rangle = \frac{\gamma + R n_X}{2\Delta A} dt \delta_{i,j}. \tag{5.5}$$

Here, i and j refer to different spatial grid points in the numerical simulation, and

$\Delta A = \Delta x \Delta y$ is the area of the grid cells. The validation in using Eq. (5.5) is checked in section 2.3.3.2 of chapter 2.

The spatial coherence across the lattice is quantified using the normalized complex first-order coherence function (sometimes denoted as $g^{(1)}$) between each pair of condensates written,

$$\mu_{nm} = \frac{\langle \psi_n^* \psi_m \rangle}{\sqrt{\langle \psi_m^* \psi_m \rangle \langle \psi_n^* \psi_n \rangle}}, \quad n, m = 1, 2, \ldots \tag{5.6}$$

where $\psi_n(t) = \Psi(\boldsymbol{r}_{\parallel n}, t)$ is the phase and amplitude of the nth condensate at the center of their respective pump spot location $\boldsymbol{r}_n$. The time average is defined as $\langle \psi_m^* \psi_n \rangle = \frac{1}{T_\mu} \int_{T_\mu} \psi_m^* \psi_n \, dt$ where T_μ is the duration of the simulation that is taken to be much greater than any other characteristic timescale in the model parameters. It is worth noting that in the experiment the mutual coherence function can be measured through multislit interferometry [113]. The modulus of the first-order coherence function $|\mu_{nm}| \leqslant 1$ serves as a normalized measure of coherence between any two condensates in the lattice, whereas its argument represents their average phase difference

$$\theta_{nm} = \arg(\mu_{nm}). \tag{5.7}$$

Fig. 5.4(a) shows an example condensate time-integrated density for a finite-sized honeycomb lattice of side-side facing triangular spots at a given lattice constant and pump power. Clear interference fringes can be seen between the pumped condensate bright spots, implying robust synchronization even in the presence of noise. Closer to the edge of the lattice transverse losses due to the strong polariton outflow are more effective, which results in weakened edge density.

In Fig. 5.4(b) the arrows denote the phase θ_{1n} between all pairs of condensates with respect to the central one (denoted with a black arrow) with a colorscale representing the coherence amplitude $|\mu_{1n}|$. As expected, the coherence drops radially due to the decreased coupling between distant neighbors. Note that the arrows have arranged themselves antiparallel with respect to nearest neighbors, implying anti-phase (π) synchronization between the condensates for the given lattice parameters. Other lattice parameters can result in a condensate solution characterized by in-phase synchronization between the lattice nodes [94]. In either case, the conclusions remain the same. We also point out the slight twist in the angle of the arrows at the edge of the lattice shown in Fig. **??**. This twist was recently observed in experiment [113] and is due to the polariton flowing out of the lattice, which corresponds to a phase gradient between the condensates.

Figure 5.4(c) shows the modulus of the coherence function $|\mu_{1n}|$ for increasing absolute distance between the central condensate node and the rest, $|\boldsymbol{r}_1 - \boldsymbol{r}_n| = d_{1n}$. One obtains

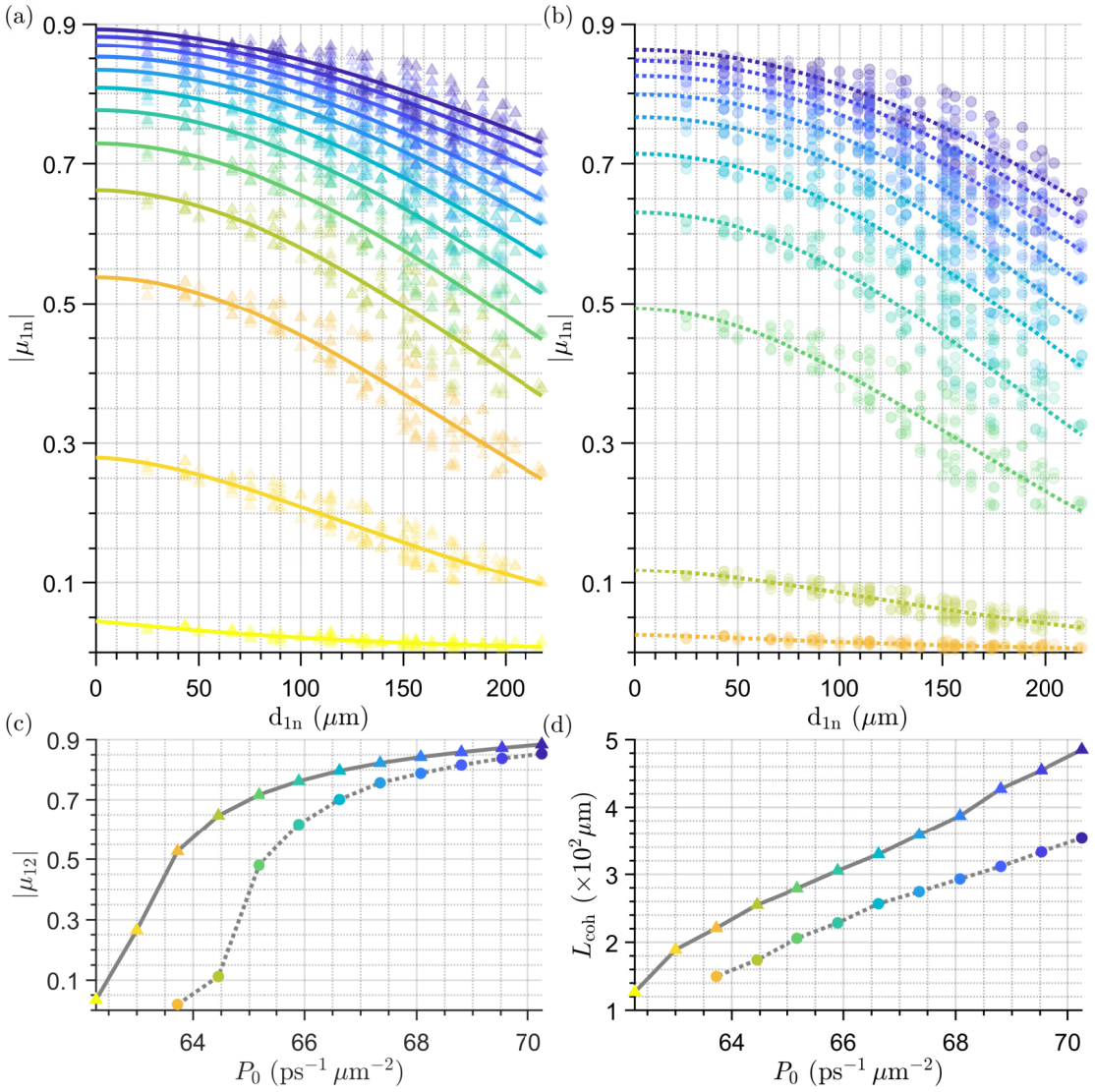

FIGURE 5.5: The modulus of the mutual coherence function $|\mu_{1n}|$ for increasing absolute condensate neighbor distance d_{1n} and different power densities (colors) for (a) triangular spots and (b) circular spots. Solid and dotted lines are fit using a stretched exponential function. (c) Corresponding power density scan of the mutual coherence between the first and second condensate $|\mu_{12}|$ for both configurations. (d) Corresponding effective coherence length extracted from the fitting for both configurations. The color of the markers directly corresponds to the values on the horizontal axis in (c).

good fit using a stretched exponential function [124] (black curve) written,

$$\mu(d) = Ae^{-(d/B)^C}, \quad d \geqslant 0. \tag{5.8}$$

Here, A, B, C are fitting parameters. Integrating $\mu(d)/A$ from $0 \rightarrow \infty$ we obtain an expression for the effective coherence length of the system [124],

$$L_{\text{coh}} = \frac{B}{C} \times \Gamma\left(C^{-1}\right), \tag{5.9}$$

where Γ is the gamma function. Equation (5.9) can be regarded as the spatial relaxation length of first-order correlations in the condensate.

Repeat the calculation for the triangle lattice from Fig. 5.4(c) but now for several different power densities collated into Fig. 5.5(a) in different colors. Yellow is the weakest power, and blue is the strongest. For comparison, the modulus of the coherence function for a lattice of circular spots is shown in Fig. 5.5(b). The comparison is more clearly visualized in Figs. 5.5(c) and 5.5(d) where only the coherence between the central nearest neighbor condensates $|\mu_{12}|$ and the effective coherence length L_{coh}, respectively, are plotted. The former [Fig. 5.5(c)] shows that the coherence of the condensate is stronger for the triangular pump spots across all powers, as expected. It also shows a sharp increase in both cases followed by a saturation that is similar to past observations [113, 125]. At even higher powers (not shown here), coherence starts to drop as the condensate becomes unstable and starts to fragment into multiple energy components [94]. This result underlines the enhanced spatial coupling between triangularly pumped condensate nodes as compared to circularly pumped nodes. Note that the amplitude of the noise for a given power density P_0 is the same for triangular and circular spots according to Eq. (5.5) since $n_X \propto P_0$. Therefore, the increased coherence for the triangular spots cannot be attributed to different levels of noise, as compared to the circular spots, but rather to the focused ballistic emission of polaritons between nearest neighbor condensate nodes in the lattice.

The latter [Fig. 5.5(d)] verifies that not only has the condensate coherence increased using triangular pump spots, but the relaxation of spatial correlations in the condensate lattice is much slower, implying longer coherence lengths than for the circular spots across all powers tested. On average, over all pump powers tested here, the improvement in coherence is $\approx 36\%$. A more exhaustive numerical study over the parameter space of the model will help to accurately quantify the improvement.

5.5 Conclusions

This chapter shows that by tailoring the shape of an incident nonresonant light source, which excites ballistic exciton-polariton condensates, it is possible to enhance the spatial coupling between separately pumped condensates. Compared to typical Gaussian spots, the reduced symmetry of the tailored pump spots refracts and focuses outflowing high-momentum polaritons from their pumped condensate centers. The coherent flow of polaritons can be directed towards their nearest neighbors, thereby enhancing the condensate's spatial coupling. In this chapter, the method of numerically solving the stochastic generalized Gross-Pitaevskii equation for a honeycomb lattice of triangular pump spots, which displays lowered threshold and larger effective coherence lengths as compared to a lattice of circular (cylindrically symmetric) pump spots, is

verified and can be applied to today's optical microcavities using standard spatial light modulator technology to generate macroscopic fluids of light with improved coherence scales. It can be used to help with exploration into complex long-range dynamics in dissipative quantum fluids, designing large-scale structured coherent light sources in the strong-coupling regime, and developing less noisy analog computing platforms based on polariton networks [115].

5.6 Disclaimer

The numerical simulation presented in this chapter was done by Y. Wang. The theoretical modeling was carried out by Y. Wang and H. Sigurdsson. The content, including text and figures, presented in this chapter is adapted from the paper:
Y. Wang, P. G. Lagoudakis, and H. Sigurdsson, *Enhanced coupling between ballistic exciton-polariton condensates through tailored pumping*, Physical Review B **106**, 245304 (2022) [126].

Chapter 6

Conclusions

The introduction, which describes polariton condensates and the tools for numerical simulation, is divided into two chapters. Chapter 2 provides the theoretical background, while chapter 3 discusses the tools for numerical simulation. Chapters 4 and 5 present numerical studies of the guidance and enhancement of the coherent exciton-polariton condensate outflow in both simple and intricate condensate dynamics driven by external-isometric nonresonant pumping. The summary, main findings, and future perspectives of the thesis are given as follows:

Chapter 2 introduces polariton condensates, starting from each component of the polariton system, namely QW excitons and microcavity photons, as well as the SC coupling between them, to the production of the polariton condensates and introduction of the 2D GPE. The materials, detuning, and dynamics of the DBRs and QWs used in this thesis are discussed as follows: Good and slightly negatively detuned microcavities with a long photon lifetime, and the AlGaAs-like QWs with Wannier–Mott excitons, produce nonzero momentum above the condensates threshold. Furthermore, the properties of the generalized 2D GPE coupled with the reservoir for pumping near the threshold in stationary conditions reveal that the spatial area of the pump profile, reservoir and condensates is similar. This explains why, in chapters 4 and 5, the expected tailored reservoir is possible by designing the external pump profile. As a tool to measure the coupling between internodes with complex white noise in the polariton lattices of chapter 5, the stochastic projection and the first-order spatial coherence are introduced, and validation of the truncated Wigner approximation, derived from the stochastic process, in the case of parameters chosen in this thesis, is checked.

Chapter 3 provides an SSFM-based with accuracy $\mathcal{O}(\Delta t^3)$ and CUDA-enabled 2D GPE solver. The main algorithms, such as parallel reduction, the core part of the SSFM, and time-integrated intensity and spatial coherence, are shown in pseudocode for clarity purposes. The computational methods not specifically covered in this chapter can be obtained through proper adjustment or variation of the GPE solver exampled in the

chapter. The numerical simulation given in chapter 5 requires a spatial grid consisting of a 1024 by 1024 complex-valued matrix ($256\,\mu m \times 256\,\mu m$ in real space) running with 2.0 ns total time and 10 fs time step, and 1.0 ns time-integrated sampling time for both intensity and mutual coherence factor, with the same time step of the simulation. Thanks to the power of parallel computing and good memory management of the GPE solver presented in this chapter, it is easier to manipulate the large data size and flow over a relatively long simulation time. From a future perspective, support for multiple GPUs and integration of the current workflow with NVIDIA's deep neural network library could open up new possibilities for polariton condensate studies. Also, the option of switching different numerical methods, for example, the widely used Runge–Kutta methods, can also be considered for future development.

Chapter 4 demonstrates the strongly focused polariton condensates, away from the pumping region, produced by the nonresonant positive- and negative-meniscus-lens-shaped excitation. To investigate condensates in an analog of the optical source-lens system, the refractive index of the lens to the source is obtained from the simplified modeling considering only the resonant planar driving term and complex-lens-shaped potential, and the corresponding numerical simulation is done with an algorithm similar to that introduced in the chapter 3. The results from the linear analysis show that, with proper lens thickness and radius, the closer the energy difference between the lens and the source, the less scattering occurs and the better accuracy from the lensmaker's equation is. With multiple energy modes enabled, the all-optical microscale lensing in complete 2D GPE simulation can cause hundreds of GHz focused-condensates beating. The beating frequency can be tuned by the energy difference between the lens and the source; moreover, the relative distance between the focal density and the lens can be adjusted by tailoring the geometry of the lens profile. The standing focal waves are also obtained by placing two face-to-face lenses. The reprogrammable capability makes it promising to achieve the all-optical transistor.

Chapter 5 keeps the isometric pump configurations like the pump profile used in chapter 4. For arbitrary C_n symmetric geometry rather than a perfect circle, the condensates produce more density along the area, which is outside the pumping region and is perpendicular to each side of the polygon, than the rest of the space. A special case with $n = 3$ is studied and compared with a circular pump. To make a fair comparison, both configurations are calibrated with the same condensation energy at the threshold power. The system consisting of side-side-facing nodes has the lower threshold power due to the highest interaction between nodes, followed by side-vertex, circular-, and vertex-vertex-facing configurations. In a large honeycomb lattice consisting of 150 nodes, in the presence of complex white noise, the side-side-facing triangular spots achieve higher spatial coherence than the circular spots at the same power density. The ballistic condensates outflow towards its nearest-neighbors spot, averaging over all the

power density, demonstrates an around 36% improvement from using the triangle-shaped spot. The bottlenecks of experiment in achieving higher spatial coherence in a large lattice usually lie in the power limit from the external excitation. Shaping the spots into an isometric shape, instead of the regular Gaussian spots, in the corresponding lattice configurations with side-side-facing orientation, like the triangular spot in a hexagonal lattice, greatly reduces the power consumption; in other words, higher coherence can be expected with the same power density.

References

[1] E. M. Purcell, Spontaneous emission probabilities at radio frequencies, in *Confined Electrons and Photons* (Springer, 1995) pp. 839–839.

[2] W.-H. Chang, W.-Y. Chen, H.-S. Chang, T.-P. Hsieh, J.-I. Chyi, and T.-M. Hsu, Efficient single-photon sources based on low-density quantum dots in photonic-crystal nanocavities, Physical review letters **96**, 117401 (2006).

[3] Y. Kaluzny, P. Goy, M. Gross, J. Raimond, and S. Haroche, Observation of self-induced rabi oscillations in two-level atoms excited inside a resonant cavity: the ringing regime of superradiance, Physical review letters **51**, 1175 (1983).

[4] D. N. Basov, A. Asenjo-Garcia, P. J. Schuck, X. Zhu, and A. Rubio, Polariton panorama, Nanophotonics **10**, 549 (2020).

[5] C. Weisbuch, M. Nishioka, A. Ishikawa, and Y. Arakawa, Observation of the coupled exciton-photon mode splitting in a semiconductor quantum microcavity, Physical Review Letters **69**, 3314 (1992).

[6] M. H. Anderson, J. R. Ensher, M. R. Matthews, C. E. Wieman, and E. A. Cornell, Observation of bose-einstein condensation in a dilute atomic vapor, science **269**, 198 (1995).

[7] K. B. Davis, M.-O. Mewes, M. R. Andrews, N. J. van Druten, D. S. Durfee, D. Kurn, and W. Ketterle, Bose-einstein condensation in a gas of sodium atoms, Physical review letters **75**, 3969 (1995).

[8] J. Kasprzak, M. Richard, S. Kundermann, A. Baas, P. Jeambrun, J. M. J. Keeling, F. Marchetti, M. Szymańska, R. André, J. Staehli, *et al.*, Bose–einstein condensation of exciton polaritons, Nature **443**, 409 (2006).

[9] S. Christopoulos, G. B. H. von Högersthal, A. J. D. Grundy, P. G. Lagoudakis, A. V. Kavokin, J. J. Baumberg, G. Christmann, R. Butté, E. Feltin, J.-F. Carlin, and N. Grandjean, Room-temperature polariton lasing in semiconductor microcavities, Phys. Rev. Lett. **98**, 126405 (2007).

[10] D. Sanvitto and S. Kéna-Cohen, The road towards polaritonic devices, Nature materials **15**, 1061 (2016).

[11] R. Su, J. Wang, J. Zhao, J. Xing, W. Zhao, C. Diederichs, T. C. Liew, and Q. Xiong, Room temperature long-range coherent exciton polariton condensate flow in lead halide perovskites, Science advances **4**, eaau0244 (2018).

[12] E. Wertz, L. Ferrier, D. Solnyshkov, R. Johne, D. Sanvitto, A. Lemaître, I. Sagnes, R. Grousson, A. V. Kavokin, P. Senellart, *et al.*, Spontaneous formation and optical manipulation of extended polariton condensates, Nature physics **6**, 860 (2010).

[13] J. Schmutzler, T. Kazimierczuk, Ö. Bayraktar, M. Aßmann, M. Bayer, S. Brodbeck, M. Kamp, C. Schneider, and S. Höfling, Influence of interactions with noncondensed particles on the coherence of a one-dimensional polariton condensate, Physical Review B **89**, 115119 (2014).

[14] G. Tosi, G. Christmann, N. G. Berloff, P. Tsotsis, T. Gao, Z. Hatzopoulos, P. G. Savvidis, and J. J. Baumberg, Sculpting oscillators with light within a nonlinear quantum fluid, Nature Physics **8**, 190 (2012).

[15] E. Wertz, A. Amo, D. D. Solnyshkov, L. Ferrier, T. C. H. Liew, D. Sanvitto, P. Senellart, I. Sagnes, A. Lemaître, A. V. Kavokin, G. Malpuech, and J. Bloch, Propagation and amplification dynamics of 1d polariton condensates, Phys. Rev. Lett. **109**, 216404 (2012).

[16] D. Niemietz, J. Schmutzler, P. Lewandowski, K. Winkler, M. Aßmann, S. Schumacher, S. Brodbeck, M. Kamp, C. Schneider, S. Höfling, *et al.*, Experimental realization of a polariton beam amplifier, Physical Review B **93**, 235301 (2016).

[17] P. Cristofolini, A. Dreismann, G. Christmann, G. Franchetti, N. G. Berloff, P. Tsotsis, Z. Hatzopoulos, P. G. Savvidis, and J. J. Baumberg, Optical superfluid phase transitions and trapping of polariton condensates, Phys. Rev. Lett. **110**, 186403 (2013).

[18] A. Askitopoulos, H. Ohadi, A. V. Kavokin, Z. Hatzopoulos, P. G. Savvidis, and P. G. Lagoudakis, Polariton condensation in an optically induced two-dimensional potential, Phys. Rev. B **88**, 041308 (2013).

[19] T. Gao, E. Estrecho, K. Y. Bliokh, T. C. H. Liew, M. D. Fraser, S. Brodbeck, M. Kamp, C. Schneider, S. Höfling, Y. Yamamoto, F. Nori, Y. S. Kivshar, A. G. Truscott, R. G. Dall, and E. A. Ostrovskaya, Observation of non-hermitian degeneracies in a chaotic exciton-polariton billiard, Nature **526**, 554 (2015).

[20] N. G. Berloff, M. Silva, K. Kalinin, A. Askitopoulos, J. D. Töpfer, P. Cilibrizzi, W. Langbein, and P. G. Lagoudakis, Realizing the classical xy hamiltonian in polariton simulators, Nature Materials **16**, 1120 (2017).

[21] R. Dall, M. D. Fraser, A. S. Desyatnikov, G. Li, S. Brodbeck, M. Kamp, C. Schneider, S. Höfling, and E. A. Ostrovskaya, Creation of orbital angular momentum states with chiral polaritonic lenses, Phys. Rev. Lett. **113**, 200404 (2014).

[22] X. Ma, B. Berger, M. Aßmann, R. Driben, T. Meier, C. Schneider, S. Höfling, and S. Schumacher, Realization of all-optical vortex switching in exciton-polariton condensates, Nature Communications **11**, 897 (2020).

[23] L. Pickup, H. Sigurdsson, J. Ruostekoski, and P. Lagoudakis, Synthetic band-structure engineering in polariton crystals with non-hermitian topological phases, Nature communications **11**, 1 (2020).

[24] M. Pieczarka, E. Estrecho, S. Ghosh, M. Wurdack, M. Steger, D. W. Snoke, K. West, L. N. Pfeiffer, T. C. H. Liew, A. G. Truscott, and E. A. Ostrovskaya, Topological phase transition in an all-optical exciton-polariton lattice, Optica **8**, 1084 (2021).

[25] D. Huang, E. A. Swanson, C. P. Lin, J. S. Schuman, W. G. Stinson, W. Chang, M. R. Hee, T. Flotte, K. Gregory, C. A. Puliafito, and J. G. Fujimoto, Optical coherence tomography, Science **254**, 1178 (1991).

[26] K. Hotate and T. Okugawa, Optical information processing by synthesis of the coherence function, Journal of Lightwave Technology **12**, 1247 (1994).

[27] Y. Chen, S. A. Ponomarenko, and Y. Cai, Experimental generation of optical coherence lattices, Applied Physics Letters **109**, 061107 (2016).

[28] B. J. Shastri, A. N. Tait, T. Ferreira de Lima, W. H. P. Pernice, H. Bhaskaran, C. D. Wright, and P. R. Prucnal, Photonics for artificial intelligence and neuromorphic computing, Nature Photonics **15**, 102 (2021).

[29] V. Giovannetti, S. Lloyd, and L. Maccone, Quantum-enhanced measurements: beating the standard quantum limit, Science **306**, 1330 (2004).

[30] A. V. Kavokin, J. J. Baumberg, G. Malpuech, and F. P. Laussy, *Microcavities*, Vol. 21 (Oxford university press, 2017).

[31] P. Cilibrizzi, A. Askitopoulos, M. Silva, F. Bastiman, E. Clarke, J. M. Zajac, W. Langbein, and P. G. Lagoudakis, Polariton condensation in a strain-compensated planar microcavity with ingaas quantum wells, Applied Physics Letters **105**, 191118 (2014).

[32] T. Kazimierczuk, D. Fröhlich, S. Scheel, H. Stolz, and M. Bayer, Giant rydberg excitons in the copper oxide cu2o, Nature **514**, 343 (2014).

[33] M. Aßmann and M. Bayer, Semiconductor rydberg physics, Advanced Quantum Technologies **3**, 1900134 (2020).

[34] P. Yang, Fermi's golden rule, optical transition. materials chemistry II (2016), online lecture notes.

[35] C. Ciuti, G. Bastard, and I. Carusotto, Quantum vacuum properties of the intersubband cavity polariton field, Physical Review B **72**, 115303 (2005).

[36] A. Frisk Kockum, A. Miranowicz, S. De Liberato, S. Savasta, and F. Nori, Ultrastrong coupling between light and matter, Nature Reviews Physics **1**, 19 (2019).

[37] J. Hopfield, Theory of the contribution of excitons to the complex dielectric constant of crystals, Physical Review **112**, 1555 (1958).

[38] Y. Todorov and C. Sirtori, Intersubband polaritons in the electrical dipole gauge, Physical Review B **85**, 045304 (2012).

[39] E. Wertz, L. Ferrier, D. D. Solnyshkov, P. Senellart, D. Bajoni, A. Miard, A. Lemaître, G. Malpuech, and J. Bloch, Spontaneous formation of a polariton condensate in a planar gaas microcavity, Applied Physics Letters **95**, 051108 (2009).

[40] C. Ciuti, P. Schwendimann, and A. Quattropani, Theory of polariton parametric interactions in semiconductor microcavities, Semiconductor science and technology **18**, S279 (2003).

[41] M. Wouters and I. Carusotto, Excitations in a nonequilibrium bose-einstein condensate of exciton polaritons, Phys. Rev. Lett. **99**, 140402 (2007).

[42] M. Wouters and V. Savona, Stochastic classical field model for polariton condensates, Phys. Rev. B **79**, 165302 (2009).

[43] M. Feit, J. Fleck Jr, and A. Steiger, Solution of the schrödinger equation by a spectral method, Journal of Computational Physics **47**, 412 (1982).

[44] Z. Li, N. B. Kovachki, K. Azizzadenesheli, B. liu, K. Bhattacharya, A. Stuart, and A. Anandkumar, Fourier neural operator for parametric partial differential equations, in *International Conference on Learning Representations* (2021).

[45] G. R. Dennis, J. J. Hope, and M. T. Johnsson, Xmds2: Fast, scalable simulation of coupled stochastic partial differential equations, Computer Physics Communications **184**, 201 (2013).

[46] X. Antoine and R. Duboscq, Gpelab, a matlab toolbox to solve gross–pitaevskii equations i: Computation of stationary solutions, Computer Physics Communications **185**, 2969 (2014).

[47] X. Antoine and R. Duboscq, Gpelab, a matlab toolbox to solve gross–pitaevskii equations ii: Dynamics and stochastic simulations, Computer Physics Communications **193**, 95 (2015).

[48] J. Gaidamour, Q. Tang, and X. Antoine, Bec2hpc: A hpc spectral solver for nonlinear schrödinger and rotating gross-pitaevskii equations. stationary states computation, Computer Physics Communications **265**, 108007 (2021).

[49] H. Bauke and C. H. Keitel, Accelerating the fourier split operator method via graphics processing units, Computer Physics Communications **182**, 2454 (2011).

[50] J. R. Schloss and L. J. O'Riordan, Gpue: Graphics processing unit gross–pitaevskii equation solver, Journal of Open Source Software **3**, 1037 (2018).

[51] B. D. Smith, L. W. Cooke, and L. J. LeBlanc, Gpu-accelerated solutions of the nonlinear schrödinger equation for simulating 2d spinor becs, Computer Physics Communications **275**, 108314 (2022).

[52] M. Kivioja, S. Mönkölä, and T. Rossi, Gpu-accelerated time integration of gross-pitaevskii equation with discrete exterior calculus, Computer Physics Communications **278**, 108427 (2022).

[53] Cuda toolkit, `https://developer.nvidia.com/cuda-toolkit` (2022).

[54] J. W. Cooley and J. W. Tukey, An algorithm for the machine calculation of complex fourier series, Mathematics of computation **19**, 297 (1965).

[55] FFTW, `https://www.fftw.org`.

[56] J. Javanainen and J. Ruostekoski, Symbolic calculation in development of algorithms: split-step methods for the gross–pitaevskii equation, Journal of Physics A: Mathematical and General **39**, L179 (2006).

[57] Cuda c++ programming guide 11.8, `https://docs.nvidia.com/cuda` (2022).

[58] A. Krizhevsky, I. Sutskever, and G. E. Hinton, Imagenet classification with deep convolutional neural networks, Communications of the ACM **60**, 84 (2017).

[59] M. Harris, Cuda pro tip: Write flexible kernels with grid-stride loops, `https://developer.nvidia.com/blog/cuda-pro-tip-write-flexible-kernels-grid-stride-loops/`.

[60] M. Harris *et al.*, Optimizing parallel reduction in cuda, Nvidia developer technology **2**, 70 (2007).

[61] Cuda c++ best practices guide, `https://docs.nvidia.com/cuda/cuda-c-best-practices-guide/` (2022).

[62] R. J. Lipton, Reduction: A method of proving properties of parallel programs, Communications of the ACM **18**, 717 (1975).

[63] W. Yuan, L.-H. Li, W.-B. Lee, and C.-Y. Chan, Fabrication of microlens array and its application: A review, Chinese Journal of Mechanical Engineering **31**, 16 (2018).

[64] P. Singh, D. K. Tripathi, S. Jaiswal, and H. K. Dixit, All-optical logic gates: Designs, classification, and comparison, Advances in Optical Technologies **2014**, 275083 (2014).

[65] D. Lu and Z. Liu, Hyperlenses and metalenses for far-field super-resolution imaging, Nature communications **3**, 1 (2012).

[66] M. Khorasaninejad and F. Capasso, Metalenses: Versatile multifunctional photonic components, Science **358**, eaam8100 (2017).

[67] Z. Liu, J. M. Steele, W. Srituravanich, Y. Pikus, C. Sun, and X. Zhang, Focusing surface plasmons with a plasmonic lens, Nano Letters **5**, 1726 (2005).

[68] H. Kim, J. Hahn, and B. Lee, Focusing properties of surface plasmon polariton floating dielectric lenses, Opt. Express **16**, 3049 (2008).

[69] L. Verslegers, P. B. Catrysse, Z. Yu, J. S. White, E. S. Barnard, M. L. Brongersma, and S. Fan, Planar lenses based on nanoscale slit arrays in a metallic film, Nano Letters **9**, 235 (2009).

[70] Y. Chen, X. Li, Y. Sonnefraud, A. I. Fernández-Domínguez, X. Luo, M. Hong, and S. A. Maier, Engineering the phase front of light with phase-change material based planar lenses, Scientific reports **5**, 1 (2015).

[71] P. V. Parimi, W. T. Lu, P. Vodo, and S. Sridhar, Imaging by flat lens using negative refraction, Nature **426**, 404 (2003).

[72] B. D. F. Casse, W. T. Lu, Y. J. Huang, and S. Sridhar, Nano-optical microlens with ultrashort focal length using negative refraction, Applied Physics Letters **93**, 053111 (2008).

[73] M. Leonetti, S. Karbasi, A. Mafi, and C. Conti, Light focusing in the anderson regime, Nature Communications **5**, 4534 (2014).

[74] C. Sturm, D. Tanese, H. S. Nguyen, H. Flayac, E. Galopin, A. Lemaître, I. Sagnes, D. Solnyshkov, A. Amo, G. Malpuech, and J. Bloch, All-optical phase modulation in a cavity-polariton mach–zehnder interferometer, Nature Communications **5**, 3278 (2014).

[75] E. Rozas, J. Beierlein, A. Yulin, M. Klaas, H. Suchomel, O. Egorov, I. A. Shelykh, U. Peschel, C. Schneider, S. Klembt, *et al.*, Impact of the energetic landscape on polariton condensates' propagation along a coupler, Advanced Optical Materials **8**, 2000650 (2020).

[76] A. V. Zasedatelev, A. V. Baranikov, D. Urbonas, F. Scafirimuto, U. Scherf, T. Stöferle, R. F. Mahrt, and P. G. Lagoudakis, A room-temperature organic polariton transistor, Nature Photonics **13**, 378 (2019).

[77] A. V. Zasedatelev, A. V. Baranikov, D. Sannikov, D. Urbonas, F. Scafirimuto, V. Y. Shishkov, E. S. Andrianov, Y. E. Lozovik, U. Scherf, T. Stöferle, *et al.*, Single-photon nonlinearity at room temperature, Nature **597**, 493 (2021).

[78] K. Chaudhary, M. Tamagnone, X. Yin, C. M. Spägele, S. L. Oscurato, J. Li, C. Persch, R. Li, N. A. Rubin, L. A. Jauregui, K. Watanabe, T. Taniguchi, P. Kim, M. Wuttig, J. H. Edgar, A. Ambrosio, and F. Capasso, Polariton nanophotonics using phase-change materials, Nature Communications **10**, 4487 (2019).

[79] J. Schmutzler, P. Lewandowski, M. Aßmann, D. Niemietz, S. Schumacher, M. Kamp, C. Schneider, S. Höfling, and M. Bayer, All-optical flow control of a polariton condensate using nonresonant excitation, Phys. Rev. B **91**, 195308 (2015).

[80] P. Cristofolini, Z. Hatzopoulos, P. G. Savvidis, and J. J. Baumberg, Generation of quantized polaritons below the condensation threshold, Phys. Rev. Lett. **121**, 067401 (2018).

[81] M. Aßmann, F. Veit, M. Bayer, A. Löffler, S. Höfling, M. Kamp, and A. Forchel, All-optical control of quantized momenta on a polariton staircase, Phys. Rev. B **85**, 155320 (2012).

[82] D. Ballarini, D. Caputo, G. Dagvadorj, R. Juggins, M. D. Giorgi, L. Dominici, K. West, L. N. Pfeiffer, G. Gigli, M. H. Szymańska, *et al.*, Directional goldstone waves in polariton condensates close to equilibrium, Nature communications **11**, 217 (2020).

[83] F. Barkhausen, M. Pukrop, S. Schumacher, and X. Ma, Structuring coflowing and counterflowing currents of polariton condensates in concentric ring-shaped and elliptical potentials, Physical Review B **103**, 075305 (2021).

[84] Y. Xue, I. Chestnov, E. Sedov, E. Kiktenko, A. K. Fedorov, S. Schumacher, X. Ma, and A. Kavokin, Split-ring polariton condensates as macroscopic two-level quantum systems, Physical Review Research **3**, 013099 (2021).

[85] T. Gao, P. S. Eldridge, T. C. H. Liew, S. I. Tsintzos, G. Stavrinidis, G. Deligeorgis, Z. Hatzopoulos, and P. G. Savvidis, Polariton condensate transistor switch, Phys. Rev. B **85**, 235102 (2012).

[86] C. Antón, T. C. H. Liew, G. Tosi, M. D. Martín, T. Gao, Z. Hatzopoulos, P. S. Eldridge, P. G. Savvidis, and L. Viña, Energy relaxation of exciton-polariton condensates in quasi-one-dimensional microcavities, Phys. Rev. B **88**, 035313 (2013).

[87] C. Schneider, K. Winkler, M. D. Fraser, M. Kamp, Y. Yamamoto, E. A. Ostrovskaya, and S. Höfling, Exciton-polariton trapping and potential landscape engineering, Reports on Progress in Physics **80**, 016503 (2016).

[88] Y. Sun, P. Wen, Y. Yoon, G. Liu, M. Steger, L. N. Pfeiffer, K. West, D. W. Snoke, and K. A. Nelson, Bose-einstein condensation of long-lifetime polaritons in thermal equilibrium, Phys. Rev. Lett. **118**, 016602 (2017).

[89] A. Alù, M. G. Silveirinha, A. Salandrino, and N. Engheta, Epsilon-near-zero metamaterials and electromagnetic sources: Tailoring the radiation phase pattern, Phys. Rev. B **75**, 155410 (2007).

[90] L. A. Smirnov, D. A. Smirnova, E. A. Ostrovskaya, and Y. S. Kivshar, Dynamics and stability of dark solitons in exciton-polariton condensates, Phys. Rev. B **89**, 235310 (2014).

[91] I. L. Aleiner, B. L. Altshuler, and Y. G. Rubo, Radiative coupling and weak lasing of exciton-polariton condensates, Phys. Rev. B **85**, 121301 (2012).

[92] S. Khan and H. E. Türeci, Non-hermitian coupled-mode theory for incoherently pumped exciton-polariton condensates, Phys. Rev. A **94**, 053856 (2016).

[93] D. N. Krizhanovskii, K. G. Lagoudakis, M. Wouters, B. Pietka, R. A. Bradley, K. Guda, D. M. Whittaker, M. S. Skolnick, B. Deveaud-Plédran, M. Richard, R. André, and L. S. Dang, Coexisting nonequilibrium condensates with long-range spatial coherence in semiconductor microcavities, Phys. Rev. B **80**, 045317 (2009).

[94] J. D. Töpfer, H. Sigurdsson, L. Pickup, and P. G. Lagoudakis, Time-delay polaritonics, Communications Physics **3**, 1 (2020).

[95] D. Racine and P. R. Eastham, Quantum theory of multimode polariton condensation, Phys. Rev. B **90**, 085308 (2014).

[96] D. Ballarini, I. Chestnov, D. Caputo, M. De Giorgi, L. Dominici, K. West, L. N. Pfeiffer, G. Gigli, A. Kavokin, and D. Sanvitto, Self-trapping of exciton-polariton condensates in gaas microcavities, Phys. Rev. Lett. **123**, 047401 (2019).

[97] L. Pickup, J. D. Töpfer, H. Sigurdsson, and P. G. Lagoudakis, Polariton spin jets through optical control, Phys. Rev. B **103**, 155302 (2021).

[98] A. Amo, S. Pigeon, C. Adrados, R. Houdré, E. Giacobino, C. Ciuti, and A. Bramati, Light engineering of the polariton landscape in semiconductor microcavities, Phys. Rev. B **82**, 081301 (2010).

[99] D. Sanvitto, S. Pigeon, A. Amo, D. Ballarini, M. De Giorgi, I. Carusotto, R. Hivet, F. Pisanello, V. G. Sala, P. S. S. Guimaraes, R. Houdré, E. Giacobino, C. Ciuti,

A. Bramati, and G. Gigli, All-optical control of the quantum flow of a polariton condensate, Nature Photonics **5**, 610 (2011).

[100] C. Leblanc, G. Malpuech, and D. D. Solnyshkov, High-frequency exciton-polariton clock generator, Phys. Rev. B **101**, 115418 (2020).

[101] D. Aristov, S. Baryshev, J. D. Töpfer, H. Sigurðsson, and P. G. Lagoudakis, Reservoir microlensing in polariton condensates, arXiv:2305.19682 (2023).

[102] C. Li, X. Chai, B. Wei, J. Yang, A. Daruwalla, F. Ayazi, and C. Raman, Cascaded collimator for atomic beams traveling in planar silicon devices, Nature Communications **10**, 1831 (2019).

[103] S. Pandey, H. Mas, G. Vasilakis, and W. von Klitzing, Atomtronic matter-wave lensing, Phys. Rev. Lett. **126**, 170402 (2021).

[104] F. Nogrette, H. Labuhn, S. Ravets, D. Barredo, L. Béguin, A. Vernier, T. Lahaye, and A. Browaeys, Single-atom trapping in holographic 2d arrays of microtraps with arbitrary geometries, Phys. Rev. X **4**, 021034 (2014).

[105] Y. Wang, H. Sigurdsson, J. Töpfer, and P. Lagoudakis, Reservoir optics with exciton-polariton condensates, Physical Review B **104**, 235306 (2021).

[106] C. E. Whittaker, E. Cancellieri, P. M. Walker, D. R. Gulevich, H. Schomerus, D. Vaitiekus, B. Royall, D. M. Whittaker, E. Clarke, I. V. Iorsh, I. A. Shelykh, M. S. Skolnick, and D. N. Krizhanovskii, Exciton polaritons in a two-dimensional lieb lattice with spin-orbit coupling, Phys. Rev. Lett. **120**, 097401 (2018).

[107] V. Goblot, B. Rauer, F. Vicentini, A. Le Boité, E. Galopin, A. Lemaître, L. Le Gratiet, A. Harouri, I. Sagnes, S. Ravets, C. Ciuti, A. Amo, and J. Bloch, Nonlinear polariton fluids in a flatband reveal discrete gap solitons, Phys. Rev. Lett. **123**, 113901 (2019).

[108] C. W. Lai, N. Y. Kim, S. Utsunomiya, G. Roumpos, H. Deng, M. D. Fraser, T. Byrnes, P. Recher, N. Kumada, T. Fujisawa, and Y. Yamamoto, Coherent zero-state and π-state in an exciton–polariton condensate array, Nature **450**, 529 (2007).

[109] R. Su, S. Ghosh, J. Wang, S. Liu, C. Diederichs, T. C. H. Liew, and Q. Xiong, Observation of exciton polariton condensation in a perovskite lattice at room temperature, Nature Physics **16**, 301 (2020).

[110] T. H. Harder, O. A. Egorov, C. Krause, J. Beierlein, P. Gagel, M. Emmerling, C. Schneider, U. Peschel, S. Höfling, and S. Klembt, Kagome flatbands for coherent exciton-polariton lasing, ACS Photonics **8**, 3193 (2021).

[111] E. A. Cerda-Méndez, D. N. Krizhanovskii, M. Wouters, R. Bradley, K. Biermann, K. Guda, R. Hey, P. V. Santos, D. Sarkar, and M. S. Skolnick, Polariton condensation in dynamic acoustic lattices, Phys. Rev. Lett. **105**, 116402 (2010).

[112] G. Tosi, G. Christmann, N. G. Berloff, P. Tsotsis, T. Gao, Z. Hatzopoulos, P. G. Savvidis, and J. J. Baumberg, Geometrically locked vortex lattices in semiconductor quantum fluids, Nature Communications **3**, 1243 (2012).

[113] J. D. Töpfer, I. Chatzopoulos, H. Sigurdsson, T. Cookson, Y. G. Rubo, and P. G. Lagoudakis, Engineering spatial coherence in lattices of polariton condensates, Optica **8**, 106 (2021).

[114] T. Boulier, M. J. Jacquet, A. Maître, G. Lerario, F. Claude, S. Pigeon, Q. Glorieux, A. Amo, J. Bloch, A. Bramati, and E. Giacobino, Microcavity polaritons for quantum simulation, Advanced Quantum Technologies **3**, 2000052 (2020).

[115] A. Kavokin, T. C. H. Liew, C. Schneider, P. G. Lagoudakis, S. Klembt, and S. Hoefling, Polariton condensates for classical and quantum computing, Nature Reviews Physics **4**, 435 (2022).

[116] I. Carusotto and C. Ciuti, Quantum fluids of light, Rev. Mod. Phys. **85**, 299 (2013).

[117] S.-i. Takayama, H. Kitagawa, Y. Tanaka, T. Asano, and S. Noda, Experimental demonstration of complete photonic band gap in two-dimensional photonic crystal slabs, Applied Physics Letters **87**, 061107 (2005).

[118] R. Tao, K. Peng, L. Haeberlé, Q. Li, D. Jin, G. R. Fleming, S. Kéna-Cohen, X. Zhang, and W. Bao, Halide perovskites enable polaritonic xy spin hamiltonian at room temperature, Nature Materials **21**, 761 (2022).

[119] T. Cookson, K. Kalinin, H. Sigurdsson, J. D. Töpfer, S. Alyatkin, M. Silva, W. Langbein, N. G. Berloff, and P. G. Lagoudakis, Geometric frustration in polygons of polariton condensates creating vortices of varying topological charge, Nature Communications **12**, 2120 (2021).

[120] Y. Zhang, X. Zhang, B. Tang, C. Tian, C. Xu, H. Dong, and W. Zhou, Realization of an all-optically controlled dynamic superlattice for exciton–polaritons, Nanoscale **10**, 14082 (2018).

[121] S. Alyatkin, J. Töpfer, A. Askitopoulos, H. Sigurdsson, and P. Lagoudakis, Optical control of couplings in polariton condensate lattices, Physical Review Letters **124**, 207402 (2020).

[122] G. Christmann, G. Tosi, N. G. Berloff, P. Tsotsis, P. S. Eldridge, Z. Hatzopoulos, P. G. Savvidis, and J. J. Baumberg, Polariton ring condensates and sunflower ripples in an expanding quantum liquid, Phys. Rev. B **85**, 235303 (2012).

[123] T.-Y. Kao, J. L. Reno, and Q. Hu, Phase-locked laser arrays through global antenna mutual coupling, Nature Photonics **10**, 541 (2016).

[124] D. Caputo, D. Ballarini, G. Dagvadorj, C. Sánchez Muñoz, M. De Giorgi, L. Dominici, K. West, L. N. Pfeiffer, G. Gigli, F. P. Laussy, *et al.*, Topological order and thermal equilibrium in polariton condensates, Nature materials **17**, 145 (2018).

[125] H. Deng, G. S. Solomon, R. Hey, K. H. Ploog, and Y. Yamamoto, Spatial coherence of a polariton condensate, Phys. Rev. Lett. **99**, 126403 (2007).

[126] Y. Wang, P. Lagoudakis, and H. Sigurdsson, Enhanced coupling between ballistic exciton-polariton condensates through tailored pumping, Physical Review B **106**, 245304 (2022).